Microscale sensing with NV centers in diamond

Janis Smits

March 20, 2020

Abstract

The negatively charged nitrogen-vacancy (NV) center in diamond possesses excellent room-temperature coherence properties and is a very promising candidate platform for the next generation of high sensitivity magnetic sensors. In this work we investigated the relaxation dynamics and sensing performance of the nitrogen-vacancy (NV) center.

while examining the NV concentration dependent population relaxation times T_1 we found strong evidence of NV-NV dipole-dipole couplings being the dominant relaxation channel for high NV concentrations ($>$1 ppm).

We also studied two distinct NV magnetometry modalities. One of them was the NV based magnetic microscope which was used to obtain optical resolution magnetic signals. Several key insights on experimental design were obtained from these efforts which, we believe, could enable us to study time-dependent magnetic processes.

The other was a high-sensitivity and high-spectral resolution NV based nuclear magnetic resonance spectrometer was built and the first two-dimensional NMR signal of an external analyte was obtained on such a system.

Acknowledgments

I would like to thank my thesis supervisor Florian Gahbauer for his patience, the his generosity with his time and the insightful discussions that always helped to get me unstuck. I hope to one day master the use of the em dash and make you proud!

I would like to thank my colleagues and co-authors at the University of Latvia without whom this work would not have been made possible, Andris Berzins, Reinis Lazda, Laima Busaite, Marcis Auzinsh, Ruvins Ferbers, Arturs Mozers and Artis Kruzins.

I would also like to thank my parents Elita Smite and Guntars Smits who have always shown unwavering support in all of my endeavours including this one.

Finally I would like to thank my partner Katrina Laganovska who bore the brunt of the days when nothing worked and helped me through all of it.

List of papers used in the work and corresponding author contributions

A. Jarmola, A. Berzins, J. Smits, *et al.*, “Longitudinal spin-relaxation in nitrogen-vacancy centers in electron irradiated diamond”, *Applied Physics Letters*, vol. 107, no. 24, p. 242 403, Dec. 2015, ISSN: 0003-6951. DOI: `10.1063/1.4937489`
Author’s contributions: Performed data analysis, experimental measurements, participated in the construction of the experimental setup.

J. Smits, A. Berzins, F. H. Gahbauer, *et al.*, “Estimating the magnetic moment of microscopic magnetic sources from their magnetic field distribution in a layer of nitrogen-vacancy (NV) centres in diamond”, en, *The European Physical Journal Applied Physics*, vol. 73, no. 2, p. 20 701, Feb. 2016, ISSN: 1286-0042, 1286-0050. DOI: `10.1051/epjap/2016150449`
Author’s contributions: Performed data analysis, developed the deconvolution and magnetic parameter fitting code

J. Smits, J. T. Damron, P. Kehayias, *et al.*, “Two-dimensional nuclear magnetic resonance spectroscopy with a microfluidic diamond quantum sensor”, *Science Advances*, vol. 5, no. 7, eaaw7895, Jul. 2019. DOI: `10.1126/sciadv.aaw7895`
Author’s contributions: Performed data analysis, experimental measurements, setup construction, wrote control software

P. Kehayias, A. Jarmola, N. Mosavian, *et al.*, “Solution nuclear magnetic resonance spectroscopy on a nanostructured diamond chip”, En, *Nature Communications*, vol. 8, no. 1, p. 188, Aug. 2017, ISSN: 2041-1723. DOI: `10.1038/s41467-017-00266-4`
Author’s contributions: Performed part of the data analysis, performed part of the experimental measurements

I. Fescenko, A. Laraoui, J. Smits, *et al.*, “Diamond Magnetic Microscopy of Malarial Hemozoin Nanocrystals”, *Physical Review Applied*, vol. 11, no. 3, p. 034 029, Mar. 2019. DOI: `10.1103/PhysRevApplied.11.034029`
Author’s contributions: Wrote part of the control software

Contents

Chapter 1

Background

In recent years research of quantum technologies has progressed considerably with many research groups now focusing on not only fundamental research but concrete applications and product development [1]–[3].

The most widely known quantum technology is probably the quantum computer. Several public and private bodies (IBM, ETH-Zurich, Rigetti and Microsoft [4]) are offering development platforms and access to genuine quantum machines. This rapid advance has been made possible by identifying platforms that can be efficiently decoupled from the rest of the universe as one of the limiting factors is the coherence time of the qubit.

Whilst this extreme sensitivity to external forces might be undesirable in computing applications a complementary class of applications have emerged in recent years that seeks to capitalize on this weakness of the quantum systems. Examples of quantum systems tailored for sensing are atomic vapor magnetometers, atomic clocks, superconducting quantum interference devices and quantum defects in solids.

Among the latter the nitrogen-vacancy color center (NV center) in diamond stands out with an array of remarkable properties. First, the ground spin state of the NV center can be both intialized and read out optically; in addition the spin state can be coherently manipulated using microwave radiation. Second, the spin coherence time (T_2) even at room temperature can reach up to ~ms [5] and reach seconds at liquid nitrogen temperatures [6]. Finally, the physically robust, chemically inert and biocompatible diamond matrix lends itself well to nanostructuring, which enables favorable geometries for sensing applications such as trenches [7] or nanopillars [8], studies in biological systems [9], [10] and the potent fabrication processes familiar in the semiconductor industry such as chemical vapor deposition (CVD), delta-doping or ion implantation. These methods grant a high degree of control over the isotopical composition [5], [11], [12], NV concentration [13], [14] and spatial distribution [15], [16], which make it possible to tailor the quantum sensor to a particular application.

Samples of bulk NVs have managed to achieve a $\sim$pT/$\sqrt{Hz}$ sensitivity [17] and microscale ensembles have reported a sensitivity as low as 1.2 nT/μm$^{3/2}$/$\sqrt{Hz}$ [18].

This thesis focuses on NV coherence time characterization and two different sensing modalities: microscale magnetic imaging and high-resolution, picoliter-scale nuclear magnetic resonance (NMR). The first chapter covers the basic structure of the NV center and the fundamentals of magnetic sensing using the defect. Chapter 2 briefly describes the relaxation mechanisms and characteristic relaxation times (T_1, T_2 and T_2^*). Chapter 3 moves on to magnetic microscopy with NV centers and finally chapter 4 deals with the applicability of NV center bases sensors in nuclear magnetic resonance spectroscopy.

The overall goal of the thesis is as follows: **Study the NV relaxation processes, build a NV based magnetic microscope and move the NV nuclear magnetic resonance spectrometer towards competitiveness with conventional techniques.**

To achieve this goal I set myself three tasks:

- Characterize the T_1 relaxation rate as a function of NV concentration and use the data to infer the possible relaxation mechanisms.
- Construct a NV diamond magnetic microscope and evaluate the possibility of studying time-dependent processes with this technique.
- Examine the feasibility of performing two-dimensional nuclear magnetic resonance experiments with an NV based sensor.

1.1 The NV center structure

The nitrogen-vacancy center point defect in diamond with C_{3v} symmetry formed when a nitrogen atom replaces a carbon atom and, additionally, is joined by a vacancy in an adjacent carbon site, as shown in Fig. 1.1.

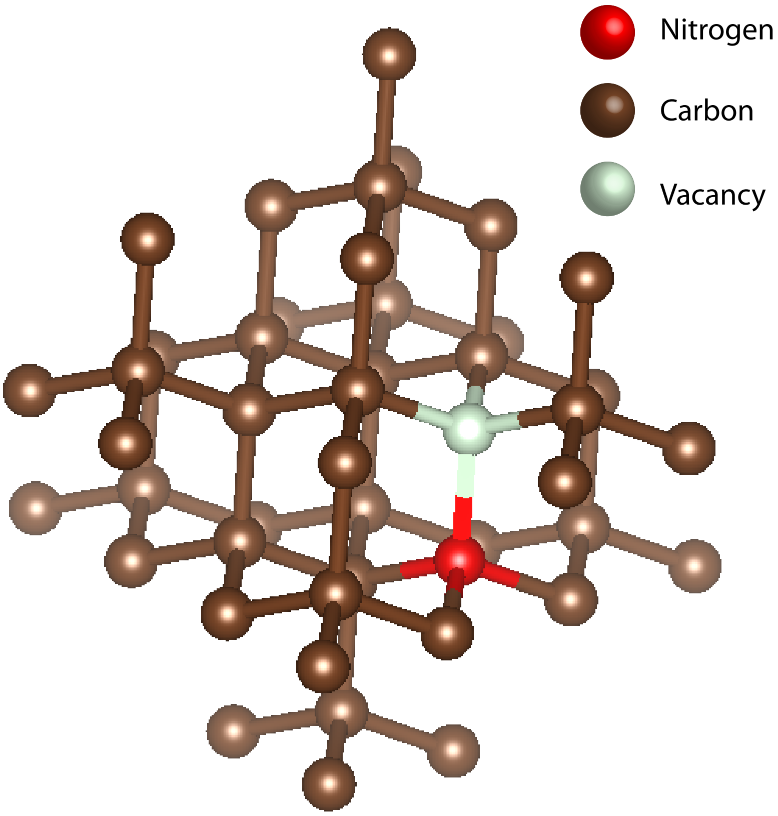

Figure 1.1: The structure of the NV center. For the negatively charged center the electron is mostly localized at the vacancy site. The axis connecting the nitrogen to the vacancy is the quantization axis.

There exist several charge state variations of the defect: NV^+ [19], [20], NV^0 [21] and NV^- [22]–[24] where the NV^0 and NV^- are the predominant varieties [25]. The negatively charged center exhibits the properties that make it highly attractive. These properties are:

- The spin state can be prepared optically.
- The spin state can be read out optically.
- Spin coherence times that are long compared to most other solid state qubit systems.

It is common in the literature to drop the "-" sign, and this practice will also be employed in this work. It is thought that the source of the additional electron are substitutional nitrogen defects (also known as P1 centers) [22], [26]. The NV center itself possesses a C_{3v} symmetry with the symmetry axis aligned along the crystalline sites of the nitrogen and vacancy. In most bulk diamond/NV fabrication techniques all four possible alignment direction are equally probable resulting in four subsets of NV centers. However, preferential orientation along two directions can be achieved through clever substrate selection and appropriate CVD growth protocols [27], [28].

1.2 NV formation and common fabrication techniques

The general steps of fabricating a NV diamond are:

- Preparation of a diamond matrix with the necessary nitrogen, ^{13}C content/volumetric distribution.
- Introduction of vacancy defects in the diamond either by ion or electron irradiation. In some cases the first and second steps are combined by using nitrogen as the vacation forming ion. High-power impulse lasers have also been used to both locally create vacancies and perform the annealing step to form NV centers [15], [29].
- High-temperature annealing in an oxygen-free atmosphere, which causes the vacancies to diffuse through the diamond until they encounter a site adjacent to a substitutional nitrogen.

▲ (Optional) Surface treatment (Plasma cleaning, acid washing etc.). In occasions where very shallow (∼5 nm or lower) NVs are necessary, oxygen termination of the dangling carbon bonds leads to better performance as it inhibits the $NV^- \rightarrow NV^0$ charge state transition [20], [30], [31].

Two processes are commonly used to produce diamonds for NV applications. The high-pressure, high-temperature (HPHT) transforms carbon to graphite in high-temperature presses. This process is relatively cheap, but produces diamonds with a higher nitrogen content and more defects. Chemical vapor deposition (CVD) builds diamonds layer by layer as atoms from a vapor are deposited on a substrate. The CVD process is slower and costlier, but yields higher purity diamonds.

The HPHT process attempts to recreate the conditions in the Earth's mantle where diamonds form naturally, i.e., high pressure and high temperature. The first industrialized method for synthetic diamond synthesis was developed by Bundy *et al.* [32], [33], achieving a pressure of 10 GPa and a temperature in the neighbourhood 2000 °C. An essential step for achieving repeatable crystal growth was the addition of nickel, cobalt or iron in the crucible along with the seed diamond. The metals act as catalysts for the growth process [33]. Over the years improvements in anvil quality have enabled longer periods of sustained high pressure [34]. Better understanding of crystal growth process prompted the introduction of additives to bind contaminants such as nitrogen (Ti, Al) or to alter the hue of the gemstone (for example the introduction of boron produces a bluish color) [35] Over the years, improvements have been made both in anvil quality, allowing for longer periods of sustained high pressure [34], and also crystal growth control. In the context of fabricating NV-based sensors HPHT diamonds have a relatively high content of nitrogen homogeneously distributed in the whole volume of the chip. It means that it is necessary to introduce only vacancies in the system and anneal in order to form NV centers. These vacancies can be created by high energy electrons, which are more easily produced than high-energy ions and also introduce considerably less lattice damage netting higher performing defects [33].

In recent years, CVD-grown diamond chips have become the prevalent host for bulk NV-based quantum sensors. There are two main reasons for this development. First, it is possible to maintain a high level of control over the spatial distribution of NV centers by using very high purity host matrices. In this case the NV depth distribution is determined by an appropriate selection of nitrogen ion implantation energies (ions tend to have a narrow implantation depth [36] ∼10 nm). A more advanced technique is the so-called delta-doping [37]–[42], where N_2 gas is introduced during the growth process to form a nitrogen-rich layer of the desired depth, thickness and defect density. Then the vacancies can be generated either by electron irradiation or light-ion implantation.

Second, CVD diamonds have fewer defects or impurities [13] than HPHT diamonds and enable the creation of isotopically pure layers of ^{12}C, which suppress the magnetic noise caused by the ^{13}C isotope (natural abundance - 1.1 %). Signals from NVs embedded in diamond matrices with fewer paramagnetic defects or lattice imperfections will experience less inhomogeneous broadening yielding better but more expensive sensors.

1.3 The NV energy structure

In total six electrons form the NV center. Two of them occupy an energy level within the conduction band and remain filled for all observable electronic energy levels of the nitrogen vacancy center [22]. The remaining electrons occupy molecular orbitals (MO) formed from the dangling bonds of surrounding nitrogen and carbon atoms. A group-theoretical approach describing the MO formation from the dangling bonds, energy ordering of singlet/triplet states and spin-orbit interaction is presented by Maze *et al.* [43] and is beyond the scope of this thesis.

The electronic energy structure and absorption/emission spectra in the triplet state manifold of the NV center are depicted in Fig. 1.2. The broad vibronic bands mean that excitation and emission can occur at different wavelengths, thus enabling easy separation between them by using dichroic mirrors or filters. Besides the direct optical transitions, there exists a non-radiative inter-system crossing to the metastable singlet state which can further transition back to the triplet through another radiation-free pathway. Between the electronic states of the singlet (^{1}A and ^{1}E) both optical (1042 nm) and non-radiative transitions are possible with the non-radiative decay between the singlet states dominating the infrared decay path [44]. The fine structure spin Hamiltonian of the ground state triplet level ^{3}A$_2$ takes the form [46]:

$$\begin{aligned} H_{gs} =& D_{gs}\left[S_z^2 - S(S+1)/3\right] + A_{gs}^{\|} S_z I_z + A_{gs}^{\perp}\left[S_x I_x + S_y I_y\right] + \\ & P_{gs}[I_z^2 - I(I+1)/3], \end{aligned} \tag{1.1}$$

where D_{gs} is the fine structure splitting, $A_{gs}^{\|}$ and $A_{gs}^{\perp}$ are the parallel and perpendicular components of the hyperfine interaction tensor,$S_{x,y,z}$ and $I_{x,y,z}$ are electronic and nuclear spin operators, and P_{gs} is the nuclear quadrupole parameter. Not that for ^{15}N the nuclear spin is $I = 1/2$ and so $P_{gs} = 0$. The value of D_{gs} at room temperature is $\sim$ 2.87 GHz, but it exhibits a temperature dependence of $\sim$ 74 kHz per Kelvin [47]. The magnetic and electric/strain field interaction of the ground state is well described by the following Hamiltonian [22]:

$$\begin{aligned} V_{gs} =& \mu_B g \mathbf{S}\cdot\mathbf{B} + \mu_B g_N \mathbf{I}\cdot\mathbf{B} + d_{gs}^{\|}\left[S_z^2 - S(S+1)/3\right] + \\ & + d_{gs}^{\perp}(E_x+\delta_x)\left(S_x^2 - S_y^2\right) + d_{gs}^{\perp}(E_y+\delta_y)\left(S_x S_y + S_y S_x\right), \end{aligned} \tag{1.2}$$

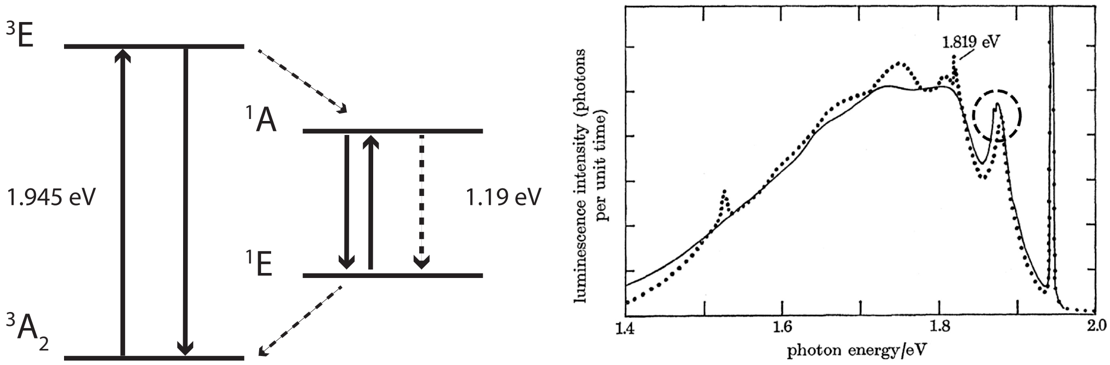

Figure 1.2: (Left) The electronic structure of the NV center. Solid arrows depict optical transitions and dashed arrows represent non-radiative transitions. The ground state is a spin triplet but it also has a metastable singlet state accessible from the excited ^3E state. The states are named after the Mulliken symbols of the irreducible representation associated with the state. (Right) The emission (solid line) and absorption (dashed line, reflected along the zero-phonon line at 637 nm) spectra of the NV center [45].

where μ_B is the Bohr magneton, g is the g-factor (there is an anisotropy associated with the g-factor, but it is small [48] and will be treated as isotropic in this text), g_N is the nuclear g-factor of either ^{15}N or ^{14}N, $d_{gs}^{\|}$ and $d_{gs}^{\perp}$ are the axial and off-axis components of the ground-state dipole moment and δ is the strain field. The values of the dipolar moment components are $d_{gs}^{\perp} = 17 \pm 3$Hz and $d_{gs}^{\|} = 0.35 \pm 0.02$ as reported by van Oort *et al.* [48]. In magnetic sensing applications we can often neglect the nuclear Zeeman, nuclear quadrupole and strain-electric field terms as they are small or only induce broadening when averaged over the an ensemble of NVs in the diamond lattice. When combining expressions 1.1 and 1.2 and dropping said terms we get:

$$H_{gs} = D_{gs}\left(S_z^2 - S(S+1)/3\right) + \mu_B g \mathbf{S} \cdot \mathbf{B}. \tag{1.3}$$

In some cases, especially when dealing with diamonds that have been subjected to large ion/electron implantation doses, the $d_{gs}^{\perp}(E_x + \delta_x)\left(S_x^2 - S_y^2\right) + d_{gs}^{\perp}(E_y + \delta_y)\left(S_x S_y + S_y S_x\right)$ term is substantial and produces ~MHz large splittings between the $m_s = \pm 1$ states.

1.3.1 Optical polarization of the NV center

As mentioned in the introduction to this chapter, one of the outstanding properties of the NV center is that the spin projection state can be polarized and read out optically. The reason for this behavior can be understood by taking another look at the NV energy structure Fig. 1.3. The direct radiative relaxation is equally probable for all spin projections [49], however comparing the relative non-radiative relaxation rates of $m_s = \pm 1$ and $m_s = 0$ magnetic sublevels [50] yields a value of

$$\frac{\Gamma_0}{\Gamma_{\pm 1}} \approx 0.53, \tag{1.4}$$

indicating a strong preference of the $m_s = \pm 1$ spin projection states to relax back to the ground state through the singlet system. The ${}^1\mathrm{E} \rightarrow {}^3\mathrm{A}_2$ intersystem crossing exhibits only a weak spin projection dependence [51] resulting in optical pumping of the $m_s = 0$ state. This phenomenon also accounts for the spin-projection-dependent fluorescence as the nonradiative channel competes with the radiative decay path. As a result the state with the lowest non-radiative relaxation contribution is the brightest.

1.3.2 Optically detected magnetic resonance of the NV center

The simplest implementation of the NV center as a magnetic field sensor is optically detected magnetic resonance (ODMR) spectroscopy. The fluorescence intensity of the NVs is monitored as function of an applied microwave frequency. When on resonance, the microwaves induce transitions between the $m_s = 0$ and $m_s = \pm 1$ spin states. As discussed in section 1.3.1 the $m_s = \pm 1$ states exhibit a lower fluorescence level due to their higher probability of non-radiative decay allowing

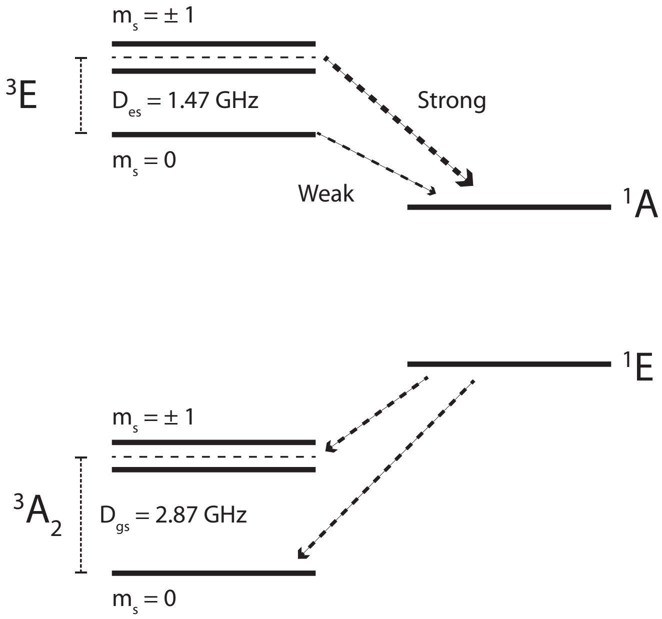

Figure 1.3: NV energy structure including the spin states. The excited state $m_s = \pm 1$ spin projections have a high probability to perform an intersystem crossing to the singlet state while the transition back to the triplet state exhibits far less dependence on the spin projection.

one to determine the energy difference between the two states. The levels are shifted (assuming all other external field, strain, and temperature variables are controlled for) according to the Zeeman term $\mu_B g \mathbf{B} \cdot \mathbf{S}$ in Eq. 1.3. In almost all sensing applications the zero-field splitting D_{gs} is much larger than the magnitude of the magnetic field under investigation. This effectively means that only the axial component of the field is detected, as off-axis terms contribute to the energy splitting only in the second order. A widely used experimental implementation for detecting ODMR is shown in figure 1.4. A complication that arises when using bulk NV diamonds as sensors is that the center can be aligned along any of the four possible orientations with equal probability. While this feature is beneficial in some applications where it is necessary to extract not only the magnitude but also the orientation of the sample field [40], [52], in most cases it complicates the ODMR spectra and lowers the signal contrast. Usually one orientation is isolated by aligning it with the magnetic field axis resulting in the ODMR structure shown in figure 1.5.

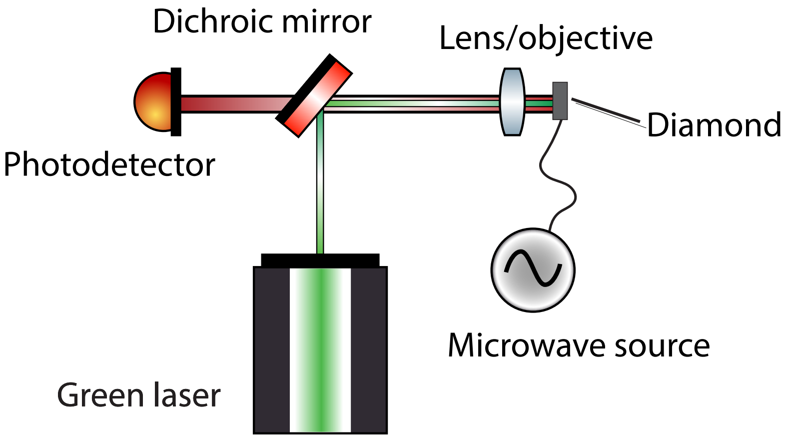

Figure 1.4: A simple ODMR experimental setup. The NVs are excited by a green laser while applying microwaves by a wire, horn antenna or some other means. The fluorescence is collected by a lens/objective and any reflected laser light is deflected by a dichroic mirror.

1.4 Relaxation and decoherence

As mentioned in the introduction, one of the reasons NVs have gained such attention are the exceptional coherence properties. Following the terminology adopted in the field of nuclear magnetic resonance, the longitudinal relaxation time is referred to as T_1, the homogeneous relaxation time as T_2, and the inhomogeneous relaxation time as T_2^*. The T_1 time describes how quickly the system reaches thermal equilibrium once all external driving forces (such as optical illumination in

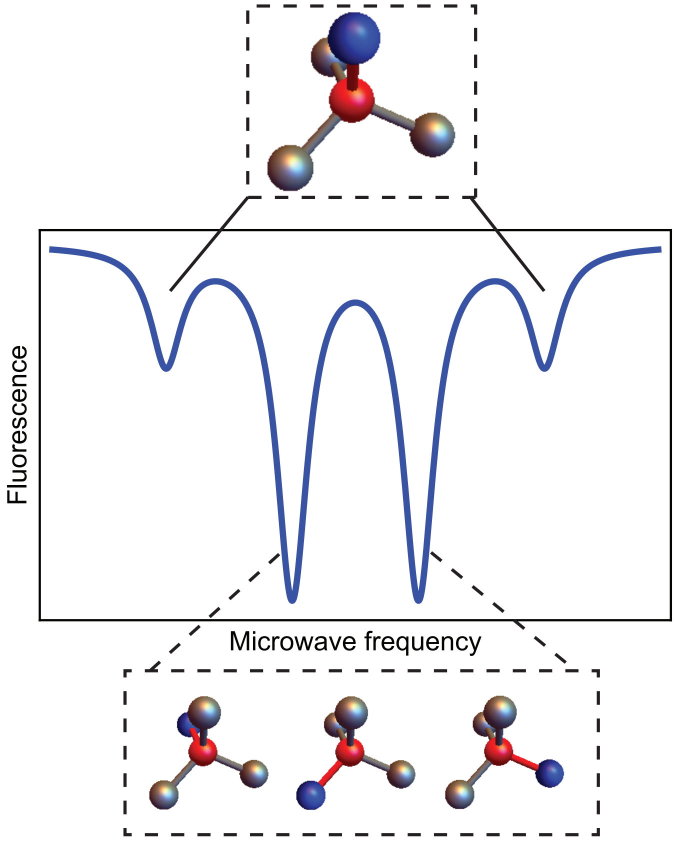

Figure 1.5: ODMR spectra in the case of a field aligned along one of the 4 possible NV orientations. This results in two families of peaks in ODMR spectra. The ones furthest out come from the aligned NVs while the inner lines are due to the 3 misaligned varieties. In the misaligned case the transitions are degenerate due to the C_{3V} symmetry of the defect.

the case of NVs) have ceased [53]. It is governed by the magnetic noise spectrum of the defect environment. The T_2 time describes how spin dephasing occurs and is mostly caused by spin-spin interactions with other paramagnetic spin species within the diamond lattice. The T_2^* time also measures the dephasing time but includes inhomogeneous effects such as magnetic field gradients across the sensing volume and fluctuations of the local spin environment. Various decoupling sequences can be used to cancel out the inhomogeneous influences and T_2 can be thought of as the upper bound of T_2^* (i.e., $T_2 \geq T_2^*$).

1.4.1 Rabi oscillations

The Zeeman sublevels of the NV triplet ground state can be coupled via resonant MW radiation. The effect of the MW radiation on the resonant sublevels can be represented conveniently on the Bloch sphere (see figure 1.6). The poles correspond to pure states while other locations on the surface on the sphere correspond to a

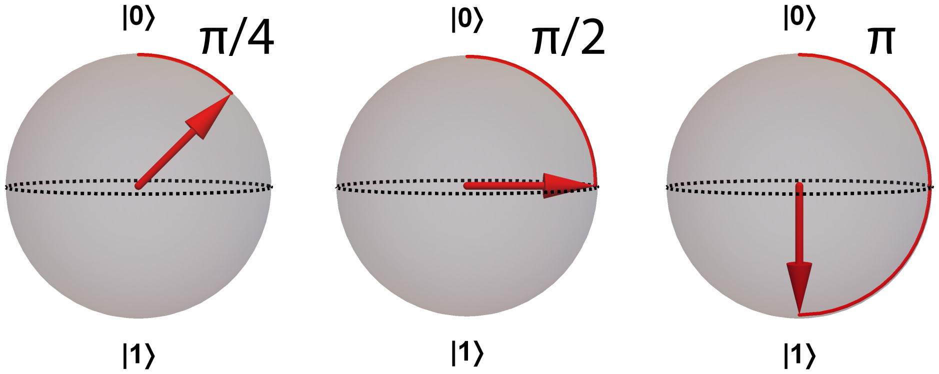

Figure 1.6: Spin state evolution under the influence of MW radiation. The state evolves by precessing around the meridian the precession angle depends on the phase accumulation $\phi(\tau) = \int_0^\tau B(t)\gamma dt$. By turning the MW power off at the right moment, a specific rotation can be achieved and is commonly referred to by the rotation angle i.e. "a $\pi/2$ pulse".

mixed state of the form:

$$|\psi\rangle = \cos\theta|0\rangle + \sin\theta e^{i\phi}|1\rangle, \tag{1.5}$$

where θ is the polar angle describing the relative contribution of each of the basis states to $|\psi\rangle$ and ϕ is the azimuthal angle describing the phase of the *wavefunction.

If we assume no relaxation and no other couplings to external fields, under the influence of MW radiation the state will precess along the meridian of the Bloch sphere with the population oscillating between the two base-states. The oscillation frequency scales as the the MW mediated coupling between the two states. In the case of spin transitions in the MW ground state the interaction Hamiltonian is simply $\hbar\gamma B_1$ and the Rabi frequency is $\Omega = \gamma B_1$, where γ is the gyromagnetic ratio of the electron and B_1 is the MW field component transverse to the spin polarization.

Since the transverse MW field amplitude is rarely precisely known the duration of a π (or any other duration) pulse is determined by a scheme shown in figure 1.7. The pulse duration is swept and the fluorescence monitored. This results in oscillations in the fluorescence level corresponding to population oscillations between the $|m_s = 0\rangle$ and $|m_s = \pm1\rangle$ sublevels. The oscillations also exhibit a decay envelope both due to inhomogeneities in the B_1 field and intrinsic dephasing due to the local spin environment. The characteristic decay time is often referred to as $T_{1\rho}$.

1.4.2 Homogeneous transverse (T_2) relaxation

Homogeneous transverse relaxation affects all the spins in the ensembles in the same way, excluding inhomogeneous factors such as spatial variation in the strength of the magnetic field. The inhomogeneous factors can usually be cancelled out by a decoupling the target spins from the environment. One of the simplest ways of decoupling the NVs from the extrinsic environment is by a Hahn-Echo sequence shown in figure 1.8.

Initially the NVs are polarized in the $m_s = 0$ state by a laser pulse. Then a resonant MW $\pi/2$ pulse is applied transferring the state to the equatorial plane of the Bloch sphere. Let us assume the MW are in resonance with the $|m_s = 0\rangle \rightarrow |m_S = 1\rangle$ transition. Then the superposition state can be written as:

$$|\psi(t=0)\rangle = \frac{1}{\sqrt{2}}\left(|0\rangle + |1\rangle\right). \tag{1.6}$$

During the first evolution period the state evolves under the influence of the magnetic field of the local spin environment accumulating a phase $\phi = -\gamma \int_0^\tau B(t)dt$. After the first evolution period the systems state can be written as:

$$|\psi(t=\tau)\rangle = \frac{1}{\sqrt{2}}\left(|0\rangle + e^{i\phi}|1\rangle\right). \tag{1.7}$$

Afterwards, a resonant π pulse is applied to the NVs, essentially flipping the sign of the accumulated phase during the first free precession period. During the next free precession period the NV continues to accumulate phase $\phi_2 = -\gamma \int_\tau^{2\tau} B(t)dt$. The net phase accumulation is then $\phi_{tot} = \phi_2 - \phi_1$., Stationary or slow contributions are cancelled. Finally, another $\pi/2$ pulse is applied. The final state of the system is a function of the total accumulated phase during both free precession periods. The state is read out optically by applying another laser pulse and monitoring the fluorescence.

There are many different variations of decoupling techniques besides Hahn-echo (CPMG, XY8-N etc.) varying in number of pulses, pulse spacing, phase control, affected spin species etc., but it is important to realize that most of them effectively act as frequency filters. That means that not only the inhomogeneous part is suppressed, but a filter function is also applied to the noise of the contribution from the local spin bath. As a result the decoupling sequences with a narrower bandwidth will result in longer coherence times.

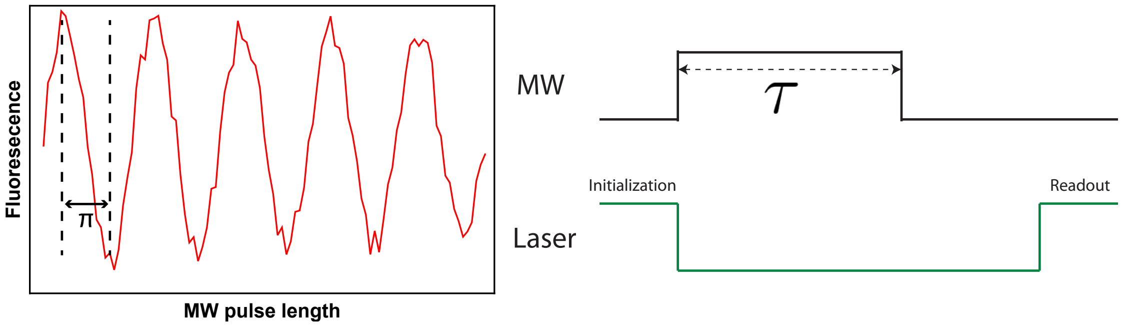

Figure 1.7: Measurement of Rabi oscillations. (left) Experimental data from a Rabi measurement in a bulk NV diamond. The time period from peak to trough is equal to the length of a π pulse. (right) The pulse sequence used to measure Rabi oscillations. The time between initialization and readout is kept fixed while the length of the MW pulse is varied.

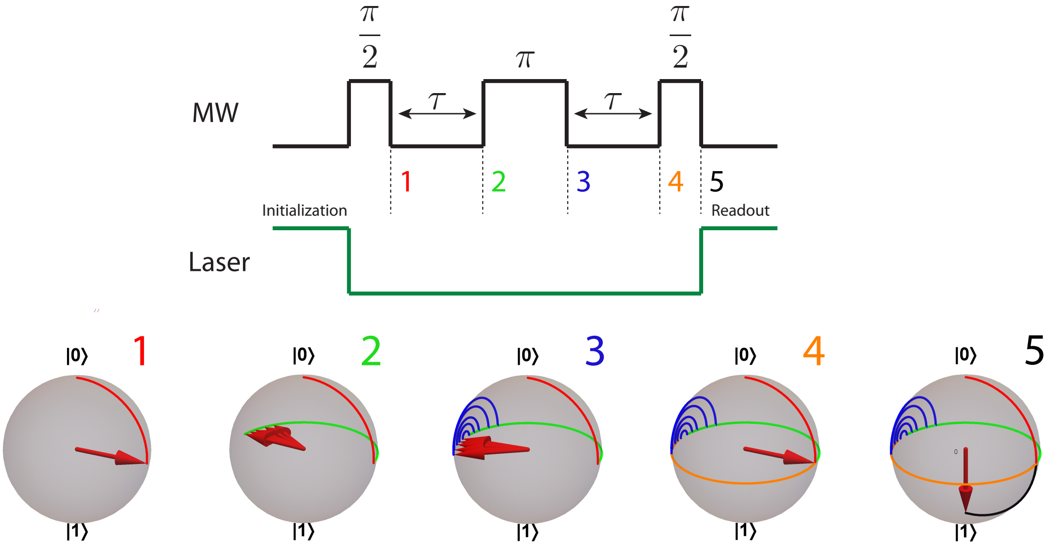

Figure 1.8: The Hahn-echo pulse sequence (top) and the corresponding evolution of the state on the Bloch sphere (bottom). Each distinct step is color-coded.

1.4.3 Inhomogeneous transverse (T_2^*) relaxation

The inhomogeneous relaxation characterizes the overall dephasing of an ensemble of NVs due to the different local or macroscopic environments they inhabit. Typical sources of inhomogeneity are magnetic field gradients, non-uniform temperature distributions, and proximate paramagnetic spin species coupled strongly to some NVs but not others. The T_2^* time is measured using a Ramsey sequence (see Fig. 1.9), which is very similar to the already described Hahn Echo sequence absent the π pulse. The missing π pulse means that inhomogeneous effects will not be cancelled as in the Hahn echo experiment. This means that this technique is sensitive to low-frequency and DC components of the local magnetic environment.

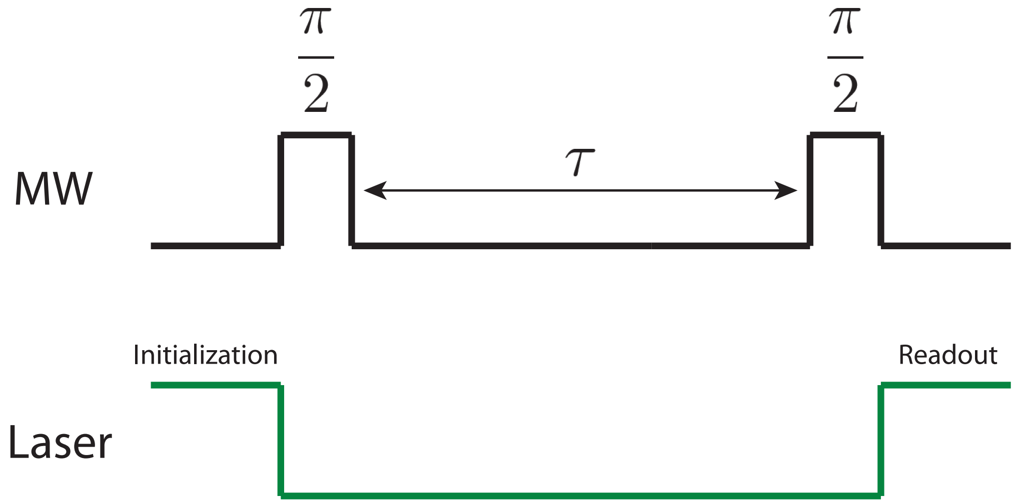

Figure 1.9: The Ramsey pulse sequence.

1.4.4 Longitudinal relaxation (T_1)

The longitudinal relaxation time T_1 describes how long it takes the spins to reach thermal equilibrium. Both phononic processes and dipole-dipole couplings to other spins contribute to the relaxation. Which mechanism dominates is strongly influenced by both the diamond's intrinsic properties as well as environmental variables such as an external magnetic field and temperature. At low fields the splitting between spin sublevels is dominated by the dipole-dipole interaction ($D = 2.87$ GHz). As the diamond phonon density of states is very low in this region, the phonon part of the relaxation is mostly due to two-phonon Orbach and Raman processes. This was confirmed by T_1 temperature dependence studies [54]–[57] where the following relaxation rate dependence was obtained:

$$\frac{1}{T_1} = A_1(S) + \frac{A_2}{\exp\frac{\Delta}{k_B T} - 1} + A_3 T^5. \tag{1.8}$$

The $A_1(S)$ is sample-dependent, the second term describes a two-phonon Orbach process [58] at room temperature and below, where $\Delta = \hbar\omega_{loc}$ is the energy of the localized phonon mode, and the final term describes the two-phonon Raman process [57].

The other contributors to the longitudinal spin relaxation are magnetic noise from the environment such as ^{13}C (natural abundance 1.1%), P1 centers, other NVs, or surface spins in case of shallow NVs. The relaxation mechanism can be thought of as the driving of the spin transitions by the magnetic noise and the relaxation rate is proportional to the power at the NV transition frequency. This dependence can be used to probe the spin bath surrounding the NV center by monitoring the T_1 as function of the external magnetic field. An example of this is shown in figure 1.10. When the energy of a transition for the NV matches that of another spin species, such as the P1 center, both the spins can simultaneously change their spin states causing the NV T_1 time to decrease. It can be used to probe the spin-environment outside the diamond as shown in [59]–[61], where spin species were identified by a spike in the magnetic noise spectrum at their Larmor frequency.

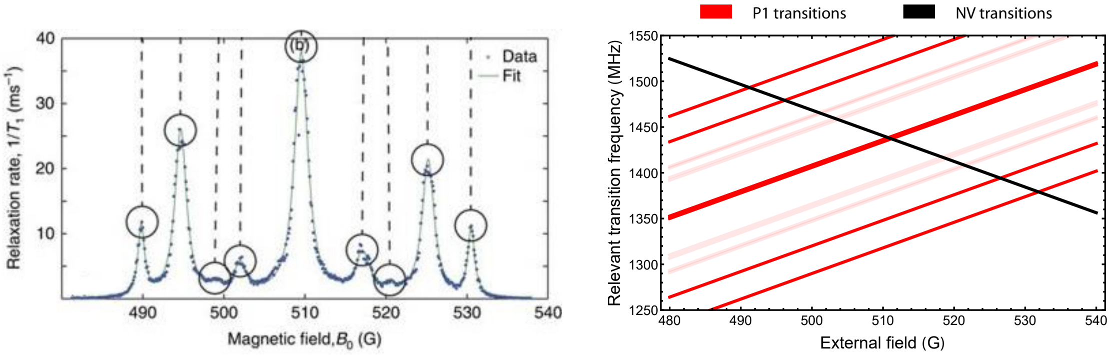

Figure 1.10: Decrease in the T_1 time due to cross-relaxation through the P1 centers. (left) Longitudinal relaxation rate as a function of an external field (applied along one of the 4 diamond crystal orientations), figure originally from [62]. The dashed lines indicate energy matching conditions (crossing points on the figure on the right side). A sharp increase is seen where the energy of an NV spin flip matches that of a P1. (right) Transition frequency as a function of applied field. P1 transitions are marked in red (allowed transitions for the NV) and pink (disallowed transitions for the NV), NV $|m_s = -1, m_I\rangle \rightarrow |m_s = 0, m_I\rangle$ transition is in black.

The pulse sequence used to measure the T_1 time is shown in figure 1.11. This type of sequences can also be used in an imaging setup by gating the exposure time [59], [60].

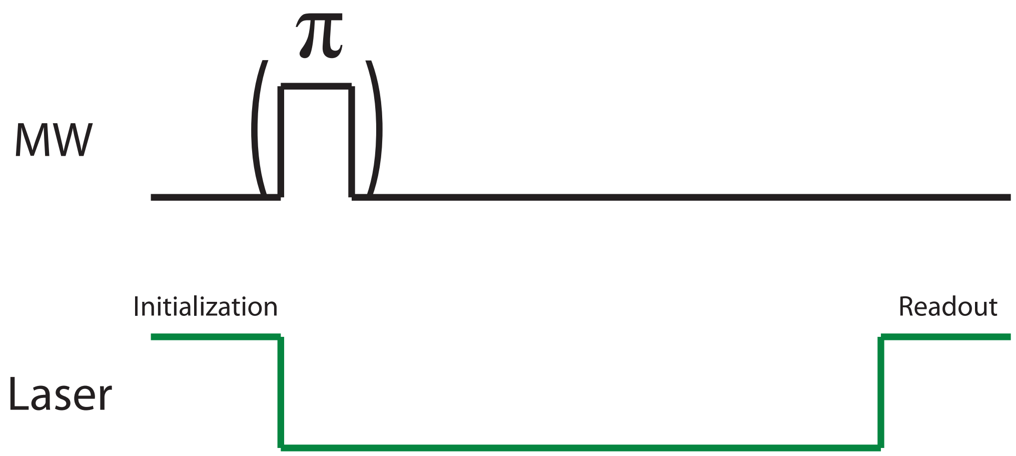

Figure 1.11: Measurement sequence for the T_1 relaxation time. The MW π pulse after the initialization is optional. Often measurements with and without the MW pulse are done in succession and then subtracted cancelling out any common-mode noise present in the system as well as isolating only the NVs resonant with the applied pulse.

1.5 Magnetometry with the NV center

There exist several different approaches to magnetometry with ensembles of NV centers depending on the frequency and bandwidth of the signal, whether full vector information is necessary or whether it is necessary to suppress temperature/strain related effects. This section contains a brief overview of the more widely used detection techniques.

1.5.1 CW-ODMR based detection

As briefly mentioned in section 1.3.2 a simple way of measuring the magnetic field is by continuously sweeping an applied microwave frequency and monitoring the NV centers' fluorescence. When the MW frequency is on resonance with either on of the $|m_s = 0\rangle \rightarrow |m_s = \pm 1\rangle$ transitions it results in a dip in fluorescence. The shot-noise limited sensitivity η is given by:

$$\eta \approx \mathcal{P}_{\mathcal{F}} \gamma_{NV} \frac{\Delta \nu}{C\sqrt{R}}, \tag{1.9}$$

where $\mathcal{P}_{\mathcal{F}}$ is a numeric factor related to the line shape of the resonance ($\mathcal{P}_{\mathcal{G}} \approx 0.7$ for a Gaussian line shape and $\mathcal{P}_{\mathcal{L}} \approx 0.77$ for a Lorentzian line shape), γ_{NV} is the NV gyromagnetic ratio, $\Delta\nu$ is the FWHM of the resonance and and R is the photon collection rate. While CW-ODMR has a relatively simple experimental realization it suffers from decreased sensitivity due to microwave- and laser induced power broadening. To achieve optimal sensitivity [17], [63], [64] optical, MW, and intrinsic contributions to the dephasing time should be roughly equal, in which case:

$$\eta \approx \mathcal{P}_{\mathcal{F}} \gamma_{NV} \frac{1}{C\sqrt{R T_2^*}}. \tag{1.10}$$

A common variation on the experimental setup presented in figure 1.4 is the addition of a lock-in amplifier. The microwave frequency is modulated across either of the transitions of the aligned NV centers (see figure 1.5). The voltage from the photo-diode is then mixed with the modulation signal, which effectively separates the information-carrying part of the signal from the more prevalent low-frequency noise contributions and thereby narrows the acquisition bandwidth.

There are also several practical problems that commonly arise and negatively impact the capabilities of the NV magnetometer:

- **Temperature** The laser light used to excite the NV centers can also cause an inhomogeneous temperature distribution to form. The transition frequency exhibits a temperature dependence of 75kHz/K which can cause either a broadening of the spectral line in a bulk magnetometer or create visual artifacts in field maps from magnetic imaging setups. A common way to address this problem is by measuring both of the $|m_s = \pm 1$ transitions and using the difference of the transition frequencies to obtain the field value. Since the temperature affects the dipolar splitting constant D [47] (see equation 1.1) the temperature contribution to the energy shift is identical for both transitions and is cancelled out when subtracting them.

- **Polarization of optical and MW fields** The NV center can absorb only light polarized transverse to the quantization axis (the axis connecting nitrogen to the vacancy site). This can result in sub-optimal excitation efficiency for certain experimental geometries especially if using (110)-face polished diamonds. However in certain situations this effect can be beneficial.

- **Magnetic and MW field homogeneity** As discussed before inhomogeneous magnetic field distributions can decrease the T_2^* time and hence lower sensitivity (eq. 1.10). A non-uniform MW field can lead to power broadening or insufficient driving strength which, in turn, causes line-broadening or diminished contrast decreasing the sensitivity of the sensor.

1.5.2 Pulsed magnetometry based detection

As mentioned above, the CW approach is limited by power broadening due to the optical or MW fields. By separating the phase accumulation and readout stages of the measurement it is possible to avoid optically induced line broadening. A simple implementation of the pulsed approach is the Ramsey sequence briefly discussed in section 1.4.3. Assuming a DC field and both of the pulses having the same phase, the state of the NV center evolves as $|\psi(t)\rangle = \frac{1}{\sqrt{2}}\left(|0\rangle + e^{-i(\gamma m_s B t + \pi/2)}|m_s\rangle\right)$ where $m_s = \pm 1$ depending on the MW frequency of the $\pi/2$ pulse. At the end of the phase accumulation time the final pulse projects the state back into the $|0\rangle, |m_s\rangle$ manifold with a probability amplitude dependent on the accumulated phase:

$$e^{iS_z\pi/2}|\psi\rangle = \frac{1}{\sqrt{2}}\left[\left(1 - e^{-iB\gamma m_s \tau}\right)|0\rangle - i\left(1 + e^{-iB\gamma m_s \tau}\right)|m_s\rangle\right], \tag{1.11}$$

where τ is the total phase accumulation time. In a shot-noise-limited assuming optimum phase accumulation time ($\tau = T_2^*$) case this leads to a sensitivity of:

$$\eta = \frac{\gamma}{C\sqrt{RT_2^*}}. \tag{1.12}$$

Note that the sensitivity is proportional to $\sqrt{T_2^*}$ rather than T_2^* as it was in the case of CW-ODMR (see eq. 1.10). In addition to circumventing the power-broadening problem, pulsed magnetometry enables the use of dynamic decoupling sequences to extend the coherence time T_2^* of the NV spins. The simplest example of this is the Hahn-Echo sequence already discussed in section 1.4.2, which effectively AC couples the sensor cancelling any contributions oscillating more slowly than τ. A popular class of decoupling sequences are based on equidistant pulses, examples of these are the Carr-Purcell-Meiboom-Gill (CPMG), XY8-N, and others. Intuitively they can be understood as behaving as bandpass filters on the magnetic field noise. Only the net power in the measurement acquisition band can dephase the NV spin resulting in an increase in the coherence time T_2^*. A more rigorous treatment and performance comparison of different pulse sequences can be found in a paper by Wang et al. [65].

Chapter 2

NV spin relaxation

One of the reasons NV centers are excellent quantum sensors are their room-temperature coherence properties. The main factor influencing the NV spin coherence time are interactions with other paramagnetic spin species which can be difficult to predict both due to the inherit complexity of modelling multi-spin dynamics and the richness of defects present in diamonds.

To discuss these interactions the NV community has adopted the language from the NMR field distinguishing two kinds processes. T_1 describes the population (longitudinal) relaxation rate and T_2 describes the coherence (transverse) relaxation rate. In literature sub- and super-scripted values are also often used ($T_{1\rho}$, T_1^*, T_2^* etc.) for effective relaxation time values that are different from the true relaxation times either due to the measurement process itself perturbing the spin system (such as an inversion recovery pulse introducing mixing effects in coupled systems [66]), inhomogeneous broadening caused by external field gradients or continuous driving fields applied to the spins.

While NV centers exhibit excellent coherence properties they experience significant degradation as the defect concentration increases. On the other hand increasing the NV concentration is desirable as the fundamental limit in bulk NV sensors is shot-noise which scales inverse to the fluorescence level and thus the number of NVs. Furthermore, while sophisticated diamond engineering can potentially minimize the deleterious affect of other defects on the coherence time, there exists a hard limit on the coherence time T_2 imposed by the population relaxation time T_1. It states that $T_2 \leq 2T_1$. In this section I will start by giving a brief overview of the most important dephasing sources and when the T_1 limit might become relevant. The second part of the chapter will summarize published [67] experimental work in studying the T_1 scaling with NV concentration.

2.1 Overview of the relaxation mechanisms of the NV center

When discussing the sensitivity of the NV center the effective transverse relaxation rate T_2^* plays an exceedingly important role as the phase accumulation and thus observed signal contrast scales linearly with this parameter. The square-root scaling in the CW-ODMR sensitivity is (eq. 1.10) scales as the root of T_2^* is due to the fact that a lower laser excitation must be used to avoid power broadening of the line [64] leading to a lower photon collection rate. In pulsed experiments (Ramsey or Pulsed-ODMR [68], [69]), if the phase acquisition time is smaller than the time spent on the initialization/readout of the NV center, the scaling is approximately linear as the increase in overall measurement time is negligible while the signal strength scales linearly with the accumulated phase.

The contributions to the effective relaxation time can be written as [63]:

$$\begin{aligned}\frac{1}{T_2^*} =&\frac{1}{T_2^*\{\text{electronic spin bath}\}} + \frac{1}{T_2^*\{\text{nuclear spin bath}\}}+ \\ &+ \frac{1}{T_2^*\{\text{strain gradients}\}} + \frac{1}{T_2^*\{\text{electric field noise}\}}+ \\ &+ \frac{1}{T_2^*\{\text{magnetic field gradients}\}} + \frac{1}{T_2^*\{\text{temperature gradients}\}}+ \\ &+ \frac{1}{T_2^*\{\text{other}\}} + \frac{1}{2T_1}.\end{aligned} \tag{2.1}$$

Magnetic/electric field gradients and temperature are extrinsic influences related to the experimental setup itself. In nitrogen rich (>1 ppm) the dominant dephasing mechanism is dipolar interactions between the NV and P1 centers [62], [70]–[72]. For dilute concentrations the dephasing time has inverse linear scaling with the paramagnetic spin concentration [73] with a scaling factor of $\frac{1}{T_2^*\{\text{P1 centers}\}} = (101 \pm 10)\text{ms}^{-1}\text{ppm}^{-1}$ reported by Bauch et al. by studying NVs in both natural abundance and isotopically purified diamonds with a nitrogen concentration spanning 5 orders of magnitude.

As mentioned before, the consensus of the NV community is that the most probable electron donor for the NV$^-$ center is the P1 defect [23], [24]. With increasing NV conversion efficiencies the P1 population is depleted leading to a regime where the dephasing contribution of NV-NV coupling can be comparable or even overtake the NV-P1 contribution. The conversion efficiency depends on several factors:

- Energy of the particles used to create vacancies. This effect is quite pronounce if ions are used to form vacancies [74] where higher energy ions create more vacancies-per-ion resulting in a higher yield. In the case of electron irradiation to the density of mono-vacancies then for electrons higher energy mostly results in higher penetration depth rather then increase in vacancy density [75].

- Annealing in vacuum or an inter atmosphere promotes the mobility of vacancies until they are captured by a substitutional nitrogen and forming the NV center

- It has also been reported that electron irradiation promotes NV center formation [76]. An interesting result reported by Schwartz et al. [77] also reports increased NV yield where even low-energy ($\leq$30 keV) electron irradiation followed by an annealing step increases the yield 1.8x when compared to a process where the electron irradiation step was omitted, signaling an alternative formation mechanisms besides vacancy-trapping by substitutional nitrogen.

The decoherence rate scaling with NV center concentration is also steeper due to the higher spin multiplicity of the NV center, the decoherence rate scaling with concentration for NV centers than it is for P1 defects. Barry and Schloss et al. [63] estimating (based on figures obtained for the P1 center) it at $\frac{1}{T_2^*\{\mathrm{NV}_{\parallel}^-\}} \approx$ 247ms^{-1}ppm^{-}1 and $\frac{1}{T_2^*\{\mathrm{NV}_{\nparallel}^-\}} \approx$ 165ms^{-1}ppm^{-}1 for NVs aligned along the same direction and NVs aligned along different crystallographic axes correspondingly.

Below the 1 ppm nitrogen concentrations the dephasing contributions of ^{13}C in natural abundance diamonds cannot be neglected. For natural abundance diamonds this limits the T_2^* time to around 1 µm. In the dilute limit (N[^{13}C]$\leq$ 1.1%) the ^{13}C limited dephasing rate also has linear concentration scaling: $\frac{1}{T_2^*\{^{13}\mathrm{C}\}} = A_{13C}\mathrm{N}[^{13}\mathrm{C}]$ with $A_{13C} \approx 0.1\mathrm{ms}^{-1}\mathrm{ppm}^{-1}$ [63], [78]. The linear scaling in concentration of the dephasing rates of all of these paramagnetic species can be intuitively understood by considering the following: the dephasing time has a linear dependence on the coupling strength. Dipolar coupling has a $1/r^3$ scaling while the average distance between two substitutional nitrogen atoms has scales as $N(P1)^{1/3}$ with concentration.

The dephasing time of the NV spin ensemble can be significantly increased by employing refocusing the ensemble with microwave pulses. The simplest refocusing method is the Hahn-Echo pulse sequence already discussed in section 1.4.2. The refocused coherence time T_2 can be one to two order of magnitude higher than T_2^*. The refocusing procedure also makes the NV center sensitive only to AC fields. In addition if the length of the Hahn-Echo sequence coincides with an integer multiple of the ^{13}C Larmor period a sharp drop in the coherence time of the NV spin ensemble. If the time τ is swept, this manifests as collapse and revival beats under the exponential decay of the fluorescence signal envelope (see Fig. 2.1). An excellent experimental study of this phenomena can be found in the work by Stanwix et al. [79].

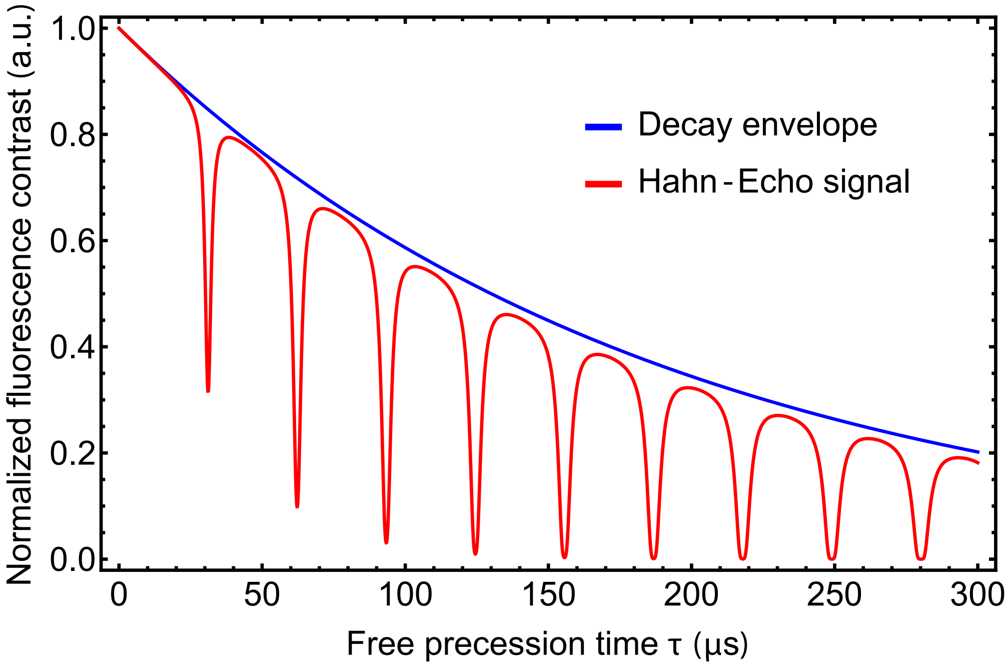

Figure 2.1: Simulated fluorescence signal at $B_0 = 300\text{G}$ as a function of free precession time τ in a NV Hahn-Echo experiment. At this field the Larmor period is $T_L = 31.11\mu\text{s}$ which is equal to the spacing between the dips in fluorescence contrast.

The decoherence time T_2 is fundamentally limited by the longitudinal relaxation time T_1 with $T_2 \leq 2T_1$. For ensembles in room temperature this value is of order $\sim$ms [47], [55] and is normally dominated by the phonon induced spin relaxation. However if the NV center is coupled (most often through magnetic dipole-dipole interactions) to a spin bath such that the energy of a dipole-allowed transition in the NV ground state system matches a dipole transition in the spin bath, the T_1 time can be substantially reduced. Such a situation is realized at around 510 G [62], [80], [81] where the NV $|m_s = 0\rangle \rightarrow |m_s = -1\rangle$ transition matches the P1 spin transition (assuming the field is aligned along the [111] direction). This effect has been successfully exploited for detection purposes. The sensitivity is equal to that of AC sensing through dynamic decoupling sequences [82] while being much easier to implement experimentally. The ease of experimental implementation has also enabled wide-field relaxometric imaging experiments [59], [83]. In most cases, however, any decrease in the T_1 time is detrimental to the overall sensor performance.

A spin system that is always in resonance (energy-matched and dipole-allowed transitions) with the NV center are other proximal NV centers. At non-zero magnetic fields aligned along one of the diamond axes only the aligned components fulfill the resonance energy-matching condition, however, as the field decreases and all of the spin-components become degenerate a drop in longitudinal relaxation times is observed. To probe the NV concentration related change in longitudinal relaxation rate we implanted a diamond chip with different, controlled doses of vacancy-forming radiation doses and monitored to corresponding T_1 time.

2.2 Experimental realisation and vacancy distribution

To control for other external parameters such as paramagnetic impurity concentration we used a Schottky field emitter electron source from a TEM microscope to create vacancies in type 1b HPHT diamond with around around 200 ppm of substitutional nitrogen. 13 spots on the same chip were irradiated with different doses (same fluence) with an acceleration voltage of 200 kV forming a layer between ~7 μm and ~ 20 μm thick. Additionally 4 spots were irradiated with the same dose but lower electron flux to control for any local charging effects. No significant differences between the spots irradiated with different electron fluxes were observed. We also assume, and this is corroborated by confocal microscopy data, that the NV distribution after annealing follows the vacancy distribution.

Two different approaches were used to estimate the vacancy distribution: a Monte-Carlo simulation using the CASINO software package [84] and from the total stopping power reported by ESTAR [85]. The results from the Monte-Carlo method are shown in Fig. 2.2. A 1000 electrons with 200 keV energies impacting 100x100x100 μm diamond block were simulated. For an ideal diamond crystal the minimum necessary energy for an electron to form a vacancy is ~180 keV [86] (although the necessary energy is smaller if the vacancy is formed near a defect such as a P1 center [87]).

The CASINO simulation shows that the mean the electrons do not retain enough energy to displace carbon atoms beyond the depth of a 7μm. An alternative approach is to use the ESTAR estimate for the CSDA (continuous slowing down approximation) range. This method estimates that electrons on average do not have enough energy to form a vacancy after travelling around 28μm in diamond, however the projected path-length on normal to the diamonds surface can be much shorter. Finally paper by Kim et. al [88] show a NV fluorescence distribution peaking at 10 μm and tailing off at 40 μm under very similar implantation conditions also for a type IIb diamond. While the estimations methods yield differ-

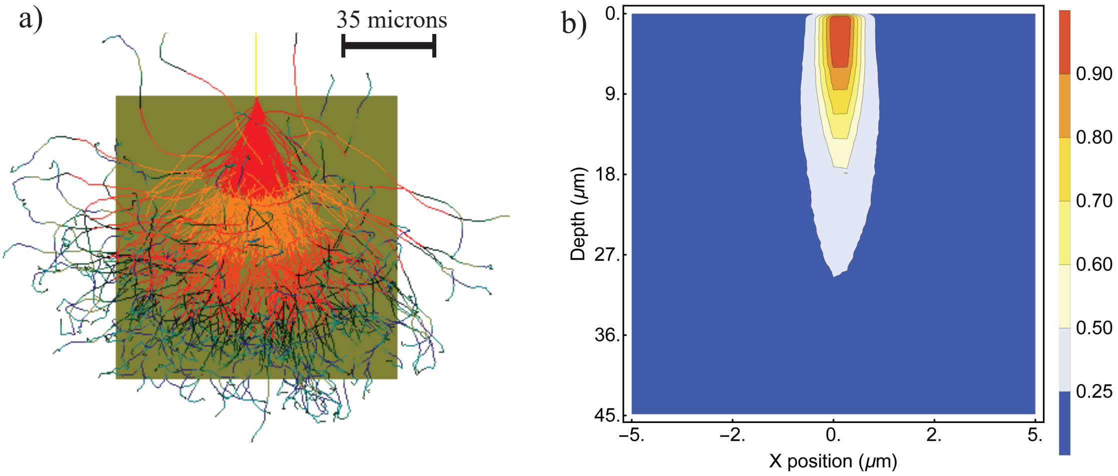

Figure 2.2: CASINO simulation of 200 keV electron beam impacting a 100x100x100 μm diamond block. a) Trajectories of simulated electrons. Color scale represents the energy of the electron. b) Averaged normalized depth/energy distribution over 1000 simulated trajectories. Only electrons retaining at least 90% of their initial energy can displace carbon atoms and produce vacancies.

ent results they are not necessarily contradictory. Electron energy loss per length travelled exhibits huge non-Gaussian fluctuations with long tails; while most of the electrons lose their ability to form vacancies beyond the 10 μm depth shown in Fig.2.2 a small subset of the population retain enough energy much deeper in the diamond.

After irradiation the sample was heated in a nitrogen atmosphere for three hours at 800°C to facilitate vacancy diffusion and capture by substitutional nitrogen defects to form NV centers. A wide-field fluorescence image of the irradiated spots is depicted in figure 2.3 and the corresponding irradiation parameters are shown in table 2.1. The concentration estimates were obtained by assuming a linear fluorescence intensity/concentration dependence and scaling from a diamond with a known NV center concentration of 10 ppm.

The experimental setup used to measure the T_1 is shown in Fig. 2.4. It consists of a custom-built epifluorescence microscope where a 512 nm diode laser is used to excite the NV centers through an objective lens (f = 4.5mm NA=0.55). The laser power at the site of the diamond is around 7 mW focused over a 50 μm spot. The microwaves were supplied through a 0.071 diameter wire placed adjacent to the sensing area.

The fluorescence was separated from the excitation light by a dichroic mirror and additional lowpass optical filter. The objective-sample distance was adjusted based on fluorescence intensity aiming to achieve the highest value. The filtered fluorescence signal was then focused on an avalanche photodiode and read-out

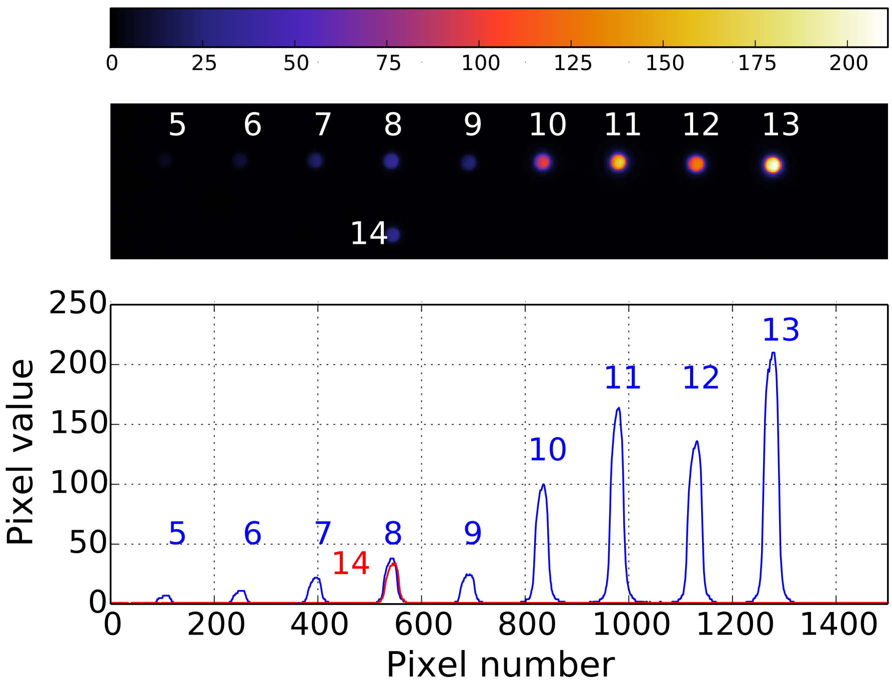

Figure 2.3: A fluorescence image of the irradiated spots on the diamond. The plot underneath the fluorescence image depicts the pixel value across a line-cut through all of the points.

using an oscilloscope.

The excitation light was pulsed using an acoust-optic modulator (rise time $\sim 50ns$. The pulse length was 50 μs to completely repump the NVs in the $m_s = 0$ state before repeating the measurement. The microwaves were pulsed by a TTL controlled switch. Both the AOM, the MW switch and the oscilloscope trigger signal were controlled by a programmable pulse generation card with a 500 MHz clock ensuring synchronization and more than adequate temporal resolution. The length of the MW pulse was determined by doing a prior Rabi measurement as described in section 1.4.1.

To magnetic field was applied through 3 pairs of Helmholtz with a known current/field dependence. The field alignment is done by monitoring the ODMR signal and adjusting the applied field direction until a spectrum resembling that shown in Fig. 1.5. The spectrum also informs on the MW resonance frequency at a particular field.

The T_1 time was measured using the method described in 1.4.4. Two data-sets were taken - one without the optional microwave pulse and the second with the pulse - and subtracted to isolate the relaxation dynamics of only one NV spatial subgroup. The obtained relaxation curves and subtracted result are shown in Fig. 2.5.

Spot Nr.	Integrated Fluorescence Intensity (arb. units)	Electron Dose (C/cm^2)	Electron Flux (A/cm^2)	Estimated NV^- Concentration (ppm)
5	1400	1.76	5.6×10^{-2}	0.2
6	2600	3.36	5.6×10^{-2}	0.3
7	5700	6.72	5.6×10^{-2}	0.7
8	10000	13.6	5.6×10^{-2}	1.2
9	6300	27.2	5.6×10^{-2}	0.7
10	29000	54.4	5.6×10^{-2}	3.3
11	50000	108.8	5.6×10^{-2}	5.5
12	39000	208	5.6×10^{-2}	4.3
13	65000	400	5.6×10^{-2}	7.1
14	8300	9.76	4.1×10^{-2}	3.9

Table 2.1: Irradiation parameters for the different spots, Integrated (red) fluorescence intensity and electron dose and estimated NV^- concentration for the different spots shown in Fig. 2.3.

2.2.1 Results and discussion

In low NV concentration samples the phonon mediated population relaxation is dominant [47] and the relaxation curve is simple decaying exponential. However in the HPHT diamond were NV concentrations can be high the NV-NV couplings also contribute to the relaxation rate. Additionally since the coupling is dipolar and thus strongly dependent on the distance between two centers the relaxation rates can vary between different members of the ensemble under investigation. To account for this effect on the ensemble fluorescence signal the data are fit with with a stretched exponential, which can be interpreted as the weighed mean of relaxation processes happening at different rates [89]. The stretched exponential takes the form:

$$N(t) = N_0 + N_1 e^{-\left(\frac{t}{T_1}\right)^{\beta}}, \tag{2.2}$$

where T_1 is the effective population relaxation time and β is a numerical factor from $(0, 1]$. For $\beta = 1$ we recover the mono-decaying exponential and the relaxation rate distribution is effectively a δ function.

Figure 2.6 shows the magnetic field dependent effective relaxation rate $1/T_1$ obtained by fitting the measured decay curves for four different concentrations. The relaxation rates agree with results reported previously at room temperatures for similar diamonds [54], [55]. There is an increase in the rate around zero field

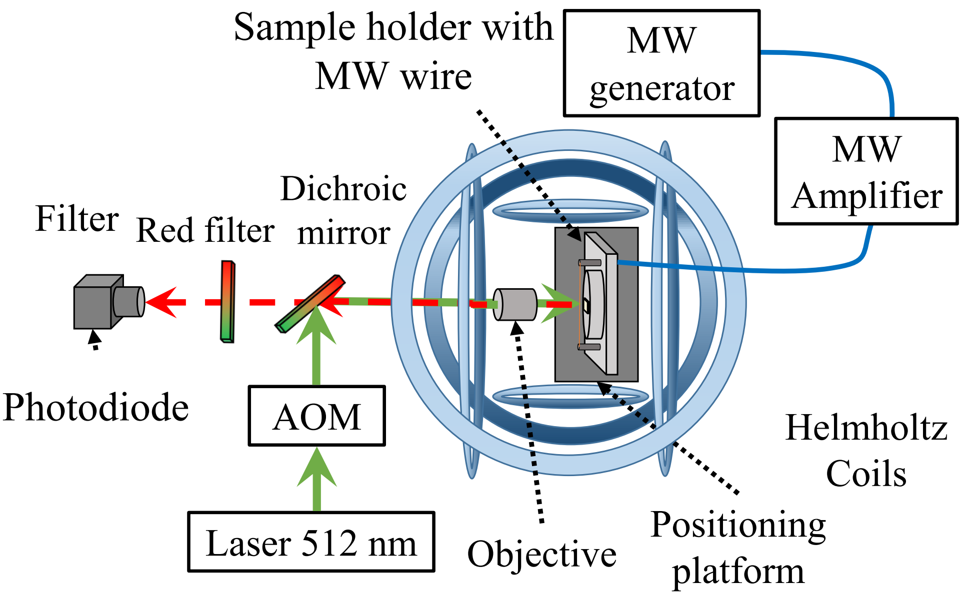

Figure 2.4: The experimental setup. 3 pairs of coils in a Helmholtz configuration were used to apply an external magnetic field along of the diamond crystal orientations. A 512 nm diode laser was used to excite the NV centers through a home-brew epi-fluorescence microscope. MW radiation was applied through a 100 μm diameter placed next to the NV spots. finally

which can be explained by the fact that all the NV spatial subgroups are degenerate and the energy matching criterion is fulfilled increasing the number of relaxation partners. A hint of a relaxation rate increase can also be seen near the crossing point which is the result of partial overlap of the transition frequencies of the differently oriented NV centers.

In most sensing applications an external field is applied to isolate one of the four spatial NV subgroups. The T_1 and β fit values for this situation are shown in Fig. 2.7. For low NV concentrations the effective relaxation rate is slower and the parameter β approaches unity which is agreement with previously reported results [55], [67]. As the NV concentration increases the relaxation rate increases in a linear fashion. This is consistent with the hypothesis that dipole interactions become the dominant contributor to the overall relaxation rate with increased NV concentration. The dipole-dipole interaction strength scales as r^{-3} while the average distance between two NV centers scales as $[\mathrm{NV}]^{-1/3}$. The relaxation rate distribution also becomes increasingly wider as the parameter β moves further away from unity. This also supports the hypothesis of NV-NV dipole interactions playing an important role at these concentrations as is illustrated in Fig. 2.8. The plot is based on a toy-model where N points are placed randomly in a volume. Then the interaction strength with the closest neighbouring (taken to be the equal

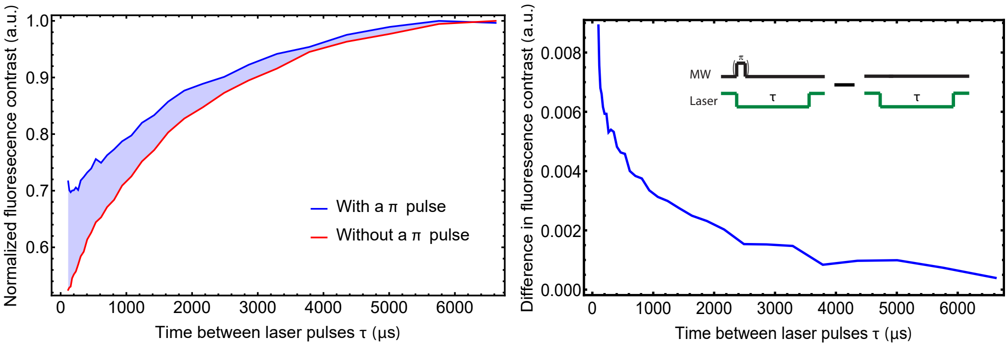

Figure 2.5: A typical T_1 measurement. (left) Fluorescence contrast as a function of time between laser pulses with an π pulse delivering (initially all the population is in the $m_s = |\pm 1\rangle$ state) without the π pulse (initially all the population in the $m_s = |0\rangle$ state). (right) The subtracted decay curve suppressing both relaxation dynamics of the other NV spatial subgroups and other common mode contributions. The curve is essentially the light-blue area in figure on the left.

to $1/r^3$) is recorded. As the number of points increase the tail of the distribution becomes longer. Since the T_1 relaxation rate is also proportional to the interaction strength this leads to a broader distribution of relaxation rates.

A puzzling feature is how subdued the zero field resonance is, since there are 4 times as many relaxation partners than when the degeneracy is lifted. Naively one would expect a proportional increase in relaxation rate (especially for the higher concentration spots where the dipolar relaxation contribution would be more significant). This can partly be explained by consider the fact that NV centers aligned along the same direction have a roughly 1.5× larger interaction energy than with those aligned along any of the other 3 axis, but this should still cause a 3x increase in the relaxation rate.

Another effect not accounted for in the experiment is the photo-ionization of the NV^- center to NV^0. The ratio between the number of NV^0 and NV^- centers is influenced by many factors amongst them the intensity and duty cycle of the laser radiation [90]. As the time between pulse τ is swept the equilibrium ratio between the two populations change possibly introducing systematic errors in the results.

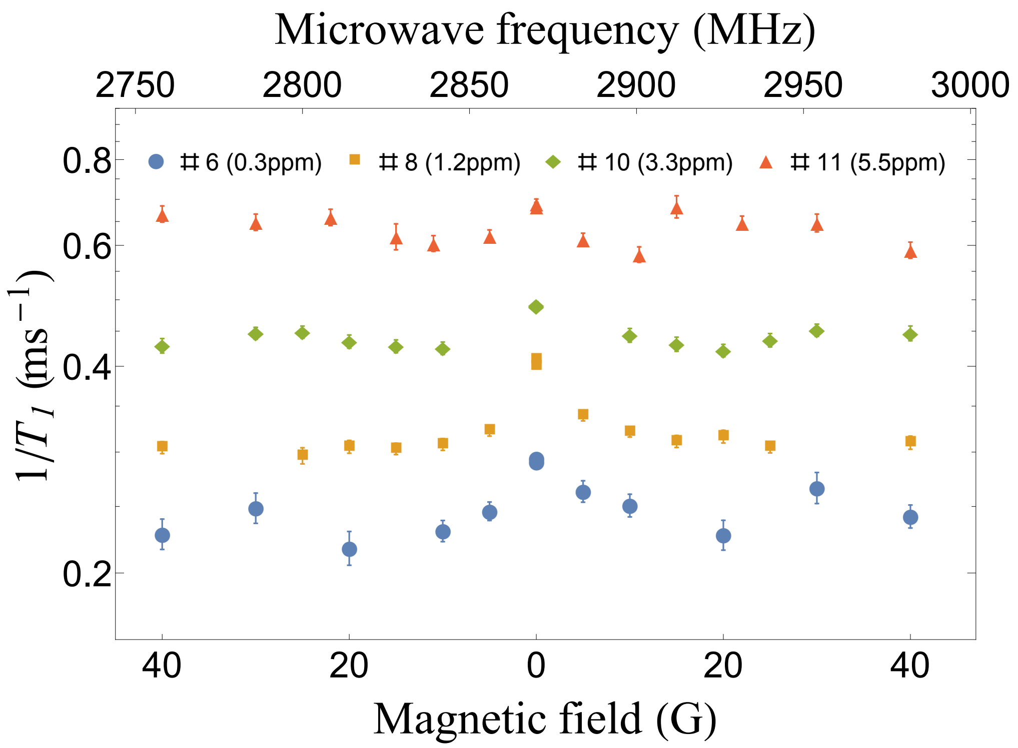

Figure 2.6: Magnetic field dependence of the effective relaxation rate $1/T_1$ for spots with different NV concentrations.

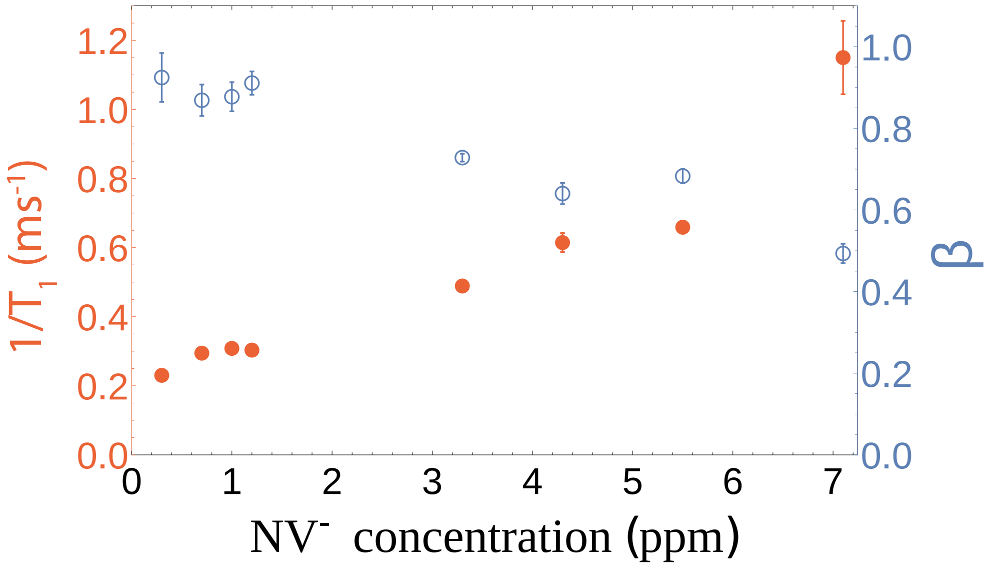

Figure 2.7: Fit parameters for population relaxation curves measured at different NV concentration at $B_0 = 30$ G. Error bars are estimated as upper and lower bounds in the parameter confidence intervals at a 95% confidence level.

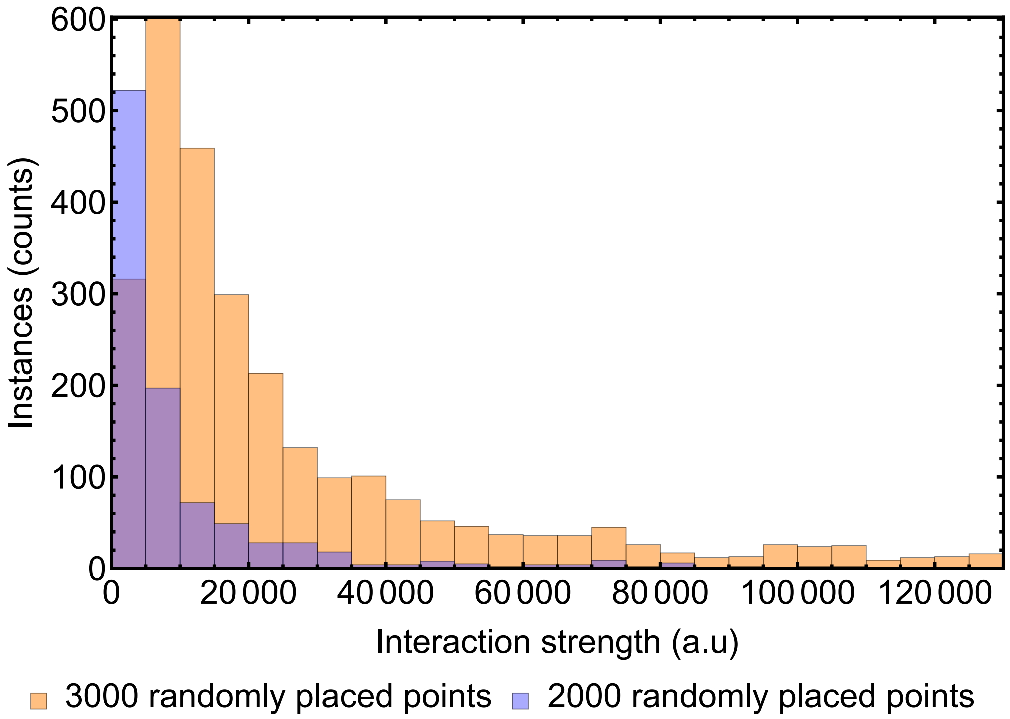

Figure 2.8: Monte-Carlo simulation for two different concentrations of randomly placed NV centers. The x-axis shows the interaction strength with the closest neighbouring NV center.

Chapter 3

Magnetic microscopy with NV centers

A wide array of magnetic phenomena manifest itself only at the microscale. The research fields interested in understanding micro- and nano-magnetic behaviour range from geology [91], study of superconductive materials [92], spintronics [93] and medicine/biology [10]. Commonly used bulk magnetometry cannot capture these small scale effects. Existing micro-scale techniques each have their own drawbacks: magnetic force microscopy while having AFM spatial resolution is limited in terms of field of view (typically $< 100\ \mu$m) and poor sensitivity ($> 10\ \mu$T). SQUID based microscopes suffer from poor spatial resolution ($\sim 150\ \mu$m [94] when working with room-temperature samples. Magneto-optical Kerr effect (MOKE) microscopes need Faraday-active samples or deposition of such a layer on top of the sample which might perturb the system in hard to predict ways and is generally incompatible with biological systems. The spatial resolution of a properly engineered ensemble diamond sensor is is limited only by diffraction. This enables microscale magnetic resonance imaging at room temperature with a reported volumetric DC magnetic field sensitivity of 34 nTμm$^{-3/2}$Hz$^{-1/2}$ with a theoretical sensitivity in the $\sim$ 100 pTμm$^{-3/2}$Hz$^{-1/2}$ pT range [17] while keeping the cost of the setup under $<$ 50k USD. To reach this kind of performance several technical challenges unique to the diamond platform must adequately addressed.

This chapter will discuss the basic working principles of a NV magnetic microscope, the best practices and technical challenges that need to be addressed to reach peak sensitivity, give an overview of recent groundbreaking work in the field, and discuss results from two specific imaging experiments studying chains of magnetic micro-particles and the magnetic properties of malarial hemozoin crystals.

Another intensively explored area of study in the field of NV quantum sensors are single NV scanning tip microscopy. This chapter will, however, omit any discussion on this subject focusing only on the microscopy detection modality.

3.1 Basic components and principles of operation of the diamond magnetic microscope

The basic building blocks of the NV magnetic microscope are similar to the ODMR magnetometer discussed in section 1.3.2 and a typical setup (shown in Fig. 3.1) bears many resemblances to the one shown in Fig. 1.4. The procedure is also similar

- The magnetic sample is placed on top of the diamond. For micro- and nanoscopic samples even small stand-off values can introduce significant variations in the field strength at the NV-site so the deposition protocols should be designed with care to ensure precision and reproducibility.

- NV centers are excited and spin-polarized by green light either in an epifluorescence configuration as shown in Fig. 3.1 or from the side as shown in the the review by Levine and Turner et. al [94].

- An external field is applied along a particular NV axis (out of 4 possible directions) to simplify the spectra. Other configurations where the field is placed the (100) direction of the diamond or indeed in a random direction that does not lie in any of the symmetry planes of the crystal are also sometimes used. The former yields a higher sensitivity while working at low fields while the latter is useful in a vector-magnetometer implementation. In NV ensemble magnetometers some bias magnetic field is almost always applied as there is always some transverse strain coupling the $|m_s = \pm 1\rangle$ resulting in a poor sensitivity near zero field.

- The applied microwave frequency is swept in synchronicity with the framerate of the camera. Usually this procedure is repeated many times to achieve the desirable per-pixel sensitivity. The result is a stack of fluorescence images at different applied microwave frequencies from which the spatial magnetic field distribution can be obtained.

There are however certain additional elements that are necessary to improve the performance of the microscope. In order to illuminate homogeneously a reasonable portion of the field-of-view usually a lens or a lens system is placed in the excitation beam path. The microwave field strength should also be uniform across the sample to avoid sensitivity losses due to power broadening (discussed in section 1.3.2). A commonly used and simple approach is using a circular microwave trace deposited on a microscope cover-slip or the diamond itself. This ensures optical accessibility with reasonable power delivery while still maintaining a low AC quality factor - a pro rather than a con since power delivery uniformity across a broad frequency range is more important than power delivery efficiency.

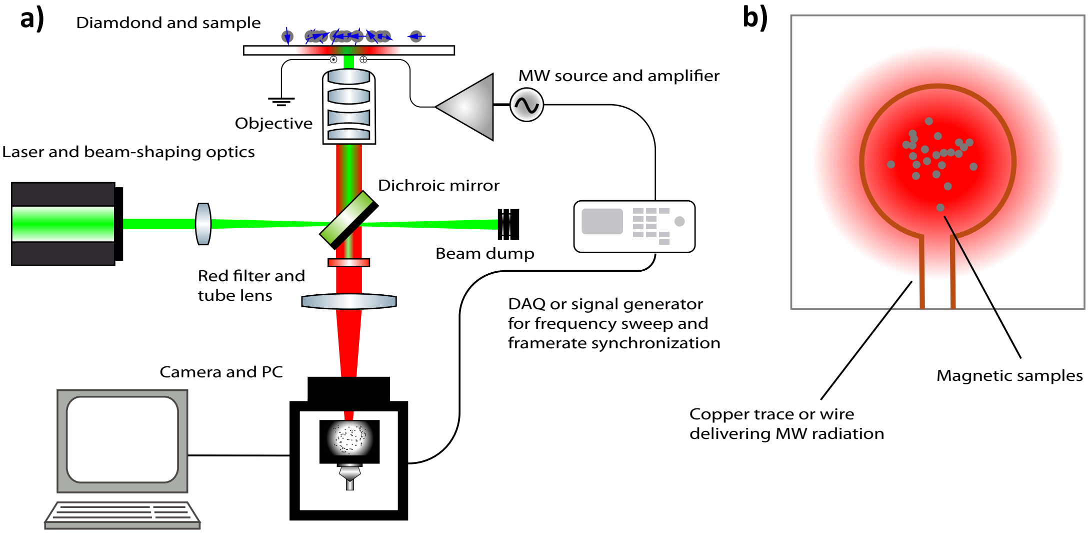

Figure 3.1: The magnetic resonance imaging setup. a) The schematic of an epifluorescence diamond microscope. The sample is usually placed on top off the diamond while the microscope is inverted. b) Top view of the diamond. The red area shows the illumination/fluorescence profile and the brown line is a deposited copper trace surrounding the field of view.

The magnetic field information extracted from the frequency-synchronized image stack can be understood by observing Fig. 3.2, which shows a simple model experiment where identical paramagnetic particles are placed on top of the diamond and the $|m_S = 0\rangle \rightarrow |m_s = -1\rangle$ ground state spin transition is addressed (this determines the sign of the resonance frequency shift). As the frequency is swept closer to resonance the fluorescence intensity decreases. This happens faster for the paramagnetic particles as the field is slightly stronger in their vicinity and initially these regions appear dimmer. As the sweep continues these regions will eventually appear lighter than the background as the resonance has already been crested for the regions in the vicinity of the particles while the particle-free regions are lagging behind. After the sweep is complete the local magnetic field value can be obtained by performing per pixel fitting of the ODMR spectrum.

The description above omits some details encountered in actual imaging experiments. Firstly only magnetic field projections along the NV axis contribute to the frequency shift. This can explained by looking at the NV Hamiltonian where the microwave radiation is again addressing one of the transitions (let us again assume we're working with the $|m_s 0\rangle \rightarrow |m_s = -1\rangle$ transition). This approach ignores

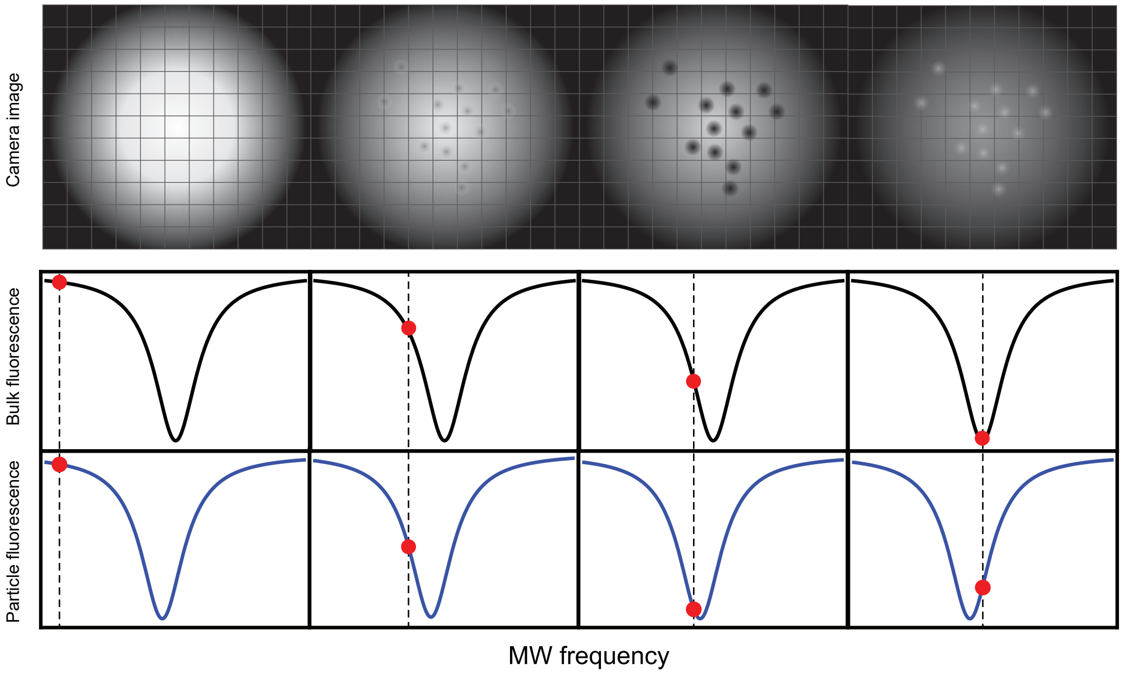

Figure 3.2: Magnetic image formation. Top row shows the image on the camera sensors corresponding to the detuning from resonance. Placed on top of the diamond are several paramagnetic particles. The bottom two rows show the fluorescence/MW frequency dependence for particle free regions (black) and regions in close vicinity to the particles (blue).

strain-related effects but we can assume that an applied bias field is strong enough to make them negligibly small. The system Hamiltonian can then be written as:

$$\hat{H} = \begin{pmatrix} 0 & \gamma\frac{1}{\sqrt{2}}\left(B_x + iB_y\right) \\ \gamma\frac{1}{\sqrt{2}}\left(B_x - iB_y\right) & D + \gamma(B_z + B_0), \end{pmatrix} \tag{3.1}$$

where $\gamma = 2.8\text{MHz/G}$ is the NV electron g-factor, $D \approx 2870$ MHz is the zero field splitting and B_x, B_y, B_z are the sample field components (the NV axis is assumed to be aligned along the z-axis) and B_0 is the bias field strength. Solving for the Eigenvalues of the Hamiltonian, the magnetic-field-dependent transition frequency ν is equal to

$$\nu = \sqrt{D^2 - 2D(B_z + B_0)\gamma + (2B_\perp^2 + (B_z + B_0)^2)\gamma^2}, \tag{3.2}$$

where $B_\perp^2 = B_y^2 + B_x^2$. By introducing a new term ν_0 and doing a series expansion:

$$\nu_0 = (D - B_0\gamma) \tag{3.3}$$

$$\nu(B_z) = \sqrt{\nu_0^2 + 2(B_\perp\gamma)^2} - \frac{\nu_0 B_z \gamma}{\sqrt{\nu_0^2 + 2(B_\perp\gamma)^2}} + \mathcal{O}(B_z^2) \tag{3.4}$$

$$\nu(B_\perp) = \sqrt{\nu_0^2 + (B_z\gamma)^2} + \frac{(B_\perp\gamma)^2}{\sqrt{\nu_0^2 + (B_z\gamma)^2}} + \mathcal{O}(B_\perp^3) \tag{3.5}$$

one can see that $B_\perp$ appears only as a second-order effect while there is linear scaling in B_z. This means that for certain applications where the sample magnetization is not aligned with the the applied bias field (for example a nuclear magnetic resonance experiment) the field measured by the NVs could be much smaller than the its actual magnitude.

Secondly the fluorescence contrast in Fig. 3.2 is greatly exaggerated. An imaging experiment is nothing more than a multiplexed ODMR spectroscopy experiment so the sensitivity has the same scaling (eq. 1.9) with the difference that the photon collection rate is distributed across many pixels on the camera sensor. This elevates the importance of light collection efficiency while simultaneously demanding excellent performance in terms of both chromatic and geometric aberrations. For this reason epi-fluorescent setups typically use infinity-corrected high-numerical-aperture (NA) oil immersion objectives as some apochromatic variants that use specialty oils can reach NA values of up to 1.6. However, since objectives with such high NA come with an incredible price-tag of over 10 thoursand USD, ~~for this reason~~ 100x/1.4 plan-N objectives are often used) with excellent aberration properties. The collection efficiency vs. NA dependence in an epi-fluorescent configuration is proportional to [95]:

$$\eta_{\text{light}} \propto \frac{\text{NA}^4}{M^2}. \tag{3.6}$$

The typical oil immersion values optical density values are matched to that of crown-glass ($n_{\text{glass}} \approx 1.5$) to maximize light transmission. Diamond has significantly higher optical density $n_{\text{diamond}} \approx 2.5$ and only benefits from a higher refractive-index medium on the objective side.

3.2 Technical challenges of NV microscopy

There are several technical challenges and implementation considerations that are unique to the NV diamond microscope. Some of these have already been mentioned—necessity for high illumination/microwave power homogeneity over the sensing area and high quality imaging optics—other aspects that warrant more attention are diamond engineering, image readout noise and efficiency, temperature/strain influence and excitation optics.

3.2.1 Diamond engineering

The engineering of the diamond sensor is arguably the most important aspect of the diamond microscope both because it directly influences the luminosity/contrast/resonance width, and because it governs the sample-sensor distance and magnetic resolution.

The typical z-axis resolution of a confocal microscope is $\sim 1\mu$m, however this is not necessarily a limiting factor as the control of the NV depth distribution can be much finer. The field from isolated magnetic particles as small as 19 nm has been captured by a sensing layer $\sim$ 100 nm thick NV sensing layer in diamond [41]. It is not trivial to find the optimum diamond parameters for a given sample as it is a function of multiple parameters: the spatial distribution and orientation with respect to the NV axis, the point-spread optical function of the setup, depth distribution of the NV centers and the resonance profile of the ensemble.

Every NV center can be considered a point-source with a microwave frequency/local magnetic field strength dependent fluorescence strength. In general the fluorescence intensity of this point source can be written as:

$$F(\nu, x, y, z) = F_0 \left[1 - C\mathcal{P} \left(\frac{\{\nu_0 - \mathbf{B}(x, y, z) \cdot \hat{\mathbf{e}}_{\mathbf{NV}} \gamma\} - \nu}{\Delta\nu} \right) \right], \tag{3.7}$$

where C is the contrast, $\mathcal{P}$ is the resonance profile (typically a Lorentzian or a Gaussian but can be more complicated if hyperfine interactions are resolved), $\Delta\nu$ is the resonance linewidth, ν_0 is the resonance frequency set by the bias field, $\hat{\mathbf{e}}_{\mathbf{NV}}$ is a unit vector pointing along the NV axis, ν is the applied microwave frequency and F_0 is the off-resonance fluorescence intensity. In the image each of these points are convolved with the point-spread function (PSF). Ignoring aberrations at the edges of the field-of-view the PSF in the xy plane is just the Airy disk which can be well approximated by a Gaussian with $\sigma = 0.42\lambda/NA$. In most cases the NV layer is smaller than the PSF in the z direction, so it can be assumed that the fluorescence of all vertical slices is just added together. The the image on the camera can be expressed as:

$$\begin{aligned} I(Mx, My) = \int\limits_{z_{min}}^{z_{max}} (F * PSF)\, dz = \\ = \frac{1}{2\pi\sigma^2} \int\limits_{z_{min}}^{z_{max}} \int\limits_{-\infty}^{+\infty} \int\limits_{-\infty}^{+\infty} F(\nu, u, v, z) \exp\left(-\frac{(x-u)^2 + (y-v)^2}{2\sigma^2} \right) dudvdz \end{aligned} \tag{3.8}$$

Ar a rule of thumb the optimum NV layer thickness should roughly match the typical feature size of the of the magnetic signal. To illustrate why it is helpful to set up a model system where a magnetic dipole point source (for example a paramagnetic nanoparticle) is placed on top of a NV layer of thickness d_{NV} (see Fig. 3.3 a). The surface normal of the vector is taken to be aligned along the [100] direction, this determines the applied magnetic field and magnetization directions. The chosen figure of merit for sensitvity is the fluorescence weighed signal strength—max $\left[\mathbf{B} \cdot \hat{\mathbf{e}}_{\mathbf{NV}} \sqrt{d_{NV}}\right]$—as shot noise is the dominant source of noise and for layers of thickness $s = d_{NV} < 1\mu$m has $1/\sqrt{d_{NV}}$ scaling with the layer depth.

The depth dependence s on the layer depth for two particles of different diameters is shown in Fig. 3.3 There are two conclusions that can be drawn from the model system:

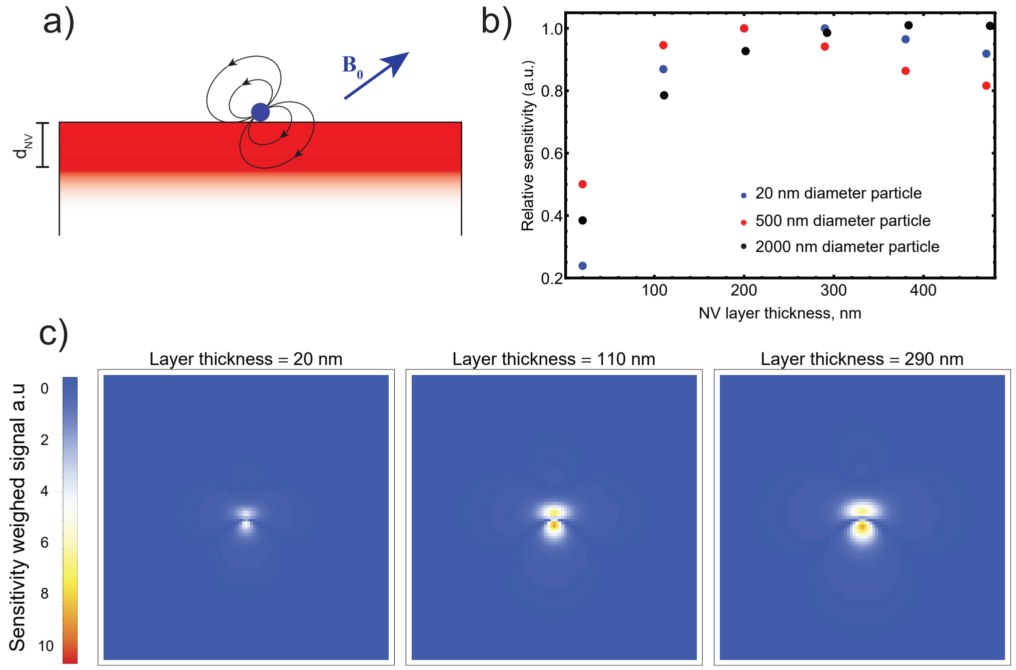

Figure 3.3: Layer depth versus signal strength. a) The model system with a paramagnetic particle on top of a NV layer. b) Signal strength s (defined in the main text) as a function of NV layer depth for three different paramagnetic particles c) Spatial distribution of the s strength for a 500 nm diameter superparamagnetic particle.)

- The signal strength has a rather gentle degradation with increasing layer thickness so the main consideration should be the degradation of spatial resolution due to the broadening of the magnetic features

- Even if the particle is very small, the diffraction limit on the resolution means that it is never worth decreasing the layer thickness beyond $\sim$ 200 nm (given by the diffraction limit. $d = \frac{\lambda_{NV}}{2NA} \approx 250$ nm.

Once the decision on the optimum layer thickness has been made, the decision on what is the best materials engineering approach to achieve the desired distribution must be answered. The simplest approach is taking a type IIa diamond with very low nitrogen concentration and implanting nitrogen ions at an appropriate energy (or multiple energies) usually estimated from SRIM [36] simulations. This process both creates vacancies and and introduces the nitrogen in the lattice. As the diffusion activation energy for substitutional nitrogen defects is much larger than for vacancies [96] the NV distribution after annealing will mimic that of the nitrogen distribution after implantation. The main drawback of this approach is the introduction of multi-vacancy defects and other forms of lattice damage that negatively impact the sensor performance. To avoid this lighter implantation species usually provide better results and Helium or electrons are often used (due to the relatively high electron affinity hydrogen is not a good implantation candidate). This means that the substitutional nitrogen defects should already be present in the diamond from the growth process. Commercially easily available and cheap type Ib diamonds have a nitrogen content anywhere between 10s to 100s of ppm distributed uniformly through the entire volume. In this case the NV distribution roughly follows the vacancy distribution, however, during the annealing step the vacancies are free to diffuse and based on the annealing temperature and duration. As a conservative example if the diffusion activation energy is taken to be ~ 1.7eV a 3 hour anneal at 800°C nets a root-mean-square vacancy translation distance of ~ 200nm. A saving grace is that once the vacancy has been captured by a substitutional nitrogen both the diffusion energy and disassociation energy of the compound defect are large and happen at temperature greater than 1600°C [97], [98]. As a ball park estimate for type 1b diamonds the typical diffusion induced broadening distance is only ~ 40 nm.

3.2.2 Temperature

For higher density NV centers the optical powers needed to drive them optimally can be substantial. While diamond is one of the best thermal conductors in the world thermal gradients follow the laser power distribution can still be observed. This effect was briefly discussed in section 1.5.1. The way to suppress this is to address both of $|m_s = 0\rangle \rightarrow |m_s = \pm 1\rangle$ transitions and subtract the ODMR profiles. As the magnetic field shifts the resonance frequencies in opposite directions while temperature shifts them the same way the temperature dependence is canceled out:

$$\begin{aligned} f_+ &= D(T) + \gamma(B_0 + B_s) \\ f_- &= D(T) - \gamma(B_0 + B_s) \\ B_s &= \frac{f_+ - f_-}{2\gamma} - B_0, \end{aligned} \tag{3.9}$$

where $D(T)$ is the temperature dependent zero-field splitting, B_0 is the bias field and B_s is the sample field projection along the NV axis. The simplest way of implementing this is alternating between transitions after each sweep around a particular resonance and subtracting them after both the scans are done (Fig. 3.4). The advantages of this approach is the possibility of operating the two MW channels

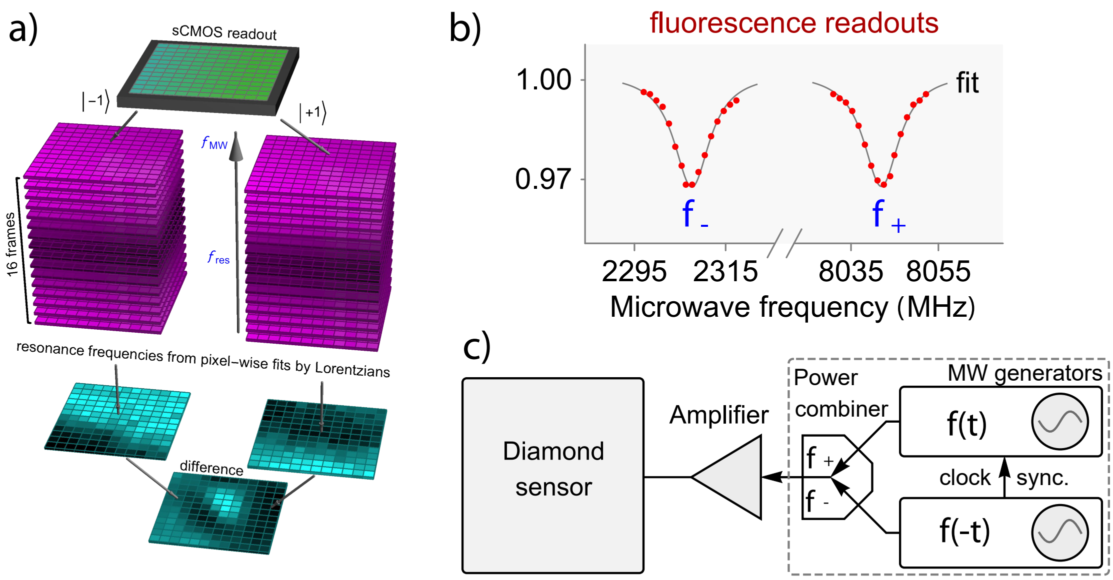

Figure 3.4: Approaches to suppressing temperature effects. a) Two stacks of frames, each corresponding to a full sweep of the resonance, are recorded, per-pixel resonance frequency is extract from nonlinear fitting, finally the two frequency maps are subtracted to yield the true magnetic field distribution. b) Transition frequencies for a 1848G large bias field. Red dots represent frame triggers. c) A dual resonance approach (figure from [99]). The two MW frequencies are combined into a single channel before being amplified. If the frequencies are swept in opposite directions this effectively constitutes a subtraction of the two transitions.

without sharing any hardware as it is often difficult/expensive two ensure high power, high efficiency and low noise spanning multiple GHz. The disadvantage is increased duty cycle and lower temperature suppression as any fluctuations faster than the time to acquire scans at both frequencies will not be cancelled out. Another approach is shown in Fig. 3.4(c). Both frequencies are combined together through a power combiner and amplified. If the frequencies are swept in opposite direction transition frequency dependencies common for both ±1 transitions (temperature, strain, electric field) will be suppressed. If, however, frequencies are swept in the same direction the device can operate as a microscale temperature/electric field sensor. However, this implementation might be challenging if high bias fields are necessary as the power combiner and amplifier would need to operate over a very broad frequency range.

3.3 Standout achievements in NV magnetic imaging

The first demonstration of a widefield NV based DC magnetic microscope operating in CW regime was done by Steinert et. al [100]. While work before this had already demonstrated the imaging capabilities of NV centers in a scanning tip experiment, this work demonstrated multiplexed magnetic field (generated by two parallel gold micro-wires on the diamonds surface) readout from a manufactured (by $^{15}N^{+}$ implantation) 2D array of NV centers. Shortly afterwards Pham et. al [101] demonstrated widefield imaging of DC and AC magnetic fields by coherently manipulating the ensemble spins. For DC sensing a Ramsey sequence was used (see section 1.4.3) and for AC sensing a Hahn-echo sequence was used (see section 1.4.2). The outlook of both of these papers emphasized how suitable the platform was for studying biological systems. The sensor is hosted in diamond—a biocompatible material—operates at ambient conditions and has the sensitivity and resolving power to probe samples at the single cell level.

In 2013 a paper published by Le Sage et al. [9] optical resolution magnetic imaging of a living system was demonstrated. The specimen that were analyzed was a magnetotactic bacterium: a single-celled organism that naturally grow membrane-bound organelles containing chains of ferromagnetic nanoparticles. The authors were able to perform magnetic field measurements of cells in a liquid solution while retaining high cell-viability. In order to avoid cell death due to the high excitation powers used, they coupled the excitation beam through a glass cube at a an angle steeper than the total internal reflection (TIR) angle. This meant that light was only evanescently coupled into sample space significantly decreasing cell death from photo-toxicity.

A similar setup also using TIR excitation was used in a paper by Glenn and Lee et. al [10] to demonstrate microscale sensing of magnetically labelled tumor cells (see Fig. 3.5). The authors report a 100% detection rate in a wide field of view (1 mm^2) with optical resolution. Situations where magnetic labels outperform fluorescent dyes are long-timescale experiments where autofluorescence or photobleaching cause image degradation, or if working in a medium that effectively scatters or absorbs light.

The diamond magnetic microscope has been successfully applied to fields other than biology as well. The broad working temperature range of the NV center magnetometer makes it appealing in studies of high temperature superconductors [102]. However, this application is complicated by the heat deposited in the diamond sensor by the excitation beam, which limits the sensor-sample distance and adversely

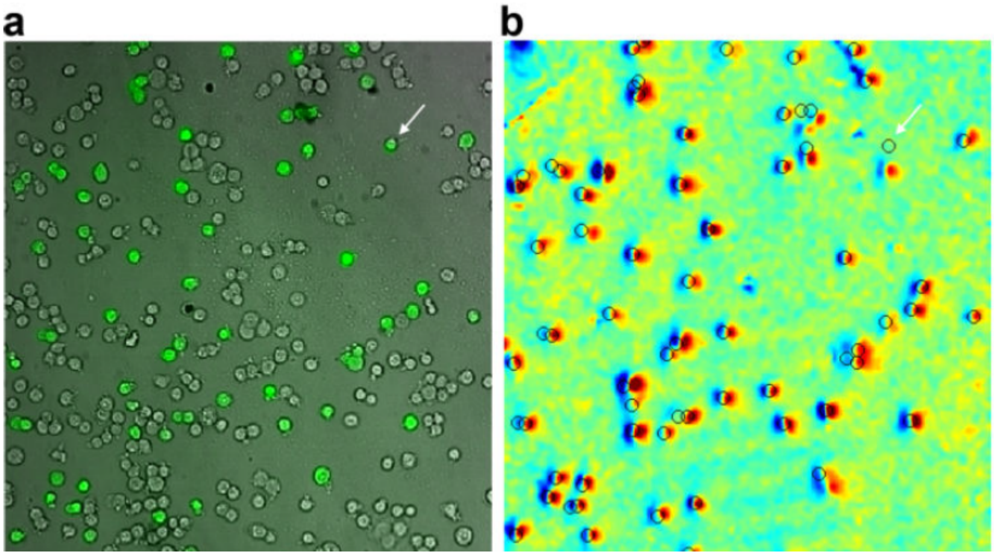

Figure 3.5: Magnetically labeled tumor cells from the paper by Glenn and Lee et al. [10]. a) Shows the optical image of two subsamples of cells where tumor cells are magnetically and fluorescently (for an illustrative overlay) labelled while b) shows the corresponding magnetic image. The detection rate is 100%. During the experiment it was also observed that once cell moved, a white arrow indicated the cell.

affects both spatial resolution and sensitivity. A study by Glenn et. al [91] studied geological samples with high field-of-view (up to 4x4 mm^2) and 5 μm resolution. The authors cite spherical aberrations and sample roughness as the main limiting factors of the spatial resolution. The former is caused by the necessity of imaging through the diamond, which causes spherical aberrations, and could be improved by designing thinner diamond chips. The latter would be improved by preparing thinner rock sections.

The NV magnetic microscope is a rapidly maturing technology and with further improvements in performance new avenues of research could be pursued. A noteworthy example is nuclear magnetic resonance imaging. The diamond sensor could be used both as a sensor (through magnetic imaging) and a signal booster (through spin polarization transfer) enabling mapping an additional detection modality: nanoscale chemical composition imaging. But at this point in time the sensitivity of the device is still insufficient to achieve adequate signal-to-noise ratio.

3.4 Magnetic imaging of particles

The potency of the platform motivated the University of Latvia Laser Center in collaboration with the Laboratory of Magnetic Soft Materials to build a magnetic imaging microscope with the ultimate goal of studying the dynamics of magnetic microswimmers, more specifically, a microswimmer consisting of a chain of ferromagnetic and superparamagnetic particles connected by a strand of protein. Controllable micro-scale devices have the potential to significantly improve precision medicine through techniques such as targeted drug delivery and the magnetic variety addresses one of the key challenges in the field—sustained locomotion—by driving them via an external magnetic field that can penetrate tissue. However, the interactions between the different forces at play (fluid viscosity, elasticity of the swimmer, magnetic dynamics within the beads, etc.) are complicated and hard to decouple, a time-dependent magnetic field map could help shed light of the magnetic dynamics of microswimmers. The first step was obtaining the static magnetic field distribution of the particles forming the swimmers.

3.4.1 Experimental implementation

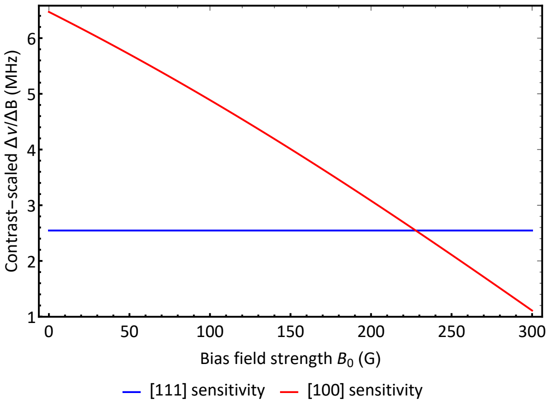

Figure 3.6: Sensitivity vs bias field for two different alignments.

The mangetic microscope design was based the epi-fluorescence configuration described in section 3.1 with the exception that the magnetic field was aligned along the [100] direction of the diamond (see Fig. 3.7[a]). While working at small bias fields < 200G this configuration yields a net improvement in sensitivity of $\sim 2\times$ due to the 4-fold increase in contrast from addressing all the spatial NV subgroups. The CW-ODMR sensitivity possesses linear scaling with contrast; the reason the relative gains are smaller are two-fold. The first is shown in Fig. 3.6 where the contrast-scaled frequency-field dependence $\partial\nu/\partial B$ is shown. For larger bias fields the field component transverse to the NV axis for the different becomes substantial and mixes the magnetic sublevels. In the aligned case (field along [111]) no state mixing occurs and the transition frequency/magnetic field dependence remains essentially constant (non-linear behaviour due to level-crossing/strain effects is ignored in this case). The second reason can be gleamed from Fig. 3.7(a). Each individual NV center subgroup still only possesses second order scaling of the transition frequency as a function of off-axis fields and are effectively sensitive only to the magnetic field projection along their respective axis. On the other hand - as all four spatial subgroups are addressed simultaneously - only the sample field projection along the bias field can be detected. Any field component transverse to the [100] direction will cause a pair-wise symmetric shift of the transition frequencies of the individual spatial subgroups with the "center-of-mass" remaining stationary. The net-result of this effect is that the field sensitivity is scaled by a geometric factor of $1/\sqrt{3}$.

This factor can also be derived mathematically in the following way. If the z axis is aligned along the [100] direction the unit vectors of each for possible NV direction can be written as:

$$\begin{aligned} \mathbf{e_{1,2}} &= \left(\mp\sqrt{\frac{2}{3}}, 0, \frac{1}{\sqrt{3}}\right) \\ \mathbf{e_{3,4}} &= \left(0, \pm\sqrt{\frac{2}{3}}, \frac{1}{\sqrt{3}}\right) \end{aligned} \tag{3.10}$$

The normalized observed fluorescence as a function of the applied MW frequency is the sum of the four spatial subgroups

$$F(\nu) = \frac{1}{4}\sum_{i=1}^{i=4} \mathcal{F}(\nu_0 + \mathbf{B}\cdot\mathbf{e_i}\gamma - \nu), \tag{3.11}$$

where ν_0 is the transition frequency due to the bias field and $\mathcal{F}$ is a funciton describing the resonance lineshape (typically a Gaussian or a Lorentzian). If the sample fields are much smaller than the bias field, the following simplification can be made:

$$F(\nu) = \mathcal{F}\left(\nu_0 + \sum_{i=1}^{i=4}(\mathbf{B}\cdot\mathbf{e_i}\gamma) - \nu\right). \tag{3.12}$$

Now substituting the unit vectors from equation 3.10 and gathering up the terms that do not cancel out yields:

$$F(\nu) = \mathcal{F}\left(\nu_0 + 1/\sqrt{3}B_z\gamma - \nu\right). \tag{3.13}$$

The diamond sensor was manufactured from a (100) face CVD type IIa diamond with a negligible nitrogen content. The chip was implanted with $^{14}N^{+}$ ions with 3 different energies—10 keV, 35 keV and 60 keV—creating a vacancy/nitrogen depth distribution shown in Fig. 3.7 (b). Subsequent annealing at 800°C should not have caused any further broadening of the final NV depth distribution as the diffusion activation energy of substitutional nitrogen is large.

Three types of magnetic particles were used: 4- and 2- μm diameter CrO_2 ferromagnetic core-shell particles and 500-nm-diameter Fe_2O_3 superparamagnetic particles. The latter consist of a polystyrene shell that encases an emulsified ensemble of Fe_2O_3 particles with a mean diameter of $\sim$ 10nm. This means that the particles can still remain superparamagnetic rather than ferromagnetic yet have a higher magnetic moment. The ensemble properties were characterized by vibrating sample magnetometry (VSM) shown in Fig. 3.8. The mass magnetization M

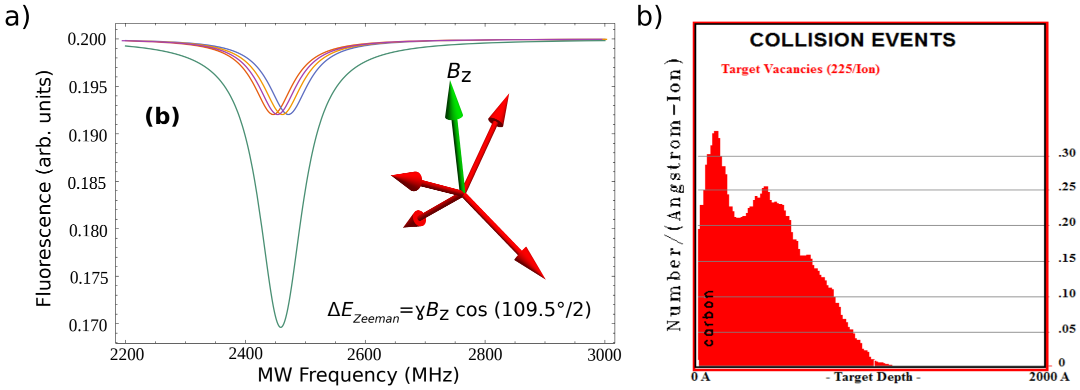

Figure 3.7: Bias field alignment and implantation paramemters. a) ODMR spectra simulation of the $|m_s 0\rangle \rightarrow |m_s = -1\rangle$ transition with a bias field aligned along the [100] direction. The signal is the sum of the contributions of all 4 spatial subgroups. A small off-axis field component is also added to prevent total overlap of the individual transition spectra and improve the legibility of the figure. b) A SRIM [36] simulation of the ^{14}N ion implantation parameters. The graph depicts the per-ion normalized vacancy distribution as a function of depth.

hysteresis curves for the ferromagnetic particles were used to estimate the magnetic moments of the individual particles from the density estimate given by the manufacturer ($\rho = 1.81$ g/cm^3). The magnetic moments are then given simply by $m = M\rho\pi\frac{d^3}{6}$. The magnetic moments of the paramagnetic particles were extracted directly from the magnetization curve (Fig. 3.8(c)) by fitting it with a Langevine function L:

$$\begin{aligned} L(\alpha) &= \coth(\alpha) - \frac{1}{\alpha} \\ \alpha &= \frac{mH}{k_B T}, \end{aligned} \tag{3.14}$$

where m is the magnetic moment, H, magnetic field, k_B, Boltzmann constant, and T, the temperature. The fit is shown in Fig. 3.8(d) and nets a magnetization estimate of $m \approx 1.6 \cdot 10^{-15}$Am^2. The purchased particles had been functionalized already with streptavedin a protein that forms a very strong non-covalent bond with another protein, biotin. By introducing biotin-terminated DNA fragments into an emulsion of the paramagnetic particles they will bind any pair of particles that come within a distance closer than the length of the DNA strand. By applying an external magnetic field the particles will also arrange themselves in strands that can then be bound by the biotin-terminated DNA strands.

After the chains are formed a 10 μL droplet containing the magnetic particle chains was drop-cast on the diamond surface and allowed to dry in a homogeneous external magnetic field aligned parallel to the diamond axis. The purpose of the magnetic field is to keep the chains stretched out and avoid clumping/knotting as

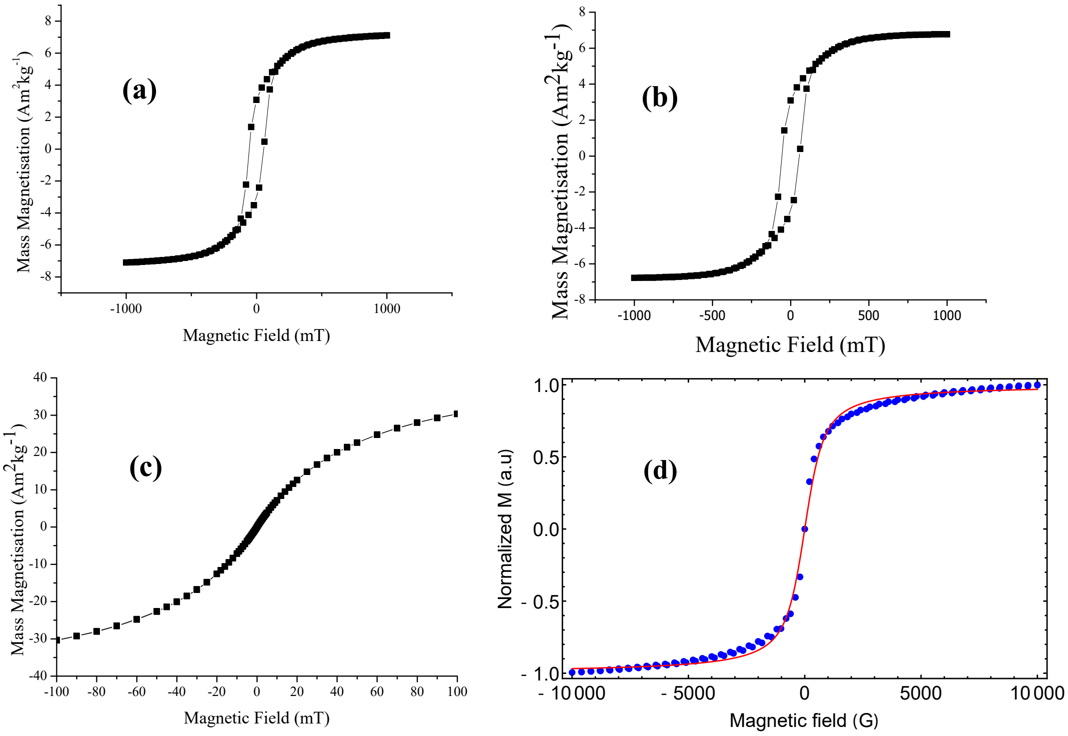

Figure 3.8: Vibrating sample magnetometry results for $4-\mu$m (a) and $2-\mu$m (b) diameter ferromagnetic particles and 500-nm-diameter (c) superparamagnetic particles. Figure (d) shows the Langevine function fit for normalized data from figure (c).

the liquid evaporates.

The microwaves were delivered through a 100 μm diameter copper wire from a microwave generator (Stanford Research Systems SG386) through a 45dB amplifier (Minicircuits ZHL-16W-43-S+). After the amplification stage the MW power was 3 W. The microwave frequency sweep and camera frame acquisition was synchronized in software. Each frame was additionally normalized to the fluorescence with microwaves off: $I = I_{on}/I_{off}$. This step was repeated 10 times and the result averaged together for each frequency. The MW sweep spanned 6 MHz.

3.4.2 Results

The magnetic optical and magnetic images of the three different particles both assembled as chains or not treated are shown side-by-side in Fig. 3.9. While the most straightforward way of distilling per-pixel ODMR spectra into magnetic field data is non-linear fitting for large images it is quite computationally taxing. In this work we made the trade-off of small deterioration in precision to an order-of-magnitude increase in processing speeds by using the following procedure:

1. the ODMR spectra for each pixel were normalized and inverted such that $\int_{f_{low}}^{f_{high}} \mathcal{F}(f)df = 1$ and $\mathcal{F}(f_{low}) = \mathcal{F}(f_{high}) = 0$, where f_{low} is the first frequency in the sweep, f_{high} is the last one and $\mathcal{F}(f)$ is the normalized function describing the resonance profile.

2. a cumulative function $\mathfrak{F}(f_0) = \int_{f_{low}}^{f_0} \mathcal{F}(f)df$ is obtained and interpolated.

3. the resonance frequency for each pixel is determined by solving for $\mathfrak{F}(f_{res}) = 0.5$.

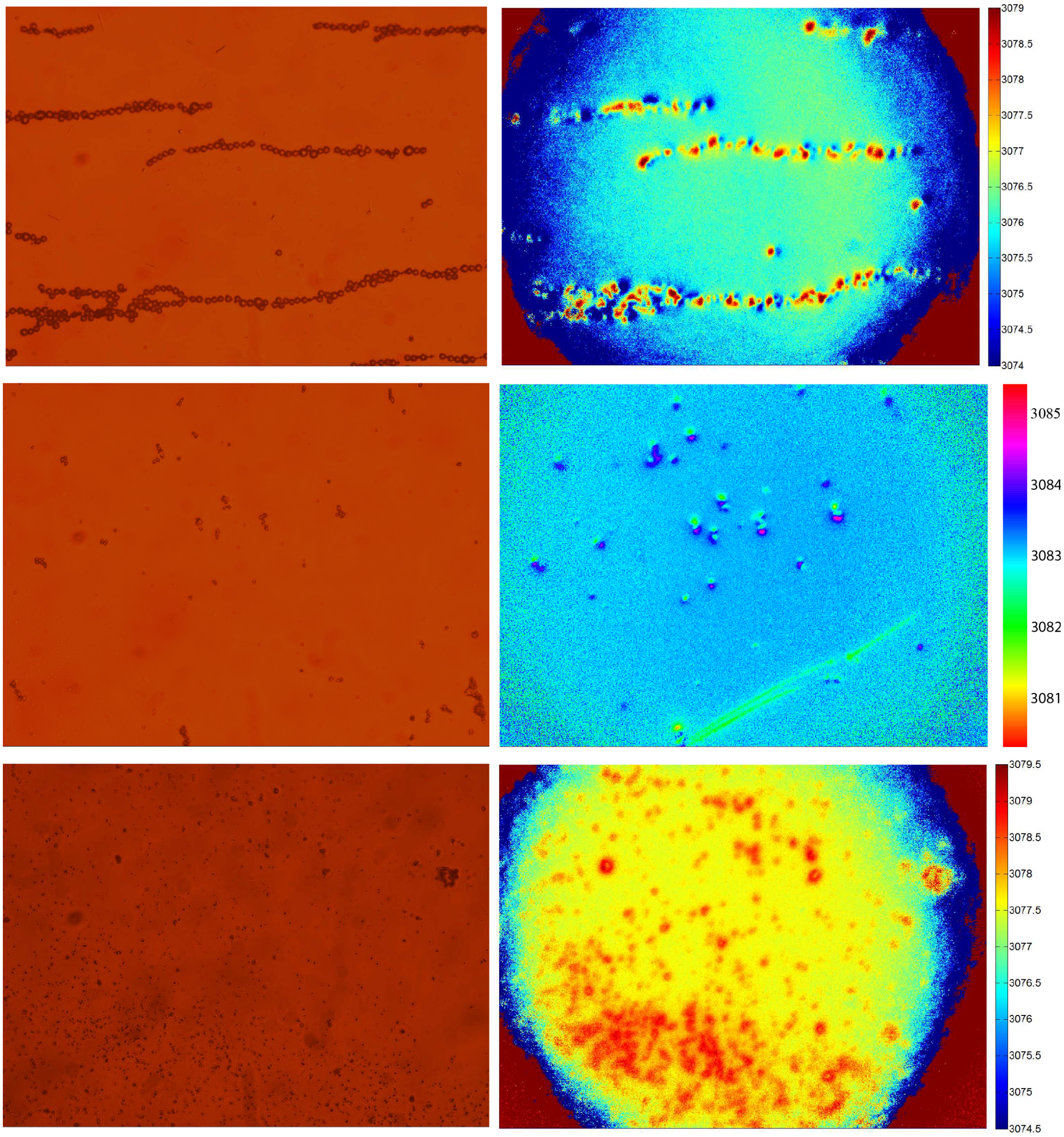

Figure 3.9: Optical and magnetic images of 4 μm, 2 μm ferromagnetic and 500 nm superparamagnetic particles.

The correlation between optical images and magnetic is very strong, but there is new information that can be gleamed from the magnetic images. First, in the images of ferromagnetic particle chains it can be seen that the individual dipoles are not very well aligned. The spatial distribution of the magnetic moment forming the magnetic chains directly influence the performance of the micro-swimmer and a direct image of this distribution allows for much faster iteration of the preparation protocol.

Second, the magnetic images also contain artifacts not related to the magnetic signals themselves. An example can be seen in the image of the 2 μm particles where an elongated feature is visible near the bottom of the image with no object present in the optical image. This is most probably a large scale plastic deformation within the diamond itself that cause frequency shifts due to higher local strain. An article documenting the common types of non-magnetic features observable in diamond magnetometry was recently published by Kehayias et. al [103].

Finally the individual magnetic momenta of each optically resolved particle can also be extracted from the images. Each particle generates a magnetic field that very closely follows that of a magnetic dipole:

$$\mathbf{B} = \frac{\mu_0}{4\pi}\left(\frac{3\mathbf{r}(\mathbf{m}\cdot\mathbf{r})}{r^5} - \frac{\mathbf{m}}{r^3}\right), \tag{3.15}$$

where μ_0 is the vacuum permeability, $\mathbf{m}$ is the magnetic moment and $\mathbf{r}$ is the sensor-particle distance. A complication that immediately arises for 500 nm particles is the optical resolution limitations already discussed in section 3.2.1. To combat this difficulty Richardson-Lucy deconvolution was performed for the fluorescence images at each microwave frequency before further analysis. The FWHM of the Gaussian PSF is $\sim$ 313 nm and was assumed to be constant across the field-of-view. After the deconvolution step a constrained non-linear fitting procedure was set up for isolated magnetic particles with the fit function:

$$\mathbf{e_{[100]}}\cdot\mathbf{B} = \frac{\mu_0}{4\pi}\left(\frac{3\mathbf{e_{[100]}}\cdot\mathbf{r}(\mathbf{m}\cdot\mathbf{r})}{r^5} - \frac{\mathbf{e_{[100]}}\cdot\mathbf{m}}{r^3}\right), \tag{3.16}$$

and free parameters $x, y, z-d/2$ for the location of the particle (d is the diameter of the particle) and m_x, m_y, m_z for the orientation and magnitude of its magnetic moment. Since only the magnetic field projection on the [100] axis is observable the unit vector along this direction is introduced in the above equation as well. Fit results for 2 μm and 4 μm particles are shown in Fig. 3.10 , and the magnetically relevant fit parameters are reported in table 3.1.

The obtained fit parameters exhibit several surprising features. First of all, the value of $z-d/2$ which characterizes the sensor-source distance is significantly larger (especially for the superparamagnetic particle) than the expected value of $\sim$ 0 nm where the particle is resting directly on the surface of the diamond. This stand-off distance is not just a mistake due to the numerical procedures employed as the

Particle type	ferromagnetic	ferromagnetic	superparamagnetic
diameter d (μm)	4 μm	2 μm	500 nm
Expected $\lvert\mathbf{m}\rvert$ (Am^2)	2.3×10^{-13}	2.6×10^{-14}	1.6×10^{-15}
Fitted z-d/2 (μm)	1.4 ± 0.1	1.3 ± 0.1	3.6 ± 0.1
Fitted $\lvert\mathbf{m}\rvert$ (Am^2)	$(6.0 \pm 0.1) \times 10^{-14}$	$(7.9 \pm 0.2) \times 10^{-15}$	$(1.2 \pm 0.1) \times 10^{-14}$

Table 3.1: Magnetically relevant fit parameters for the different magnetic particles investigated in this work.

observed magnetic features are also broader than suggested by a simple forward model according to expression 3.15. A possible culprit could be residual solute from the sodium azide and phosphate pH buffer solution in which the particles were suspended. Based on the solute concentration given by the vendor (correcting for a 50x dilution with water—a part of the preparation process), the deposited volume of 10μL would create a 1.2 μm thick layer of solid residue across the diamond which is close to the fit values obtained for the ferromagnetic particles. For the 500 nm superparamagnetic particles the discrepancy is even more pronounced however exact solution composition for the superparamagnetic particles is unknown precluding a similar analysis.

The magnetic moment values obtained from the fit also significantly deviate from the ensemble measurements both over- and under-shooting the expected values from ensemble measurements 4-10 times. While some variation in the magnetic moment values is expected the results obtained lie well outside the specification given by the manufacturer. These discrepancies indicative of uncontrolled-for systematics in the experimental setup discussed in the next section.

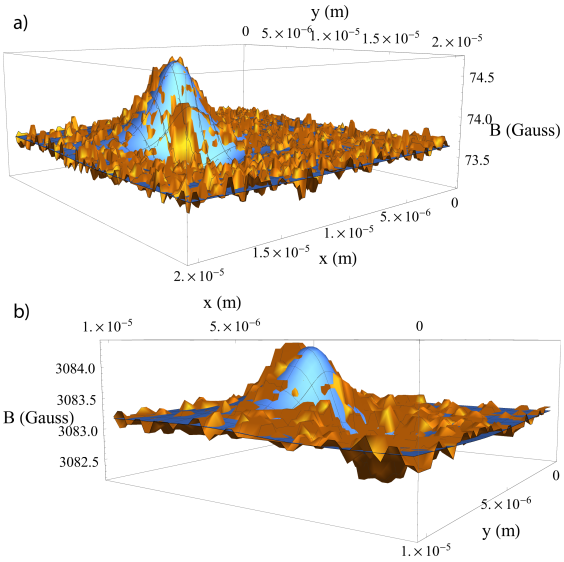

Figure 3.10: Data (orange) and fit result (blue) for an isolated 4 μm (a) and 2 μm (b) particles.

3.4.3 Design mistakes

The research reported on in the previous section were performed on a pilot-device in the University of Latvia and, as such, it suffered from several poor experimental design choices. While netting a reasonable qualitative description of the magnetic properties of the samples the quantitative disagreement prompted a further investigation of what should have been done differently. Three key areas of improvement were identified:

- Excitation intensity
- Phase-continuous frequency sweeps
- Image data normalization and microphonics

The green laser used in the experiment was a CrystaLaser GC532-100-SLM diode pumped solid state laser with a peak output power of 100 mW. The power at the input of the microscope objective was 60 mW. The power was spread across almost all the field of view which was 0.5 mm for our optical system (40x microscope objective with a 200 mm tube lens). The overall power density was thus only $\sim$ 250 $\mathrm{mW\,cm^{-2}}$ which falls below the optimum optical power density for our diamond sample [103]. This resulted in a poor signal to noise ratio, longer averaging times and possibly systematic errors due to long-term drift in temperature/optical alignment. A higher laser power would have also allowed us to increase the depth of the NV center layer increasing the fluorescence intensity and further improving SNR.

Another experimental inefficiency is related to how the MW frequency/frame synchronization was performed. Both the frequency stepping and frame acquisition was triggered in software by sending the appropriate command to the microwave generator (Stanford Research Systems SG386) and the camera (Leica DFC310 FX). This meant that before each frame the generator would have to re-acquire a lock on the set frequency. Per the specification of the generator at least 8ms are necessary to achieve a lock of 1 ppm. The exposure time per frame was $\sim$ 40 ms causing a broadening in the observed linewidth. Additionally serial communication is slow and the repeated back-and-forth between the hardware and control software add several milliseconds of down-time for each frequency, negatively impacting the measurement duty cycle. An alternative synchronization scheme implemented in to latest iteration of the microscope uses frequency modulation of the microwave signal (the same generator is capable of a modulation depth of 32 MHz in the 2-4 GHz range) with an analogue voltage and hardware trigger the frame acquisition. Both the modulation input an frame trigger pulse trains are controlled by the same DAQ ensuring long term stability.

Both of the flaws mentioned above affect the signal-to-noise ratio but do not directly lead to biased results. We believe this effect arises from the self-referencing procedure where the fluorescence was normalized against the fluorescence intensity when the microwaves for turned off: $I = I_{on}/I_{off}$. This was done with the intention of suppressing any drifts in the optical setup and low frequency vibrations, and, at first, an increase in the magnetic image contrast was observed. However, it was later observed that the magnetic particles were also visible when the MW radiation was far off-resonance the transition frequency of the NV center leading to the conclusion that what was actually observed was a microphonics induced artifact. This effect could account for the large size of the magnetic features and lower average magnetic field strength. A better referencing strategy is addressing both the $|m_s = 0\rangle \rightarrow |m_s = +1\rangle$ and $|m_s = 0\rangle \rightarrow |m_s = -1\rangle$ transitions and subtracting the observed signals. Details of this procedure are described in section 3.2.2.

3.5 Magnetic imaging of malarial hemozoin

The power of optimized experimental procedures was demonstrated in a later work probing the properties of hemozoin [104]. Hemozoin is an organic crystal formed by blood-feeding parasites. Amongst such parasites is *Plasmodium* that causes malaria. A product of the parasites digestion of haemoglobin is heme, a substance toxic to cells and to the parasite itself. The parasite accretes free heme into insoluble hemozoin crystals to avoid poisoning itself. Anti-malarial drugs disrupt the the formation of hemozoin and cause the parasites to kill themselves. The NV diamond microscope could theoretically probe the hemozoin formation/disruption dynamics in living *Plasmodium*-infected cells. However, the first step is to produce magnetic images of individual hemozoin crystals. The author's contribution to this work was limited to implementing the control and automation software and discussing the results.

3.5.1 Experimental modifications and results

When compared to the experimental implementation of the NV magnetic microscope described in section 3.4.1 several key aspects are different. First, the experiment was realized at a much higher magnetic field as the sample is paramagnetic and the produced signal has linear scaling with applied field strength. Two permanent neodymium magnets were used to apply the bias field as shown in Fig. 3.11. This provided both the high magnetic field strength and reduced the magnetic field inhomogeneity. A (110) surface cut 0.2µm thick type Ib diamond (roughly 50 ppm of nitrogen) was used, and the magnetic field was aligned along one of the four possible NV axes. Second, 200 mW of 532 nm excitation power (Lighthouse Photonics Sprout-G-10W) were used to excite a 40 × 40µm spot in the diamond through an oil-immersion objective ensuring adequate optical power to optimally excite the NV centers. Third, both of the NV transitions were addressed in an alternating manner where the addressed transition was changed every full sweep (one sweep consisted of 16 frames each with an exposure time of 3 ms). All MW/camera synchronization was done in hardware with the sole exception of switching the central MW frequency, which was done in software. Finally, the sensing properties of the NV centers were themselves improved both because the (110) surface cut enabled better alignment between the NV electric transition dipole moment and the electric field vector of the exciting light and, more importantly, because lighter ions could be used to create vacancies as the type Ib diamond already has ∼ 50 ppm of substitional nitrogen. This resulted in lower lattice damage and thus better NV coherence/sensing properties.

The compound effect of all of these steps was a per-pixel sensitivity of $8.4\,\mu\mathrm{T\,Hz^{-1/2}}$ which is an order of magnitude improvement on the implementation discussed in section 3.4, where a sensitivity of $\sim 100\mu\mathrm{T\,Hz^{-1/2}}$ was observed. This enabled the multiplexed study of the properties of individual hemozoin crystals revealing features missing from the ensemble results. The merits of characterizing a population of single crystals versus an ensemble measurement was immediately demonstrated upon closer examination of the magnetic properties. Around 95% of hemozoin crystals were paramagnetic with a volume magnetic susceptibility $\xi = 3.5 \times 10^{-4}$ and in agreement with results reported in other sources [105], [106], however, a small fraction of the particles showed saturation magnetization saturation at high applied magnetic fields (see Fig. 3.12a) B_0 while simultaneously generating much stronger sample fields the other crystals (see Fig. 3.12b). This behaviour is indicative of superparamagnetism, a result reported on in artificial hemozoin crystals [107], [108].

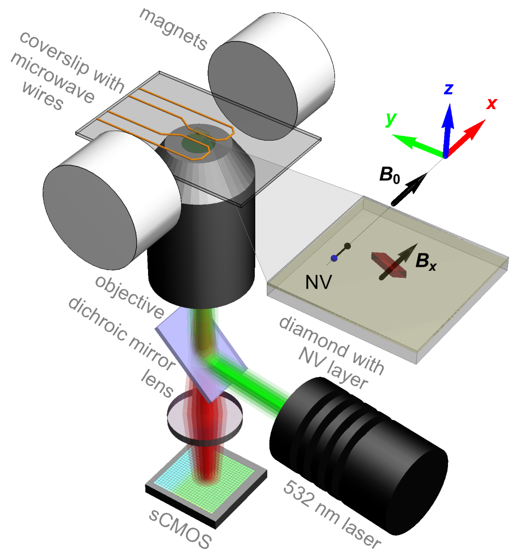

Figure 3.11: The NV magnetic microscope for studying malarial hemozoin.

3.6 Summary

The NV magnetic microscope is capable of nanoscale widefield magnetic microscopy and has been applied in experiments spanning the fields of biology, geology, material science and others. Two realizations of the device created four years apart

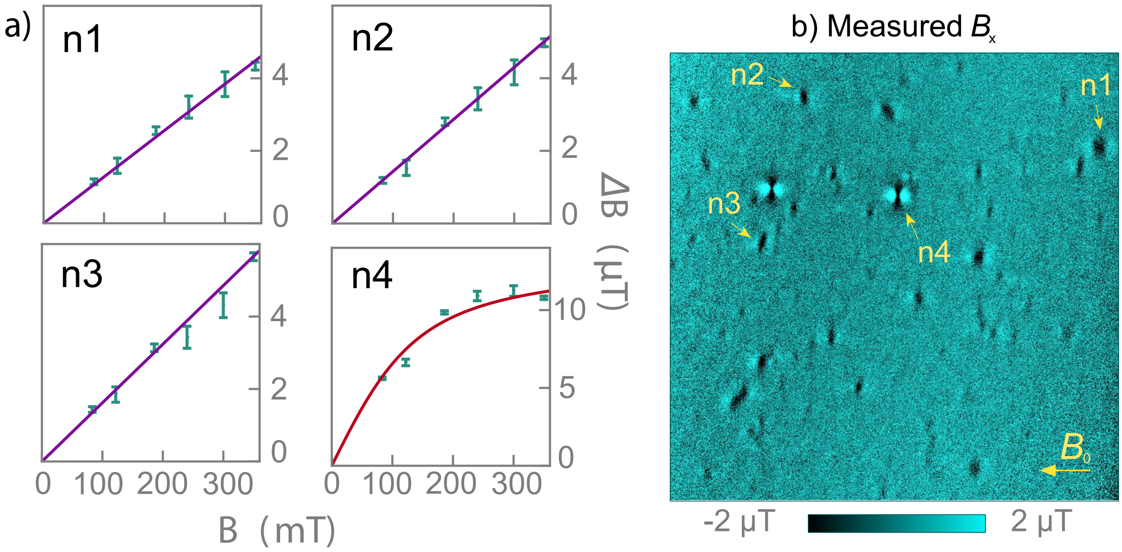

Figure 3.12: Magnetic properties of hemozoin crystals. a) Magnetization dependence on the applied filed strength. b) Magnetic field distribution at a bias field $B_0 = 350\text{mT}$.

showed an order of magnitude increase in sensitivity, by implementing faster and more robust control/acquisition hardware solutions, optimizing the fabrication process of the defects and adapting the device to more severe environmental conditions in terms of both magnetic field and temperature with the goal of coaxing out the maximum amount of signal of the sample.

Some extremely promising research avenues still lie one order of magnitude out of reach: neuronal currents generate magnetic fields that are in the nano- and picotesla range, fields due to thermal nuclear polarization are in the nanotesla range, many time-dependent processes from magnetic microswimmer motion to transient currents in nanoelectric devices are, at this point in time, inaccessible due to the insufficient single-shot sensitivity.

Several approaches to bridging the sensitivity gap are being actively pursued: growing preferentially aligned NV centers [109]–[111] or integrating dynamic decoupling procedures in AC sensing [103]. For nuclear magnetic resonance imaging signal strength could be enhanced by many orders of magnitude by coupling the target nuclei to the NVs and transferring polarization [112], [113] from one species to the other.

Chapter 4

NMR spectroscopy with NV centers

Measuring magnetic fields of submicron volumes might seem like an impressive achievement but only begins to utilize the possibilities opened up by NV centers. The ease with which NV centers can be coherently manipulated with microwaves, means that the AC sensitivity can be pushed to the nano- and picotesla level. This opens up the possibility of chemical analysis of picoliter volumes using the techniques of nuclear magnetic resonance (NMR). In conjunction with the relatively high frequency range over which magnetic fields can be detected (Aslam et al. [114] detected the magnetic field generated by protons precessing in a 3 T external field at a frequency of ∼127 MHz) this makes the NV center a very promising sensor for the next generation of nuclear magnetic resonance (NMR) spectrometers.

While the information that NMR spectroscopy can yield about molecular structure is among the most detailed that can be obtained, the technique is traditionally plagued by a low SNR. The reason for the low SNR is that the signal detected is proportional to the net magnetization of the sample, which, in turn, is very low because the Zeeman energy splitting is low compared to the average thermal energy. Almost all commercial NMR machines detect the signal through a pick-up coil coupled to a high Q-factor resonator. The signal-to-noise ratio of this detection modality scales as $B_0^{7/4}$ [115] (the scaling factor is, however, dependent on the coil geometry and could be slightly different). This has motivated the development of magnets capable of generating ever stronger magnetic fields, but, despite the considerable research effort the field strength has only increased by a factor of 2 over the last 25 years.

This situation further motivates the research into non-inductive alternatives for NMR detection such as NV centers. In order to serve as a meaningful alternative to traditional NMR techniques, the challenges the diamond platform has to meet are two-fold. First, The characteristic magnetic field strengths than need to be detected are in the picotesla or nanotesla range (the latter necessitates working with very shallow NV centers or applying a large magnetic field $B_0 \geq 1\text{T}$ both of which pose additional technical challenges), second, the frequency resolution and field homogeneity and stability have to be in the parts-per-million (ppm) up to parts-per billion (ppb) range in order to provide the relevant spectral information.

This chapter will give a brief introduction in the basic physics of NMR and then proceed to discuss two strategies of reaching the necessary sensitivity and spectral resolution to perform useful NMR spectroscopy experiments using NV centers in diamond.

4.1 Nuclear magnetic resonance spectroscopy

Nuclear magnetic resonance (NMR) spectroscopy exploits the interactions of spins located in different parts of a molecule with each other and with the local magnetic environment. The first experiments registering NMR signals were performed simultaneously by two groups: Purcell, Torrey, and Pound [116] and Bloch, Hansen, and Packard [117]. The former detected a radio-frequency signal from 1 kg of paraffin wax while the latter observed the proton signal from water both in a strong magnetic field.

The source of these signals were the magnetic moments of nuclei. If a nucleus possesses non-zero spin then it has both a magnetic moment and intrinsic angular momentum. If we have a free single nucleus in an external magnetic field it interacts with an external magnetic field (Zeeman effect), and the interaction is described by the Hamiltonian:

$$\hat{H}_{Zeem} = -\mu \cdot \mathbf{B}, \tag{4.1}$$

where μ is the nuclear magnetic moment and $\mathbf{B}$ is the magnetic field. If we assume the magnetic moment is aligned along the field direction, which is assumed to be pointing along the z axis, then:

$$\hat{H}_{Zeem} = -\gamma B_0 \hat{I}_z, \tag{4.2}$$

where, γ is the gyromagnetic ratio, B_0 is the field strength and $\hat{I}_z$ is the spin operator. The eigenstates of this system are the Zeeman basis states:

$$\begin{aligned} \hat{H}_{Zeem} &= E_n|\psi\rangle \\ |\psi\rangle &= |I, m\rangle, \end{aligned} \tag{4.3}$$

and the eigenenergies are:

$$E_n = -\gamma\hbar B_0 m. \tag{4.4}$$

The evolution of a given state under a time-independent Hamiltonian is given by:

$$|\psi(t)\rangle = e^{-I\frac{\hat{H}}{\hbar}t}|\psi(0)\rangle. \tag{4.5}$$

If the system is in an eigenstate of the Hamiltonian no dynamics are observable. However, if the state is not an eigenstate of the Hamiltonian will evolve in time. In other words there will be a time t such that $\langle\psi(t)|\psi(0)\rangle \neq 1$. Let us consider the example of an $I = 1/2$ spin aligned along an axis transverse to the applied field. Without loss of generality let us assume that the spin is aligned along the positive direction of the x axis. At time $t = 0$ the system state is an $\hat{I}_x$ eigenstate:

$$\hat{I}_x|\psi(0)\rangle = \hbar\frac{1}{\sqrt{2}}\begin{pmatrix}1\\1\end{pmatrix} = \hbar\frac{1}{2}|x\rangle. \tag{4.6}$$

Applying expression 4.5 to 4.6 and rearranging the terms we get the solution:

$$|\psi(t)\rangle = \frac{1}{\sqrt{2}}\begin{pmatrix}e^{i\frac{\gamma B_0}{2}t} & 0\\ 0 & e^{-i\frac{\gamma B_0}{2}t}\end{pmatrix}\begin{pmatrix}1\\1\end{pmatrix} = \begin{pmatrix}e^{i\frac{\gamma B_0}{2}t}\\ e^{-i\frac{\gamma B_0}{2}t}\end{pmatrix} \tag{4.7}$$

The time evolution of the state describes a spin precessing in a plane transverse to the applied field direction. The precession frequency is the Larmor frequency

In almost all cases an NMR measurement is performed on ensembles of nuclear spins that are very weakly coupled to the sensor. This means that the act of measuring the system state does not significantly perturb the system and it evolves as if no sensor was present. An NMR measurement is essentially just a series of weak measurements that track the orientation of the precessing spins.

The next few subsections will introduce the core concepts, mathematical formalism and terminology used when discussing NMR spectroscopy.

4.1.1 The density operator

In NMR literature the state of the system is described using the density operator rather than the state function. For a pure state (i.e., where all the spins in the ensemble are in the same state) the density operator can be written as:

$$\hat{\rho}(t) = |\psi(t)\rangle\langle\psi(t)|. \tag{4.8}$$

The evolution of the density matric ir governed by the equation:

$$\hat{\rho}(t) = e^{-i\hat{H}t}\rho(0)e^{i\hat{H}t} \tag{4.9}$$

and the expectation value of an operator $\hat{A}$ is given by:

$$\mathrm{Tr}(\hat{A}\hat{\rho}), \tag{4.10}$$

where Tr denotes the trace of a matrix. In ensemble NMR experiments the system is a mixed state. Each individual spin the system is in some state $|\psi_n\rangle$ with some probability p_n and the state of the system is a statistical mixture of all the individual states. There is no such thing as an average state vector, but it is possible to write down the average density operator of the system:

$$\hat{\rho}_{tot} = \sum_{n}^{N} p_n \hat{\rho}_n, \tag{4.11}$$

here $\hat{\rho}_n$ is the pure-state density matrix describing spin n, and N is the total number of spins in the system. The evolution of the statistical density matrix under a time-independent Hamiltonian is still governed by equation 4.9.

4.1.2 Coherent control

In an external magnetic field a spin system is at thermal equilibrium, and the density matrix is of the form:

$$\hat{\rho}_{tot} = \frac{e^{-\frac{\hat{H}}{k_B T}}}{\mathrm{Tr}\left(e^{-\frac{\hat{H}}{k_B T}}\right)}, \tag{4.12}$$

where k_B is the Boltzmann factor and T is the temperature. If the z axis is chosen to lie along the external field direction (and neglecting all interactions intrinsic to the spin system such as quadrupole interactions) then the representation of the density operator is a diagonal matrix with matrix elements:

$$\rho_{m,m'} = \delta_{m,m'} \frac{e^{(\gamma\hbar m B_0)/(k_B T)}}{\sum\limits_{m=-I}^{m=I} e^{(\gamma\hbar m B_0)/(k_B T)}}, \tag{4.13}$$

where I is the spin quantum number and m is the magnetic quantum number. The net magnetization of the spin ensemble M is:

$$N\gamma\hbar\mathrm{Tr}\left(\hat{I}_z\hat{\rho}_{tot}\right). \tag{4.14}$$

It is much easier to detect the magnetic field generated by a precessing spin than the extremely small DC shift due to the magnetization of the material. That means we need to tip the magnetization by 90°. This is most often done by applying a radio-frequency magnetic field transverse to the static field B_0 described by the Hamiltonian:

$$\hat{H}_{RF} = -\hat{I}_x\gamma\hbar\cos\omega t. \tag{4.15}$$

In this case the field is assumed to be linearly polarized and aligned along the x axis. The dynamics of such a system are usually analyzed by transition to a rotating frame and dropping the terms that average away very rapidly. This procedure transforms a time-dependent problem into a time-independent one. Derivations of this procedure are widely available (an excellent treatment is given in chapter 10 of Levitt [118]) and I will use only the result in the case where the RF frequency is resonant with a dipole allowed ($\Delta m = \pm 1$) transition. The pulse transforms the state in the following way:

$$\rho_{final} = e^{-i\Omega_R \tau \hat{I}_x} \rho_{initial} e^{i\Omega_R \tau \hat{I}_x}, \tag{4.16}$$

$\Omega_R = \frac{\gamma B_1}{2}$ is the Rabi frequency and τ is the evolution time. If $\rho_{initial} = 1/2\hat{S}_x$ and $\tau = \pi/2\Omega$ then $\rho_{final} = \hat{I}_y$. This is essentially the same coherent control discussed in 1.4.1 but applied to the nuclear spins rather than the NV center.

A simple time-domain NMR signal is shown in Fig. 4.1. In real world circumstances the target spins are coupled to the environment that causes the signal strength to decay. The rate of decay and the character of the decay envelope are determined by a wide variety of factors, ranging from coupling strength to neighbouring spins, field homogeneity, coupling anisotropy etc.

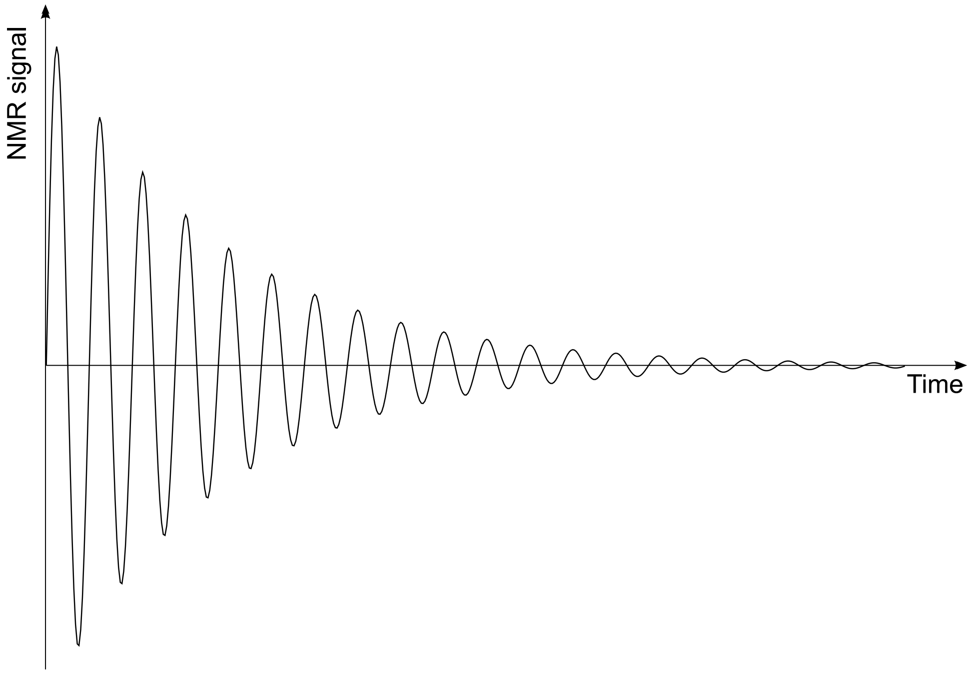

Figure 4.1: A simple NMR signal often also called the free induction decay (FID) signal. The signal envelope decays exponentially with a characteristic decay time of T_2^*.

The accessible frequency resolution is linked to the decay time T_2^* through the Heisenberg uncertainty principle $\Delta E \Delta t \geq \hbar/2$. If the broadening mechanism is entirely homogeneous and the signal envelope is a decaying exponential then then resonance line is a Lorentzian with a scale parameter $\Gamma = \frac{1}{T_2}$. The Lorentzian is a direct result of the Fourier transform of an exponentially decaying harmonic function.

4.1.3 Chemical shifts and spin couplings

The measurements described in previous sections would let us identify the presence of different nuclei as the NMR spectra would contain lines at Larmor frequencies from which the corresponding gyromagnetic ratios could be deduced. This would not be a very informative measurement as there are simpler ways of deducing the elemental composition of a sample which does not rely on detecting exceedingly faint magnetic signals, not to mention the fact that many nuclei have zero net spin and do not generate a magnetic field themselves. The potency of the NMR measurement comes from two sources: position-dependent couplings between nuclear spins and the local magnetic field at the site of the nucleus being altered by the electrons that form the chemical bond.

The latter effect is called the "chemical shift" because the outer shell electrons causing it are also involved in determining the chemical properties of the compound. The chemical shift scales linearly with the applied magnetic field [118] and thus is usually measured in ppm. A ^{1}H spectrum of ethanol is shown in Fig. 4.2; the ^{1}H prefix informs on the spins being targeted, which, in this case, are protons. Other popular target spins are ^{13}C (the more common ^{12}C isotope has no nuclear spin), ^{2}H (useful as a label or reference signal as it has near identical chemical properties as hydrogen but a 6-fold lower gyromagnetic ratio) and ^{15}N (present in all amino-acids and has no quadrupole nuclear moment as opposed to ^{14}N). Other spins are used for more niche applications. In the ethanol molecule spectrum there are three distinct, color-coded groupings of resonance lines, each chemical-shifted to a slightly different frequency. The NMR community has chosen the proton signal in tetramethylsilane to mark 0 ppm for both the ^{1}H and ^{13}C spectra.

The additional structure within the particular groupings is attributable to couplings between the different spins. There are three types of couplings that play an important role in spin-spin interactions. The first is direct dipole-dipole coupling, which has a Hamiltonian of the form:

$$\hat{H}_{d-d} = \frac{\mu_0 \gamma_1 \gamma_2 \hbar}{4\pi r_{1,2}^3} \left[\hat{I}_1 \hat{I}_2 - 3\frac{1}{r_{1,2}^2} \left(\hat{I}_1 \hat{r}_{1,2} \right) \left(\hat{I}_2 \hat{r}_{1,2} \right) \right], \tag{4.17}$$

where $\mathbf{r_{1,2}}$ is the internuclear unit vector. In liquids, the rapid molecular tumbling usually causes this term to average to zero, but in very viscous solutions or solids this is not the case.

The second effect is indirect dipole-dipole coupling, which results from electron-mediated nuclear interactions. Each spin weakly interacts with the electrons resulting in a small electron spin population redistribution (i.e. weakly "magnetizes" the electron spins), which causes a slight shift in the field strength at the site of

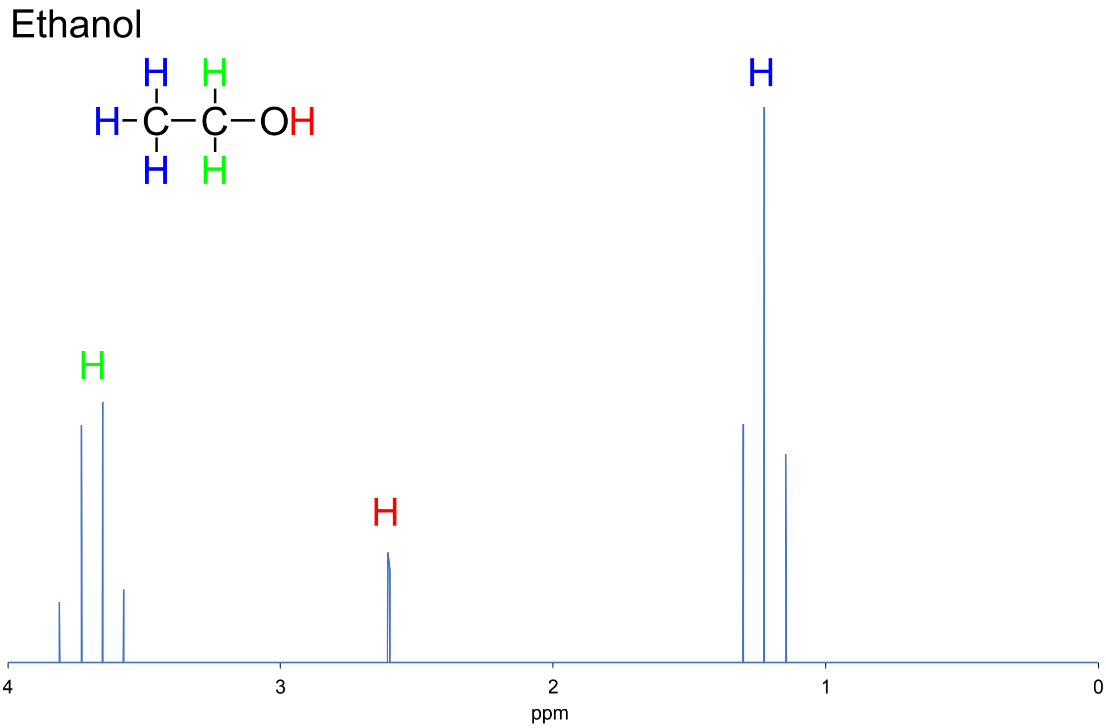

Figure 4.2: The ^{1}H NMR spectrum of ethanol.

adjacent nuclei. These are usually referred to as J-couplings and are of the form:

$$\hat{H}_J = 2\pi \hat{I}_1 \mathbf{J}_{1,2} \hat{I}_2, \tag{4.18}$$

where $\mathbf{J}_{1,2}$ is the spin-spin coupling tensor. The anisotropic part can be separated [53] as it also often averages away due to the rapid molecular tumbling:

$$\mathbf{J}_{1,2} = \mathbf{J}_{1,2}^{\text{iso}} + \mathbf{J}_{1,2}^{\text{aniso}} = J_{1,2} \times \mathbb{1} + \mathbf{J}_{1,2}^{\text{aniso}}, \tag{4.19}$$

where $\mathbb{1}$ is the unit matrix with the correct dimensionality. Finally spins with $S \geq 1$ interact with electric field gradients generated by the surrounding electron clouds. In the principal-axis coordinate system of the nucleus, the Hamiltonian takes the form:

$$\hat{H}_Q = \omega_Q \left[\left(\hat{I}_z^2 - \frac{1}{3} I(I+1) \right) + \frac{\eta}{3} \left(\hat{I}_x^2 - \hat{I}_y^2 \right) \right], \tag{4.20}$$

where ω_Q is the nuclear quadrupole frequency related to the magnitude of the nuclear quadrupole moment and the strength of the local electric field gradients, and η is the electric gradient asymmetry parameter (see [119] for a more detailed discussion).

In the ethanol ^{1}H spectra in Fig. 4.2, no quadrupole interactions are present as $S_{^1\text{H}} = 1/2 < 1$ and direct dipole-dipole couplings as well as anisotropic J couplings are not visible due to motional averaging. The only remaining contributing factor is the istropic J-coupling. These couplings "travel" through bonds but in most systems the interaction strength rapidly drops as the number of chemical bonds increases (a notable exception are aromatic compounds, where the interaction strength can be similar even multiple bond-hops away). However, the natural abundance of ^{12}C spins is much higher than of ^{13}C and the former has zero net spin so the dominant interactions in this example are between the protons color coded in blue and green. The hydrogen color coded in red does not have a significant J-coupling to any of the other protons due to the high electron affinity of oxygen which acts as a buffer for electron-mediated interactions. The number of splitting and their relative amplitudes are determined by the possible combinations of spin orientations and follow Pascals triangle. If we examine the protons marked in green they are coupled to three protons (marked in blue). There is one configuration where all the blue spins are parallel to the green proton $|\downarrow\downarrow\downarrow\rangle$, three configurations with only one blue proton is anti-parallel - $|\uparrow\downarrow\downarrow\rangle$, $|\downarrow\uparrow\downarrow\rangle$, $|\downarrow\downarrow\uparrow\rangle$ - three configurations with two blue protons are anti-parallel $|\uparrow\downarrow\uparrow\rangle$, $|\uparrow\uparrow\downarrow\rangle$, $|\downarrow\uparrow\uparrow\rangle$ - and finally one configuration where all blue protons are anti-parallel: $|\uparrow\uparrow\uparrow\rangle$.

Even such a simple molecule as ethanol has quite a complicated structure arising from the different spin-spin and spin-field interactions. However, interactions are usually spatially localized and the overall transition frequency is usually dominated by the chemical shift both separating the multiplets, which avoids overlap, and hinting at the functional groups present. This allows researchers to elucidate the structure of very complicated molecules such as proteins.

4.1.4 Motivation for using NVs as an alternative sensing platform

The induction-based NMR analysis is a very mature platform and the advances in the sensitivity/performance have been mostly incremental: slightly higher fields, slightly higher magic-angle-spinning frequencies. When considering nanoscale sensing, the field of microcoil-based NMR especially in the nL–pL range has benefited greatly from the maturing of microfabrication techniques for both the solenoid itself and, what is often the more challenging part, the sample delivery system. Planar microcoil designs have been able to obtain NMR spectra from single eggs (100 pL from wish or water flea) using planar microcoil designs [120], [121] and even integrating the planar coil design into a microfluidic platform allowing for a liquid/biologically favorable environment while holding the sample in place[122]. Other topologies besides planar have also reported sub-nL sensing capabilities however each of them have specific drawbacks. Solenoidal geometries [123], [124] suffer from low fill factors in order to circumvent susceptibility broadening [125], striplines and microslots have poor sensitvity scaling to the sub-nL level [126]. All induction-based detectors also suffer from some common problems: parasitic detection regions formed by the leads connecting the sensing element to the amplifier, large effective sensing volumes (in the recent pL-scale papers [120]–[122] the sample was larger than the sensing volume of the coil), which adds a larger-than-desired solvent contribution to the signal, and, finally, NMR resonance linewidth broadening due to susceptibility mismatch between the solvent/sample and the inductor metal.

Another significant issue presenting itself at the nanoscale is local magnetic field gradients due differences in magnetic susceptibilities between the sample and the detector. The local magnetic field variation at distance r and angle around a cylinder (a reasonable approximation of a solenoid) with magnetic susceptibility χ is [127]:

$$\Delta B = \frac{B_0 \sin^2(\theta)\cos(2\phi)}{2r^2} R^2 \Delta\chi, \tag{4.21}$$

where B_0 is the static magnetic field θ is the angle between the cylinder axis and the external field, $\Delta\xi$ is the difference between magnetic susceptibilities and R is the cylinder radius. To obtain reasonable fill factor values the wires of the sensor coil have to be very thin. If we treat the example in [121] where 0.35 μm thick wires are used (assume copper-air interface), then the magnetic field difference across the sample is 2ppm. This can be somewhat offset by reducing $\Delta\chi$. This can be done by immersing the coil in a non-conductive material of a magnetic susceptibility close to that of the inductor material (-9.6×10^{-6} for copper)[128]. One would think that due to the relatively high magnetic susceptibility of diamond (-2.2×10^{-5}) the problem would be even more pronounced for NV based sensors. However since the sensing volume is defined not by the dimensions of the diamond itself but rather by the NV region being optically addressed the diamond chip can be (and usually is) much larger compared to the sensing volume making the gradients across it vanishingly small (see SI of [129] for a more detailed discussion).

Despite the numerous drawbacks listed in the previous paragraphs at this point in time inductive detectors are still very competitive in the field of pL detection. An overview of different approaches capable of picoliter scale sensing are shown in Fig. 4.3. The inductive systems are pushing up against their intrinsic limits both in terms of sensitivity and spectral resolution while the potential of NV based detectors still remains untapped. In the last 4 years the spectral resolution of the NV NMR spectra have increased by 3 orders of magnitude and intensive ongoing research is exploring the possibility of polarization transfer from NVs to analyte nuclei netting another multiple orders of magnitude improvement in terms of sensitivity. The hyperpolarization enhancement has already been demonstrated when performing ^{13}C NMR measurements on the carbon spins that form the diamond

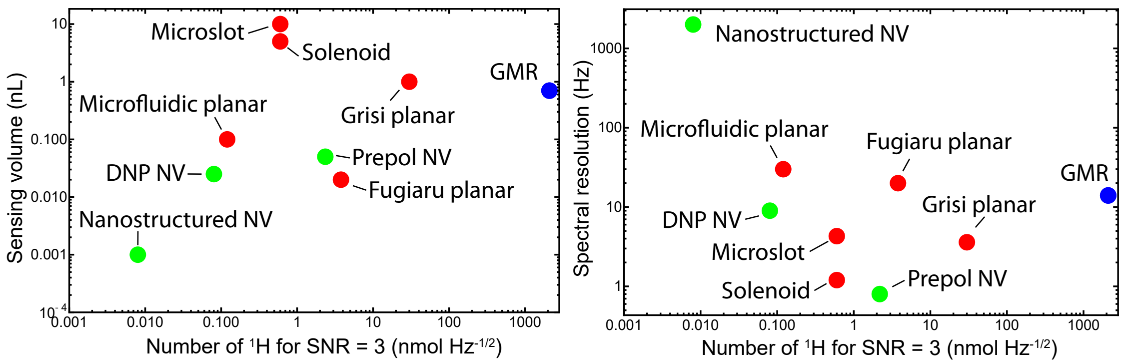

Figure 4.3: The landscape of picoliter NMR methods comparing sensing volume and absolute spectral resolution. The induction based method sensitivity is rescaled assuming a field equivalent to 300 MHz ^{1}H Larmor frequency while all other values are reported as they appeared in the original paper. The data sources are as follows: nanotstructured NV [7], microslot [130], solenoid [131], microfluidic planar [122], Fugiaru planar [120], Grisi planar [121], prepol NV [129], DNP NV [132], GMR [133], single NV [114].

lattice (see for example [112]) and active research is exploring different strategies of polarization transfer.

Another more subtle argument aspect in which the NV centers are a perspective NMR platform is the sophistication of sample isolation techniques especially liquid-chromatography (LC) combined with solid-phase-extraction (SPE). This enables work with very high sample concentrations while still needing small amounts of sample. The nitrogen vacancies have potential to move to even smaller sensing volumes while maintaining similar sensing properties while their inductive counterparts cannot. LC has demonstrated separation of nanomolar quantities of biologically relevant small molecules [134], [135] High performance LC machines are commercially available (see for example Bruker [136]) and are easily integrated with microfluidic systems. SPE compliments the separation capabilities of LC and is already broadly used by the NMR community when studying biological matter [137]–[140]. It's main attraction in the context of very-small sensing volume detection is that by limiting the amount of solvent used the concentration can be increased limited only by sample-handling and peak broadening due to susceptibility mismatch [135].

4.2 Nitrogen vacancy NMR spectroscopy exploiting statistical polarization

The first papers reporting on ensemble NV NMR signals from spins not belonging to the diamond host [141], [142] exploited the effect that if the effective sensing NMR is very small the stochastic polarization (i.e. the probability that at any point in time there might be more spins pointing along the +x direction than the -x direction) can become substantial. A comparison between statistical polarization and thermal polarization (the small net polarization due to the energy difference between the Zeeman sublevels) for protons in water at two different field strengths is shown in Fig. 4.4. As can be seen as the volume shrinks below 1 μm^3 the field

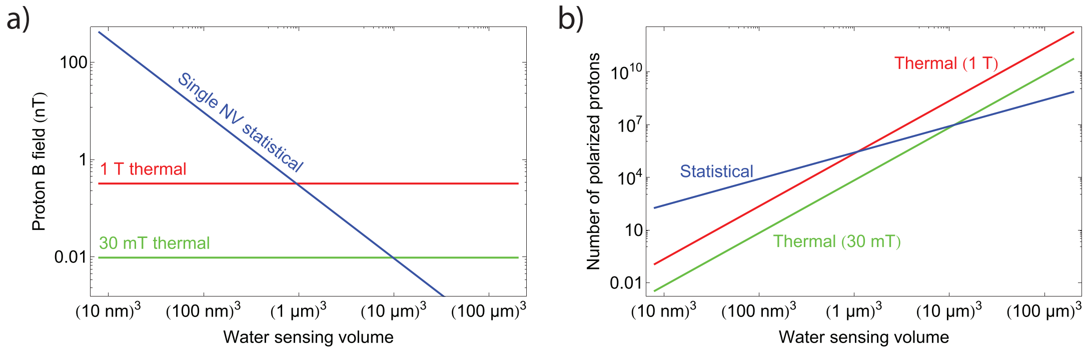

Figure 4.4: Thermal vs statistical polarization; a) the magnetic field produced by the target spins as a function of volume b) the number of polarized spins as a function of volume.

from the statistically polarized protons rapidly increases. This section will discuss published work [7] on detecting statistically polarized analyte spins with increased signal-to-noise ratio achieved by nanostructuring the sensors surface. The authors contribution in this work was acquiring and analyzing a portion of the experimental data

4.3 Detecting statistical polarization with NV centers in diamond.

The effective sensing volume of an NV center is determined by the sensor-analyte distance. Fig. 4.5 shows a side-by-side view of two NV centers at different depths. Each spin a magnetic dipole generating a field that falls of as $1/r^3 \sim 1/V$, where V is the sensing volume, the number of statistically polarized spins scales as $\sqrt{V}$ so the overall scaling of the signal strength due to statistical polarization versus sensing volume is $V^{-1/2}$. For thermal polarization this quantity is constant as the number of polarized spins is linear in volume and the overall signal strength is constant. Another factor that has to be taken into account is the experiment geometry. As discussed before, when operating at field below ∼ 1000G the NV centers are proportional only to the magnetic field component along the natural NV quantization axis. Then the RMS field sensed by the NV centers needs to be multiplied by an additional geometric factor:

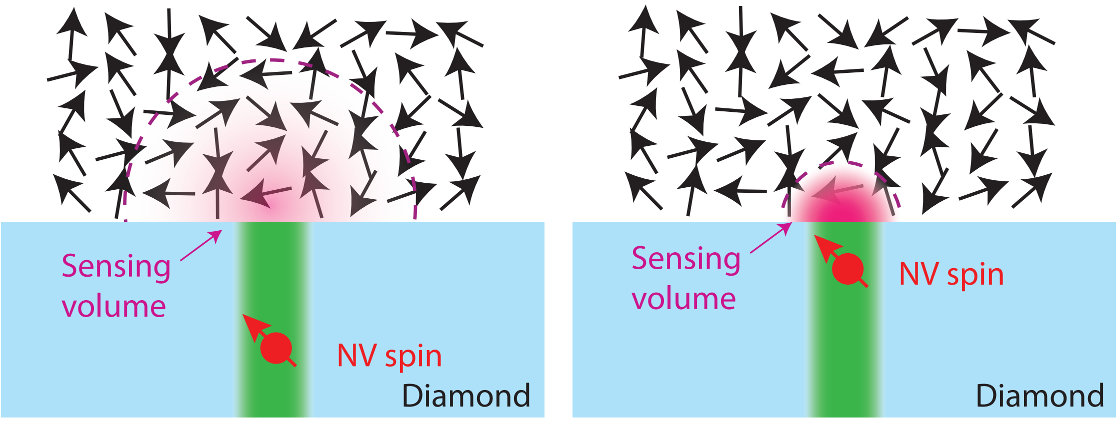

Figure 4.5: Effective sensing volume for NV centers at two different depths. For shallow NVs the majority of the signal is contributed by a few strongly interacting spins near the diamond surface.

$$B_{\mathrm{RMS}}^2 = P(\alpha)\left(\frac{\mu_0 h\gamma_{nuc}}{4\pi}\right)^2 \frac{\rho}{d_{NV}^3} = \frac{\pi(8-3\sin(\alpha)^4)}{128}\left(\frac{\mu_0 h\gamma_{nuc}}{4\pi}\right)^2 \frac{\rho}{d_{NV}^3}, \tag{4.22}$$

where ρ is the nuclear spin number density, α is the angle the N-V axis makes with the normal to the substrate surface, $P(\alpha)$ is the geometric prefactor and d_{NV} is the depth of the NV center below the diamond surface. A derivation of expression 4.22 is given by Pham et al. [141]. As the average NV depth must be very small this constrains the average depth of the NV ensemble. As the NV ensemble density is also limited due to performance degradation (see chapter 2) the amount of fluorescence is also weak leading to a poorer shot-noise limited performance. To combat this we etched grooves in the diamond substrate (Fig. 4.6) before nitrogen implantation and annealing. This increased the effective surface area and thus the number of NV centers in the FOV while still maintaining a limited sensor-sample distance and high statistical polarization. The fluorescence comparison between a flat and a grooved sample are shown in Fig. 4.6(b). To confirm that all of the sensitive region were in contact with the analyte (i.e. whether there were any wetting issues) water stained with Alexa 405 dye was deposited on the diamond and imaged with a confocal microscope. As can be seen in Fig. 4.6(c) the analyte wets the sample well and pentrated deep into the grooves.

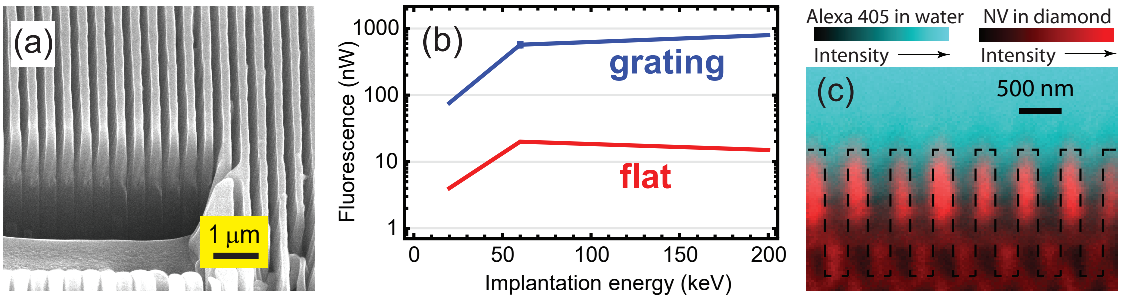

Figure 4.6: Nanostructured diamond surface for higher SNR. a) SEM image of the etched grooves. b) Performance enhancement of nanostructured vs flat diamond. The fluorescence level is significantly higher due to the larger number of NV centers in contact with the analyte in the same field of view. c) Confocal image of the diamond with dye-stained water dispersed on top of it. The dashed lines represent the diamond-water boundary.

4.3.1 AC magnetometry of statistically polarized sources

The simplest implementation of an AC magnetometry sequence is the Hahn-echo measurement already discussed in section 1.4.2. For an NV center evolving in the presence of a fluctuating magnetic field and under the influence of a decoupling sequence such as Hahn-echo the probability of finding the NV electronic spin in state $|m_s = 0\rangle$ after a free evolution time τ_{tot} is equal to [13]:

$$p(\tau) = \frac{1}{2}\left(1 - \langle \cos\phi(\tau_{tot})\rangle\right), \tag{4.23}$$

if the phase of the first microwave $\pi/2$ pulse is equal to the phase of the last one and:

$$p(\tau) = \frac{1}{2}\left(1 - \langle \sin\phi(\tau_{tot})\rangle\right), \tag{4.24}$$

if the phase of the second pulse is shifted by $\pi/2$ with respect to the first one. The term $\phi(t)$ is the average phase accumulated during the evolution time:

$$\phi(t) = \gamma \int f(t)B(t)dt. \tag{4.25}$$

The function $f(t)$ characterizes the influence of the pulse sequence on the perceived magnetic field of the spin. This influence is summarized in Fig. 4.7. The first thing to notice is that any low frequency and DC components of the magnetic field will average to zero (as it should be for an AC magnetometry sequence), second, AC components that are off-resonance with pulse sequence will also be attenuated. The resonance criteria is that the phase acquisition time τ before and after the π pulse equals a half-period of the oscillating field. Finally the sequence is also phase-sensitive as can be seen when comparing Fig. 4.7 (b) and (c). The rejection of off-resonance components means that the pulse sequence effectively acts as a bandpass

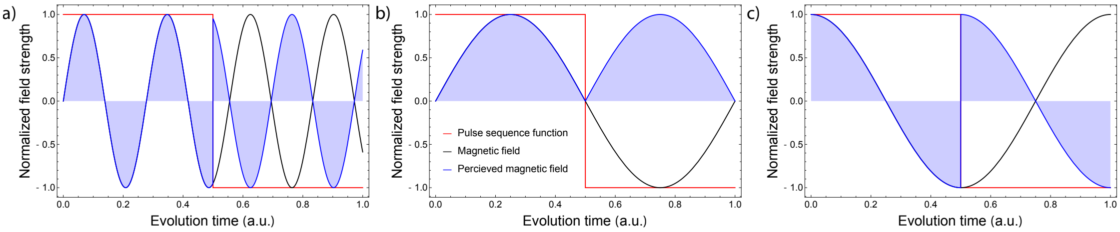

Figure 4.7: Magnetic field perceived by the spin for a field off-resonance with the pulse sequence (a) and on-resonance in-phase (b) and on-resonance $\pi/2$ phase shifted.

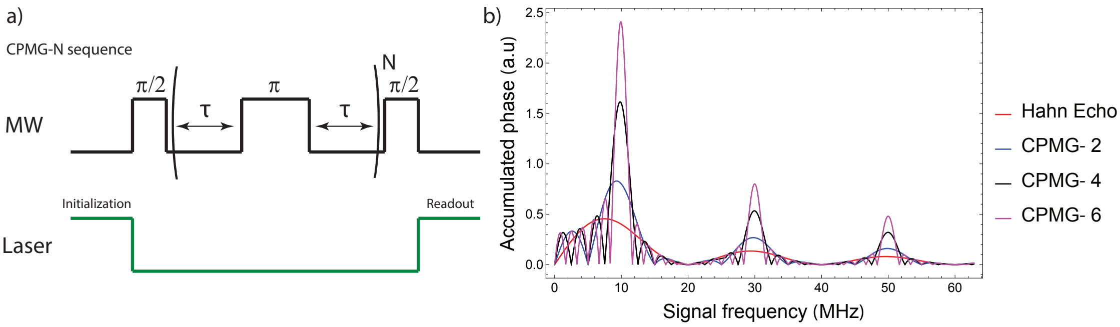

Figure 4.8: The CPMG pulse sequence (a) and comparison of accumulated phase for a given passband for Hahn-echo and different order CPMG sequences. The data were simulated assuming a signal perfectly in-phase with the pulse sequence.

filter decoupling the NV spin from a portion of the environmental magnetic field noise. The passband of the filter is determined by the spacing between pulses and the bandwidth can be reduced by introducing additional pulses in the pulse sequence. The Carl-Purcell-Meiboom-Gill (CPMG) pulse sequence is an extension of the Hahn-Echo sequence which does exactly that (see Fig. 4.8(a)).

When detecting repeatable coherent signals such as the AC fields generated by thermally polarized spins the phases of the first and last $\pi/2$ pulses should be shifted by $\pi/2$ with respect to one another as in the low field limit this will lead to a change in fluorescence linear in the field strength (the Taylor expansion of eq. 4.24 with respect to magnetic field), while there is only a second order change in field if both phases are the same. However, the field from statistically polarized sources have both random amplitude and phase with a mean value around zero, thus only the root-mean-squared (RMS) component of the field can be detected by setting both of the $\pi/2$ pulse phases to be equal. In the small field regime and assuming that the magnetic fields are Gaussian distributed [13], [143] the probability of finding the NV spin in state $|0\rangle$ after a phase accumulation time τ_{tot} is:

$$p(\tau_{tot}) = \frac{1}{2}\left(1 + e^{-\langle\phi(\tau_{tot})^2\rangle/2}\right) = \frac{1}{2}\left(1 + e^{-\chi(\tau_{tot})}\right), \tag{4.26}$$

where:

$$\chi(\tau_{tot}) = \gamma^2 \int S_B(\omega) \frac{F(\omega\tau)}{2\pi\omega^2} d\omega. \tag{4.27}$$

$S_B(\omega)$ is the magnetic noise (analyte + other magnetic sources) power spectrum of the environment and $F(\omega\tau)$ is the filter function of the pulse sequence. For a Hahn-echo sequence $F(\omega\tau) = 8\sin^4 \frac{\omega\tau}{4}$ and for a CPMG-N sequence (N is even) $F(\omega\tau) = 8\sin^4 \frac{\omega\tau}{4N} \sin^2 \frac{\omega\tau}{2} / \cos^2 \frac{\omega\tau}{2N}$ [143] (note that τ is different from τ_{tot}, the former is defined in Fig. 4.8(a) while the latter characterizes the total phase acquisition time.

By sweeping the time τ the passband of the pulse sequence samples the magnetic field intensity at different frequencies netting the magnetic noise spectrum. This is analogous to a noise measurement with a lock-in amplifier where the quantity being swept is the modulation frequency. The frequency resolution of the NV noise spectroscopy measurement is not infinite, it is fundamentally limited by the transverse relaxation time T_2. While the decoupling sequence somewhat extends it, at room temperature ensemble decoherence time peaks at $\sim$ 1 ms [13] even for very dilute nitrogen concentrations. Nitrogen implanted samples tend to perform even worse due to the additional lattice damage introduced during the ion implantation step. In any event the short comparatively short T_2 times of NV centers compared to nuclear spins limits the accessible NMR spectral resolution to several kHz. In a 3 T bias field this is equivalent to 10-100 ppm rendering the sensor useless.

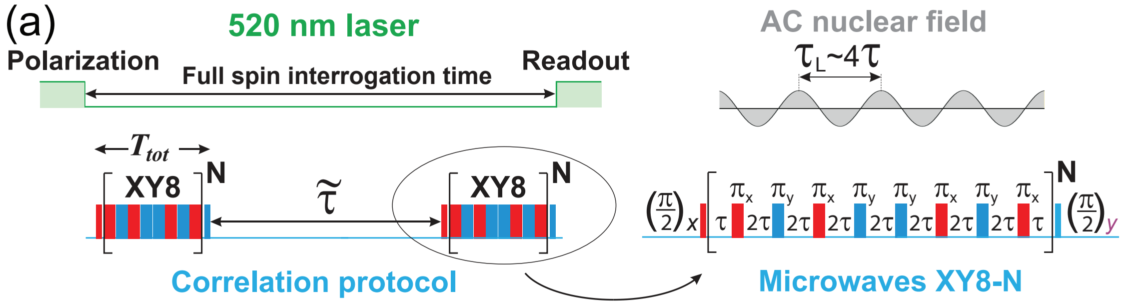

Figure 4.9: The correlation pulse sequence consisting of two XY8 sequences seperated by the correlation time $\tilde{\tau}$.

It is possible to extend the effective relaxation time to the NV longitudinal relaxation time T_1 by employing a correlation protocol consisting of two pulse trains separated by a correlation time $\tilde{\tau}$ 4.9. An XY8 sequence was used instead of a CPMG sequence as it has demonstrated better robustness against pulse timing/phase errors [144]. During the evolution time $\tilde{\tau}$ the accumulated phase during the evolution under the first pulse sequence is stored in the longitudinal component of the NV spin and then correlated. The derivation for the signal intensity as a function of the sequence parameters for a Hahn-Echo sequence is given by Laraoui et al.[145] (see also SI of [7]):

$$F_{\mathrm{HE}} = F_0 \left[\left(1 - \frac{C}{2}\right) + \frac{C}{4} \left(\frac{4\gamma_{NV} B_{\mathrm{RMS}}}{\omega} \sin^2\left(\frac{\omega\tau}{2}\right)\right)^2 \cos\left(\omega(2\tau + \tilde{\tau})\right)\right], \quad (4.28)$$

where F_0 is the mean fluorescence intensity, C is the peak to peak correlation spectroscopy fluorescence contrast (essentially the Rabi contrast taking into account signal decay due to T_2 relaxation), B_{RMS} is the RMS nuclear magnetic field amplitude, $\tau$is the phase acquisition time between the $\pi/2$ and π pulses in a Hahn-echo, $\tilde{tau}$ is the time between the two pulse sequences and $\omega = 2\pi\gamma B_0$ is the nuclear Larmor frequency. When using a CPMG (XY8) sequence the fluorescence expression is similar with the only change being an appropriate selection of the filter function [143]:

$$\begin{aligned} F_{\mathrm{CPMG/XY8}} = F_0 \Bigg[\left(1 - \frac{C}{2}\right) + \\ + \frac{C}{4} \left(\frac{4\gamma_{NV} B_{\mathrm{RMS}}}{\omega} \sin^2\left(\frac{\omega\tau}{2}\right) \frac{\sin(2\omega\tau N)}{\cos(\omega\tau)}\right)^2 \cos\left(\omega(2\tau + \tilde{\tau})\right)\Bigg]. \end{aligned} \quad (4.29)$$

The effective relaxation time can be extended even further than the T_1 time of the NV center by transferring the phase information to the adjacent nitrogen nuclear spin [114], [146]. The nuclear spin in this setting is referred to as a quantum memory and it can store the information from hundreds of milliseconds to multiple seconds depending on the environmental conditions enabling operation in the ppb regime.

The correlation NMR experiments consists of a series of measurements sweeping $\tilde{\tau}$. The relative NV fluorescence intensity $\Delta F/F$ is modulated at the nuclear Larmor frequency similar to a standard NMR measurement. The experimental results for a correlation experiment are shown in Fig. 4.10(a). The NMR spectrum is obtained by a Fourier transform of the time dependent signal and the extracted gyromagnetic ratios agree well with the expected values for the corresponding spin species. The minimum detectable concentration for Fomblin$^{\mathrm{TM}}$ - defined as the number of spins necessary to reach a SNR value of 3-to-1 in 1 second of integration - is $\rho_{\min} = 40 \pm 2 \times 10^{24}$ spins/liter. This is equivalent to 4 ± 0.2 picomoles of analyte spins.

The method does, however, suffer from a crucial flaw when it comes to high spectral resolution sensing. While the sensors effective coherence time can be extended far enough ($\sim$ 1 s) to provide adequate spectral resolution for meaningful NMR measurements (couple of ppm) the limiting factor is the correlation time of the target spin itself. For nanoscale sensing volumes the analyte spins are free to move and rapidly diffuse through the sensing volume (see Fig.4.11(a)). As

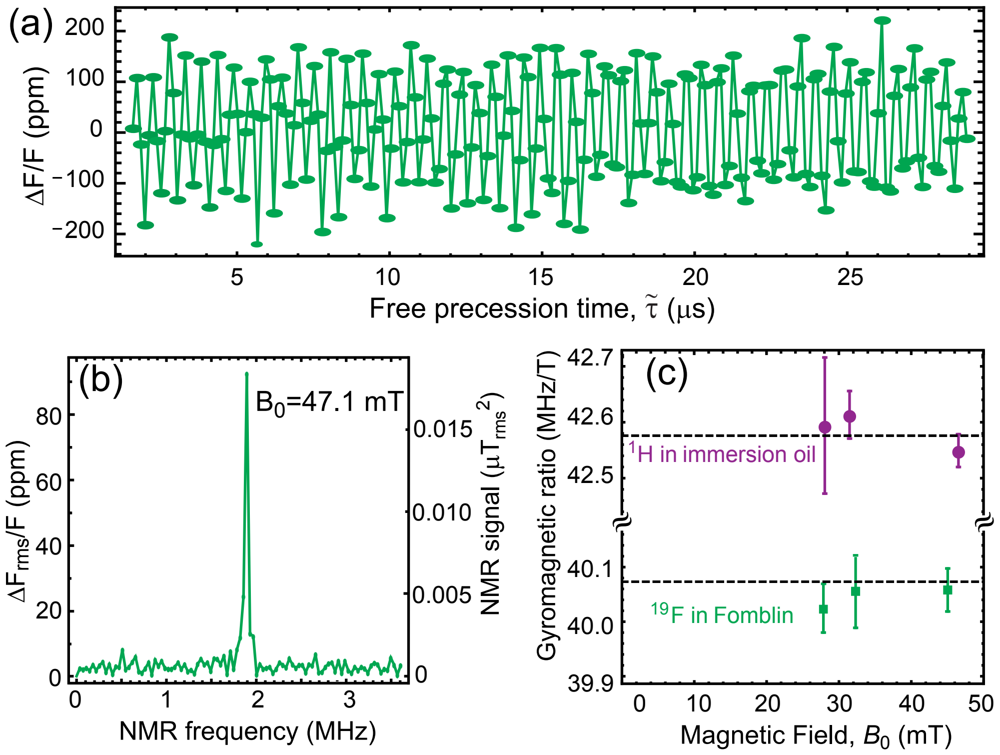

Figure 4.10: An NMR correlation experiment. Fluorescence as a function of correlation time $\tilde{\tau}$ (a). Fourier transform of the correlation signal (b). Field dependence of the NMR peak position for a ^{1}H rich (immersion oil) and ^{19}F rich (Fomblin$^{\text{TM}}$) samples.

one spin leaves the sensing volume, another may enter but their phases are entirely uncorrelated (see Fig. 4.11(a)). The spin dynamics can be considered an Orenstein-Uhlenbeck stochastic process [13], [141], [143] with a known power spectral density function:

$$S(\omega) = B_{\text{RMS}}^2 \frac{2\tau_c}{1 + (\omega - \omega_L)^2 \tau_c^2}. \tag{4.30}$$

The diffusion limited correlation time τ_c is equal to [7], [141]:

$$\tau_c = \frac{2d_{NV}^2}{D}, \tag{4.31}$$

where d_{NV} is the mean depth of the NV layer and D is the nuclear spin diffusion coefficient. The experimental observations support the model: the signal decay envelope is an exponential (Fig. 4.11(b)) a Fourier transform of which leads to a peak with a Lorentzian profile (described by eq.4.30), and the correlation time increases as the square of the NV depth (which in turn at the voltages used is proportional to the implantation energy) as shown in Fig. 4.11(c). Several groups have reported chemical resolution NMR performed with NV center probing statistical polarization [114], [147] but these were highly complicated experiments. Aslam et al. achieved 1 ppm resolution while probing the statistical polarization

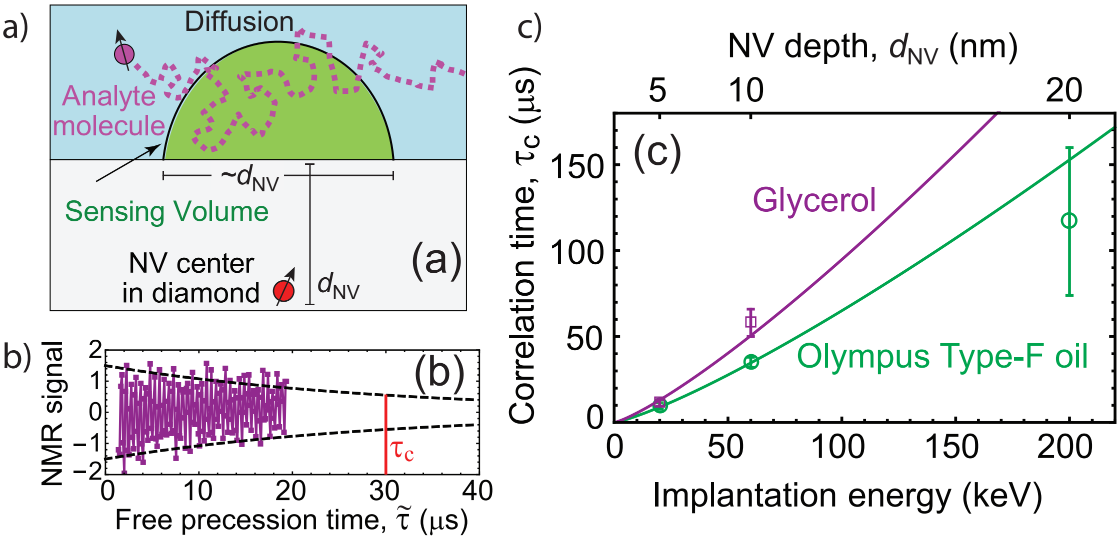

Figure 4.11: (a) Diffusion in nanoscale NV NMR. The effective sample volume is defined by the depth of the NV center beneath the surface. The correlation time is defined by how quickly on average the spin leaves this volume due to diffusion. (b). The signal envelope of the time-dependent signal is a decaying exponential where the time constant is the correlation time (c). The sensing volume and the correlation time can be increased by increasing the nitrogen implantation energy and thus the average depth of the NV centers. Two correlation time and the NV depth are related by expression 4.31.

of a sample by implanting the NV sensor 30 nm beneath the diamond surface, using very viscous analytes, going to a high magnetic field (3T), and using the adjacent nitrogen nuclear spin as a quantum memory for increased effective sensor relaxation times. However, the increased sensor depth lead to poor signal to noise ratio and a total averaging time of multiple days for some samples. Additionally for very viscous substances the motional averaging that suppresses line broadening due to dipole-dipole coupling becomes less efficient again limiting the accessible spectral resolution.

Several papers have outlined potential strategies of how to extend the diffusion limited correlation time and they mostly involve spatial confinement by various means for example encapsulating analyte in liposomes or polymer shells, techniques already employed in microcoil based NMR. Other approaches [147] have involved surface functionalization with species that bind to proteins and immobilize them. The drawbacks of both of these approaches are possible impact on the molecular structure and properties of the species being examined as well as additional engineering and technical complexity.

4.4 Microscale sensing of thermal polarization

While promising on account of their larger SNRs, achieving a high spectral resolution with this technique is an enormous technical challenge. As a result, we decided to pivot to NMR based on thermally polarized spin signals. These signals are much weaker, but do not suffer from the diffusion issue as all the spins are in phase. The field magnitude generated by an ensemble of thermally polarized spins can be estimated as:

$$B_{\text{therm}} \sim \frac{\mu_0}{4\pi}\frac{h^2\gamma^2 B_0\rho}{4k_B T}. \tag{4.32}$$

The decoupling sequences for AC sensing described in the previous section are hard to implement if the nuclear Larmor frequencies are larger than a a 100-200 MHz as the requirements on both pulse duration and power delivery become very stringent. For proton spins the equivalent field is around 2000 G. Techniques such as electron-nuclear double resonance (ENDOR) can be used employed at higher fields but they will not be discussed further in this work. Using expression 4.32 for pure water at 2000 G (spin concentration $\rho = 6.7 \times 10^{25}$ spins/L) gives a signal field strength estimate of 600 pT. In reality the measured value is smaller due to geometric factors (physical dimensions of sample/sensing layer and NV axis orientation) but still well within the capabilities of NV sensors. Nevertheless the first paper reporting on thermal NMR signals from an external analyte at room temperature came out only in 2018 (2017 on ArXiv) where Glenn and Bucher et al. [40] demonstrated a 9 Hz spectral resolution while working at an external field $\approx$ 900 Gauss, most probably limited by temporal/spatial inhomogeneities of the bias field, and a molar sensitivity of ~ 370 M$\sqrt{\text{Hz}}$.

This section will describe the work on the realization of NV thermal NMR sensing in a microfluidic platform yielding order-of-magnitude improvements in both sensitivity and spectral resolution.

4.4.1 High resolution sensing of coherent AC signals

The key-enabling technique enabling high-resolution NV NMR was reported on two papers submitted in January and July of 2017 [40], [148]. While differing in implementation details both papers exploited the fact that the dynamic decoupling sequences described in the previous section are phase sensitive and that the signals under investigation are not perturbed by the measurement process. The principles of the methods are shown in Fig. 4.12. The measurement consists of a series of dynamic-decoupling (be it CPMG-N, Hahn-echo or, as it is in the case shown here, XY8-N) sequences sampling the phase of the nuclear field at set intervals. The

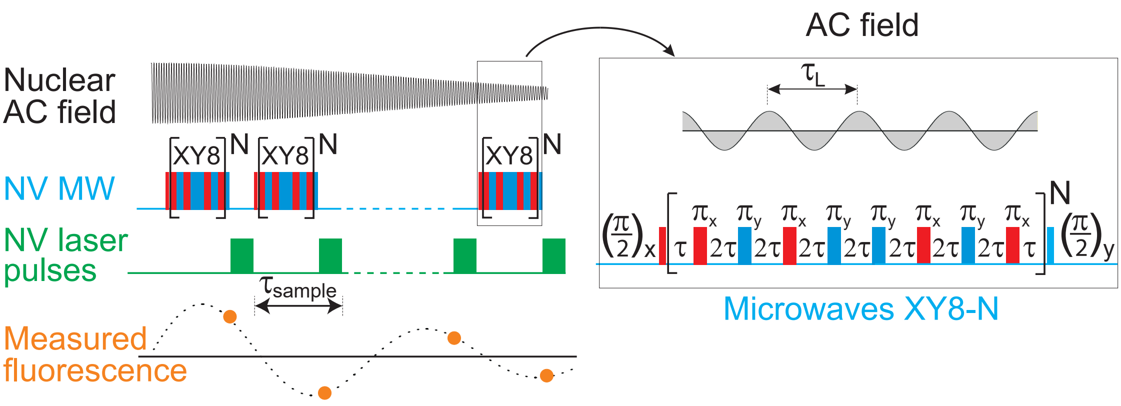

Figure 4.12: High resolution AC sensing with NV centers. The measurement consists of repeated XY8-N sequences spaced a set time apart. The fluorescence modulation frequency is determined by the nuclear AC frequency and the readout repetition frequency.

fluorescence signal as a function of time is then:

$$F = F_0 \left[1 + C/2 \sin\left(4\gamma B_{\mathrm{AC}}(\omega) S(\omega_0) \tau_{\mathrm{tot}}\right) \cos\left((\omega - \omega_{\mathrm{alias}})t + \phi_0\right)\right], \tag{4.33}$$

where c is the residual peak-to-peak contrast after the XY8-N pulse sequence, τ_{tot} is the total phase acquisition time of the pulse sequence, $B_{\mathrm{AC}}(\omega)$ is the nuclear magnetic field amplitude precessing at ω - the Larmor frequency -, $S(\omega)$ is the filter function of the pulse sequence, ω_{alias} is the sampling frequency (or in other words the repetition frequency of the XY8 pulse sequences) and ϕ_0 is the phase of the nuclear precession with respect to the first logged $\pi/2$ pulse. The frequency measurement is severely aliased but normally the NMR signal is located very near the value given by the g-factor of the nuclear species (absent strong static interactions such as dipole-dipole or quadrupole for spins with higher multiplicity) removing any ambiguity of the frequency measurement. Additionally the narrow passband of the XY8 sequence rejects noise present at other frequencies that could be folded in with the spectral region of interest.

Another positive aspect of this detection scheme is that the whole FID is acquired during one measurement as opposed to sweeping a parameter of the sequence as was the case in the correlation sequence described in the previous section. This maintains a constant excitation/readout duty cycle, and avoids any artefacts related to NV1$^-$/NV^0 photodynamics, as well as limiting the number of times the measurement software needs to communicate with the timing pulse hardware decreasing unnecessary downtime.

The low signal values still pose a significant technical challenge. This problem is further exasperated by temporal and spatial external field inhomogeneities that broaden the NMR line and make it that much harder to detect against the baseline noise. The long-term temporal drifts of commercial power supplies also severely inhibit averaging times without additional feedback mechanisms in place. To combat the issue of low signal strength we embedded the diamond sensor in a microfluidic platform and spatially separating the detection and polarization steps of the experiment. This prepolarization technique enabled us to polarize the analyte at a high (1.5 T) magnetic field while performing the measurement at only 13 mT where both the diamond sensor performance and field homogeneity are much more easily optimized. In this configuration we obtained a spin sensitivity of $27\mathrm{M}\sqrt{\mathrm{Hz}}$ and a spectral resolution of 0.655 Hz both on a sensing volume of 40 pL.

The enhanced performance allowed us to perform two-dimensional (2D) nuclear correlation spectroscopy (COSY) of liquid analytes for the first time in a NV ensemble sensor.

4.4.2 Experimental details

The prepolarization concept is shown in Fig. 4.13. The analyte is housed in a helium-pressurized container connected to the microfluidic system. Before each experiment the analyte is heated up and sonicated in an ultrasonic bath. Helium is used due to its low solubility in most liquids and sonication minimizes the amount of solute gas (mostly CO_2 from the atmosphere) present in the analyte. These steps are in order to avoid bubble formation in the microfluidic system. Before arriving at the sensing area the analyte is housed in the Hallbach array until it reaches thermal equilibrium, then it is quickly shuttled to the sensing with a shuttling time smaller than the T_1 time of the analyte. We estimate that around 80% of the equilibrium polarization at 1.5 T is retained. The microfluidic system is operated in a stop-flow regime with the aid of two microfluidic switches located before the Hallabach array and after the diamond chip. Two switches are necessary to maintain constant pressure in the channel and avoid undesirable fluid flow caused by expansion/contraction of the microfluidic tubing.

The microfluidic chip is shown in Fig. 4.14. The body of the microfluidic chip is formed by a 2 mm wide channel milled into a glass microscope slide with a diamond drill. One side of the channel is sealed with a 150μm coverslip while the other is capped off with another glass slide on which microwave traces are deposited. The sensor is 35-μm-thick diamond membrane with (100) polished faces. The membranes were formed from chips grown by chemical-vapor-deposition with a nitrogen density of 20 ppm. The chip was laser-cut into the thin membranes, implanted with 10^{18} $\mathrm{e}^{-}1/\mathrm{cm}^2$ accelerated to 2 MeV and annealed at 800-1100 °C using the recipe described in [7]. The inlets and outlets were constructed by drilling two 0.5 mm diameter holes in the base microscope slides and attaching two rubber

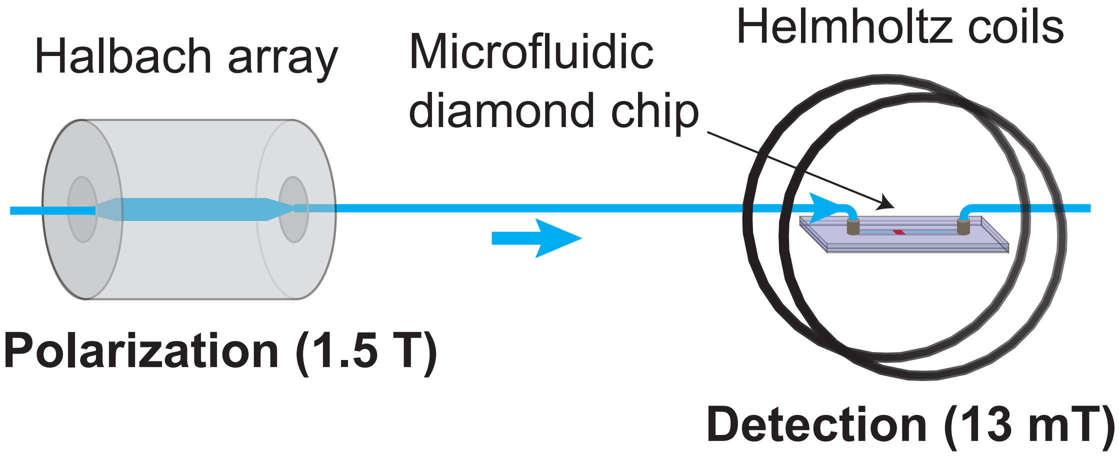

Figure 4.13: The prepolarization setup. Analyte is flown through a high-magnetic field area generated by a Hallbach array. The analyte polarizes in this region and is then quickly shuttled (with a shuttling time lower than the T_1 of the analyte) to the sensing area where a homogeneous 13 mT field is generated by a pair Helmholtz.

stoppers were glued to the base of the slide with double-sided tape. Microfluidic PEEK tubing was pushed through holes drilled in the rubber stoppers. A conventional NMR system consisting of of a $2 \times 0.5 \times 0.5$ mm volume of water surrounded by a pick up coil connected to a matching circuit. The quality factor of the complete circuit was ~ 20. The output passed through a low-noise current pre-amplifier (SRS 560) and digitized by a 2 MHz DAQ (NI-6361). The feedback microfluidic loop was also prepolarized but entirely separate from the main sensing loop. The time dependent signal was subsequently Fourier transformed and fit with a Gaussian curve to localize the resonance frequency.

The chips placement in the system is shown in figure 4.15(a). At first glance it might seem that a (110) surface polished diamond would make the optical setup simpler and improve the NV fluorescence intensity due to a more favorable polarization/NV axis orientation. However, in this configuration there is a cancellation effect as the NVs are sensitive only to the magnetic field component aligned along the NV axis but the nuclear spins precess in a plane transverse to the magnetic field direction. The analyte can be thought of as a large homogeneously magnetized volume. The field felt by an NV center located a point $\vec{r_0}$ and with an NV axis along the aligned in the (110) plane (here assumed to be the x axis without loss of generality), located at depth h below the surface, due to a magnetic field

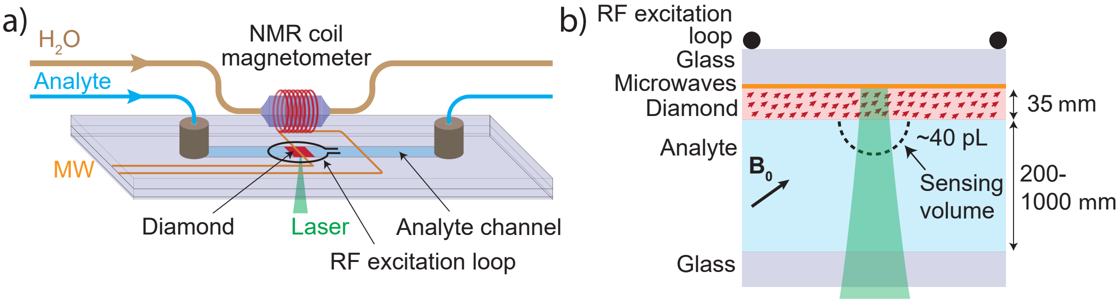

Figure 4.14: The microfluidic assembly. A copper microwave trace is deposited on a microscope slide on top of which a 35 μm thick diamond membrane with a homogeneous distribution of NV centers if glued. A 2 mm wide rectangular channel was milled in another microscope glass slide to form the channel that was capped off by a 150 μm thick coverslip placed on top of the channel. A volume of water surrounded by a conventional NMR pick up coil was placed near the diamond chip and used as a feedback signal source for the Helmholtz coil currrent source. The optical path went through the analyte as in this case the diamond sensor could be placed directly above the microwave stripline increasing both the Rabi frequency, MW field homogeneity and fluorescence intensity as the microwave stripline reflected both the excitation and fluorescence light.

oscillating in the transverse plane at phase ϕ of its precession is equal to:

$$\begin{aligned} B_{\text{eff}} &\sim \int_{-\infty}^{\infty} dx \int_{-\infty}^{\infty} dy \int_{0}^{\infty} \left(\frac{3\mathbf{r}(\mathbf{m}\cdot\mathbf{r})}{r^5} - \frac{\mathbf{m}}{r^3} \right) dz \\ &= \int_{-\infty}^{\infty} dx \int_{-\infty}^{\infty} dy \int_{0}^{\infty} dz \frac{3xy\cos(\phi)}{(x^2+y^2+(h+z)^2)^{5/2}} + \\ &+ \frac{3hy\sin(\phi)}{(x^2+y^2+(h+z)^2)^{5/2}} + \frac{3yz\sin(\phi)}{(x^2+y^2+(h+z)^2)^{5/2}}. \end{aligned} \tag{4.34}$$

Notice that all terms contain either x or y or both which are asymmetric while the integration limits are symmetric meaning that the final value of the integral is 0. The argument for a (111) polished diamond follows a similar logic. There is no total cancellation in the case of a (100) polished diamond which is why it was used in this experiment. Additionally between the Helmholtz coils and the microfluidic chip a pair of magnetic linear and second-order order gradient shims driven by a commercial Instek GPD-4303S power supply. The spacing between the shim planes was 8 cm and were formed by 24 AWG enameled wire capable of producing gradient compensation field of $1.2 - 1.6$ μT/mm/A for the linear shims and $0.05 - 0.1\mu$T/mm/A for the second-order shims. Shimming was done in two steps: first the linear shim values were adjusted against the coil NMR magnetometer. The stand-off distance between the NMR coil magnetometer and

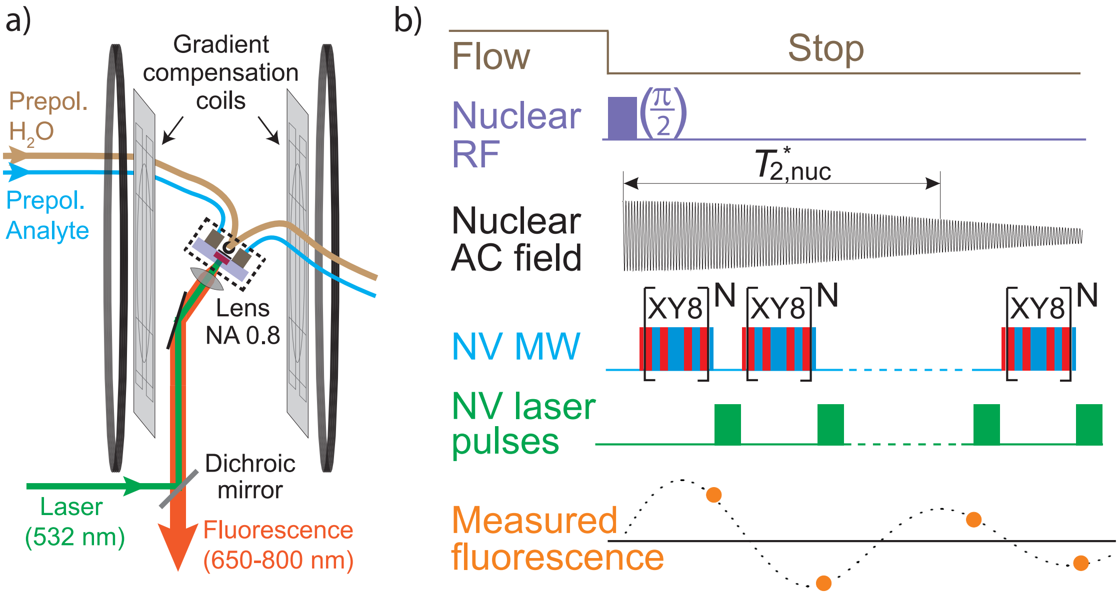

Figure 4.15: a) Placement of the microfluidic chip in the experimental apparatus. The chip has to be tilted in order to align the NV axis with the external field. A aspheric NA= 0.8 aperture lens was used to both deliver the excitation laser light and collect the NV fluorescence. Between the Helmholtz coils and the chip were placed a pair linear and second order gradient shims. b) A diagram showing all the relevant pulse timings. Before each NMR readout the flow is stopped. Then a RF $\pi/2$ pulse is applied and the nuclei start precessing. The decay envelope determined by the T_2^* time which is usually limite by the

the NV sensing volume was about 3 mm so the fine-tuning of the shim values was done on a water NV NMR signal this was done iteratively by first adjusting the linear shims, then the second orders and then moving back to linear and so forth until the width of the water signal had plateaued for all available shim channels.

An additional set of coils were glued to the Helmholtz coil body driven by a Thorlabs LDC 4005 low noise current source. The current was controlled by an analog signal from the same DAQ that was used for the NMR coil magnetometer readout with a signal amplitude proportional to the deviation of the observed NMR signal frequency from a setpoint value. After the integration of an ultra-low noise HighFinesse UCS 10/40 current supply the for driving the Helmholtz coils the NMR spectrometer was relegated to a monitoring function rather than active feedback. If the deviation from setpoint registered by the NMR coil magnetometer exceeded 0.6 Hz the measurement was rejected (see Fig. 4.16).

The relevant timings of the experiment are shown in figure 4.15. First, the flow is stopped, next a resonant RF $\pi/2$ pulse tilts the nuclear spins and they start precessing. After a 50 ms delay, in order to avoid ringdown and microphonics effects, a series of XY8-N measurements are performed and the fluorescence level

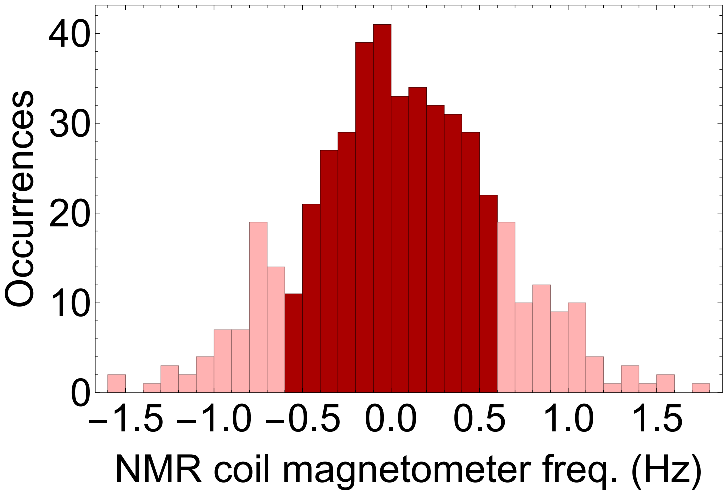

Figure 4.16: Histogram of observed coil magnetometer NMR values in a typical NMR. The measurements falling into the region shaded in darker red were averaged together while all other values were rejected.

for each readout is logged. While the same measurement could also be performed in a continuous flow regime this would result in larger signal broadening due to spatial field gradients as the flowing spins sample the field from a larger area.

To summarize, the key ideas behind the experiment are:

- Measure thermal polarization instead of statistical to avoid the diffusion limit of spectral resolution.
- Polarize spins at a high field and quickly shuttle them to a sensor location. This simultaneously ensures a relatively high polarization and optimum sensing conditions.
- Temporal stability and spatial gradient minimization are key to achieve narrow NV NMR signals.

4.4.3 Results

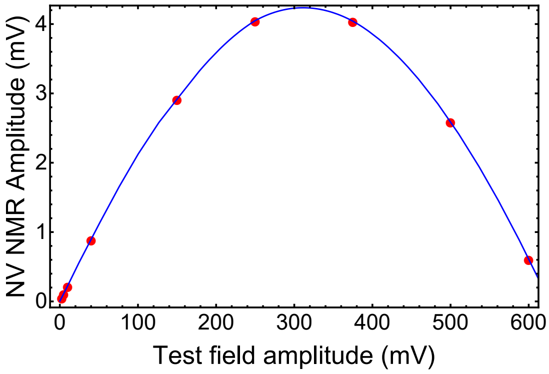

Figure 4.17: Testfield signal strength as a function of generator voltage.

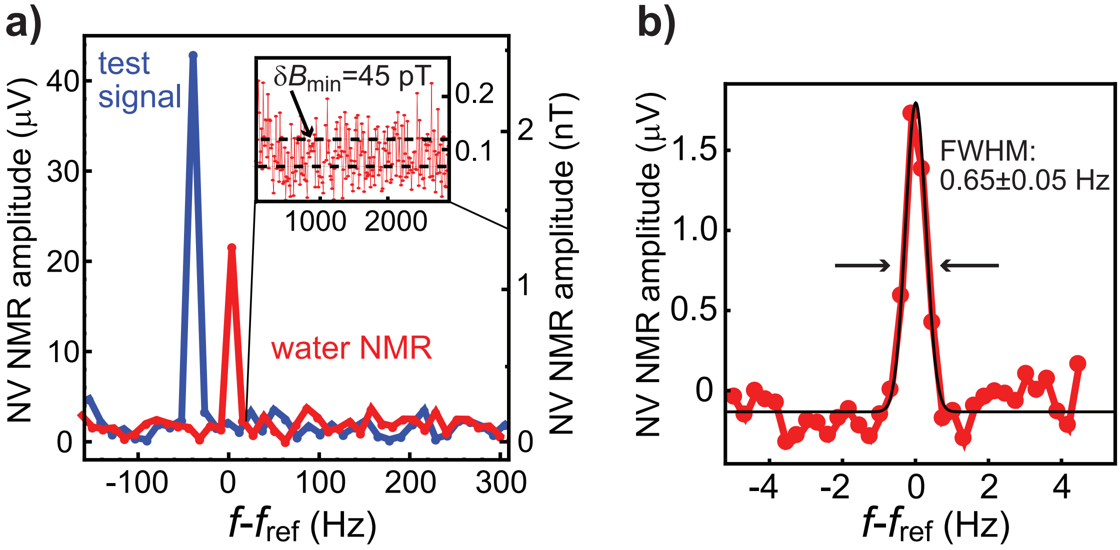

Figure 4.18: NMR water spectra for setup characterization. Sensitivity estimation with a water NV NMR signal versus a calibration field of a known amplitude (a). Spectral resolution limit of a NV water signal.

The spectral resolution and sensitivity limits of our device were tested with deionized water. To make an NMR field strength was calibrated against a testfield from a signal generator. The testfield signal was applied through a copper wire placed some distance from the NV center. To obtain a magnetic field/generator voltage dependence the NMR signal amplitude was monitored while the generator voltage was gradually increased. The pulse sequence parameters were chosen such that the the filter faction transmission and the applied testfield frequency was unity. According to equation 4.33 the dependence should be sinusoidal and reach a peak value at $B_{\text{AC}} = \pi\gamma\tau_{tot}/8$. Knowing the total phase accumulation time τ_{tot} from the pulse sequence parameters ($\tau_{tot} = 24.16$ μs) the corresponding magnetic field amplitude is also known and a magnetic field/voltage dependence can be obtained from Fig. 4.17. A calibration magnetic field amplitude of 2.5 nT was set and a detected with the NV NMR spectrometer. This provided a conversion factor between the detected field amplitude in nT and photodetector signal strength in μV. A calibration signal together with a water NMR signal are shown in Fig. 4.18(a) showing that the analyte field amplitude is 1.21 nT. This figure also enables us to deduce the polarization retention after microfluidic shuttling by comparing it to a value obtained from magnetostatic modelling of a water volume polarized at 1.5 T. We conclude that 80% of the equilibrium polarization at 1.5 T is retained. The standard-deviation of points near the signal peak (Fig. 4.18(a) inset) gives a noise estimate with an equivalent magnetic field amplitude of 0.10 nT/$\sqrt{\text{Hz}}$ which corresponds to a concentration sensitivity of 27 M/$\sqrt{\text{Hz}}$ for a SNR of 3:1.

Fig. 4.18(b) shows a high-resolution water NV NMR spectra after the optimizing the magnetic field gradient compensation shims. A Gaussian fit reveals a full width at half maximum of 0.65 ± 0.05 Hz, an order of magnitude improvement when compared to previously reported results [40]. This is still broader than the low-field room-temperature T_2 limit of water [149] of ~ 0.1 Hz. We attribute this to the temporal instability in the bias magnetic field B_0.

To showcase the capabilities of our sensing platform we obtained the NMR spectra of different liquid analytes. Fig. 4.19 show the results for water, trimethylphosphate (TMP) and 1,4-difluorobenzene (DFB). In the time-domain signal of water a decay envelope is visible from which we infer a spin dephasing time of $T_2^* = 0.5$. This is consistent with the sub-hertz FWHM linedwidths observed in the frequency domain. In the TMP signals (Fig. 4.19(b)) beats are observed in the time-domain a characteristic sign of two similar frequency signals being present. The source of this signal is J-couplings between the protons pins and the phosphorus spin. There are two equally probable configurations where the proton is either parallel or anti-parallel to the phosphorous spin resulting. Each configuration has a slightly different energy and thus a slightly different precession frequency resulting in two closely spaced NMR lines split by the heteronuclear J-coupling between the ^{31}P and ^{1}H spins. The observed value of 11.04 ± 0.06 Hz agrees with results obtained from conventional NMR experiments [150]. In the DFB frequency spectra three peaks are observable because each of the protons interacts with two fluorine atoms. As discussed in section 4.1.3 this results in a 1:2:1 intensity distribution of equidistant peaks. The observed splitting between the lines of 6.09 ± 0.05 Hz is consistent with values reported elsewhere [151], [152]. The spectral resolution and SNR of the prepolarization system are both high enough make possible the acquisition of multi-dimensional NMR spectra as well.

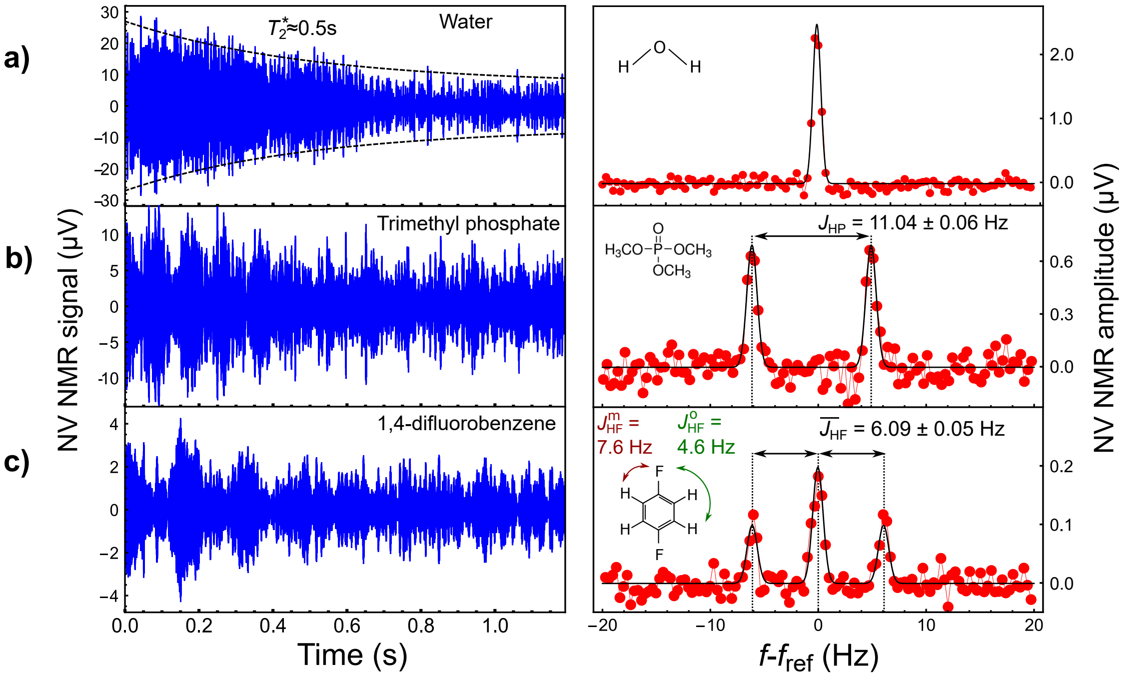

Figure 4.19: Time domain (left column) and frequency domain (right column) NV NMR signals of **(a)** water, **(b)** trimethylphosphate (TMP), and **(c)** 1,4-difluorobenzene (DFB). The signals are averages of ∼ 1000 traces equivalent to a total acquisition time of ∼ 1 h. The time-domain data shown are filtered with a 1 kHz bandpass filter centered around the spectrum center-of-mass for better visualization. Each of the peaks are fit with Gaussian functions to obtained the resonance frequencies. When fitting the TMP data the peak amplitudes are constrained to be equal while for DFB a 1:2:1 amplitude ratio is enforced. We obtain a J-coupling value of $J_{\mathrm{TMP}} = 11.04 \pm 0.06$ Hz for TMP and an average J coupling value between the fluorine and hydrogen spins of $\bar{J}_{\mathrm{HF}} = 6.09 \pm 0.05$ Hz for DFB.

Multidimensional nuclear magnetic resonance spectroscopy

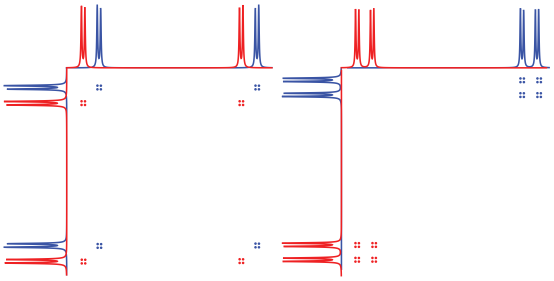

Figure 4.20: The two-dimensional COSY spectrum of cases (b) and (d)

The one dimensional nuclear magnetic resonance spectrum of complex molecules in which many different interactions of different strength are present can be hard to interpret and some peaks cannot be unambiguously assigned. A powerful technique that might lift can lift the ambiguity is multi-dimensional NMR techniques. A simple example of the clarity provided by a two-dimensional pulse sequence over a one dimensional one is provided by Levitt in chapter 16 of "Spin Dynamics"[118] which I will try to concisely reproduce here. Consider a pair of $I = 1/2$ spins in an isotropic liquid such that the dipole-dipole coupling averages out. Then the Hamiltonian is of the form:

$$\hat{H} = \omega_1 \hat{I}_1 + \omega_2 \hat{I}_2 + 2J_{1,2}\hat{I}_1\hat{I}_2, \tag{4.35}$$

where $\omega_{1/2}$ is the Zeeman energy (taking into account the chemical shift of each spin) and $J_{1,2}$ is the isotropic J-coupling strength. The spectrum then consists of two pairs of peaks where the larger splitting (typically) is causes by the chemical shift while the finer structure is caused by the J-coupling. Figure 4.21 demonstrates an assignment problem where two different pairs of coupled $I = 1/2$ spins with similar J-couplings but different chemical shifts are present in the analyte. Model experimental data are shown in subfigure (a) can be described by any of the configurations shown in subfigures (b-d) and the assignment of which peak corresponds to what spin species.

One way to solve the assignment problem was developed by Ernst et al. and is called the a correlation spectroscopy (COSY) sequence. It consists of two $\pi/2$ pulses separated by a variable evolution period τ_1. Following the second $\pi/2$ pulse the spin generated precessing magnetic field is recorded as function of time τ_2. A series of measurements varying the τ_1 time are performed to build up a 2D data array. During the first part of the pulse sequence the spin-spin coupling causes the spins to accumulate additional phase due to the J coupling. This affects the tilt effect of the last $\pi/2$ which in turn affects the observed NMR field amplitude during the last phase of the evolution τ_2. If a 2D Fourier transform is applied to the accumulated data-set crosspeaks appear between spin species that are coupled. Fig. 4.20 shows the color-coded COSY spectra for scenarios (b) and (d). The structure is clearly different removing the ambiguity present in the 1D spectra and illustrating the power of multidimensional NMR sequences.

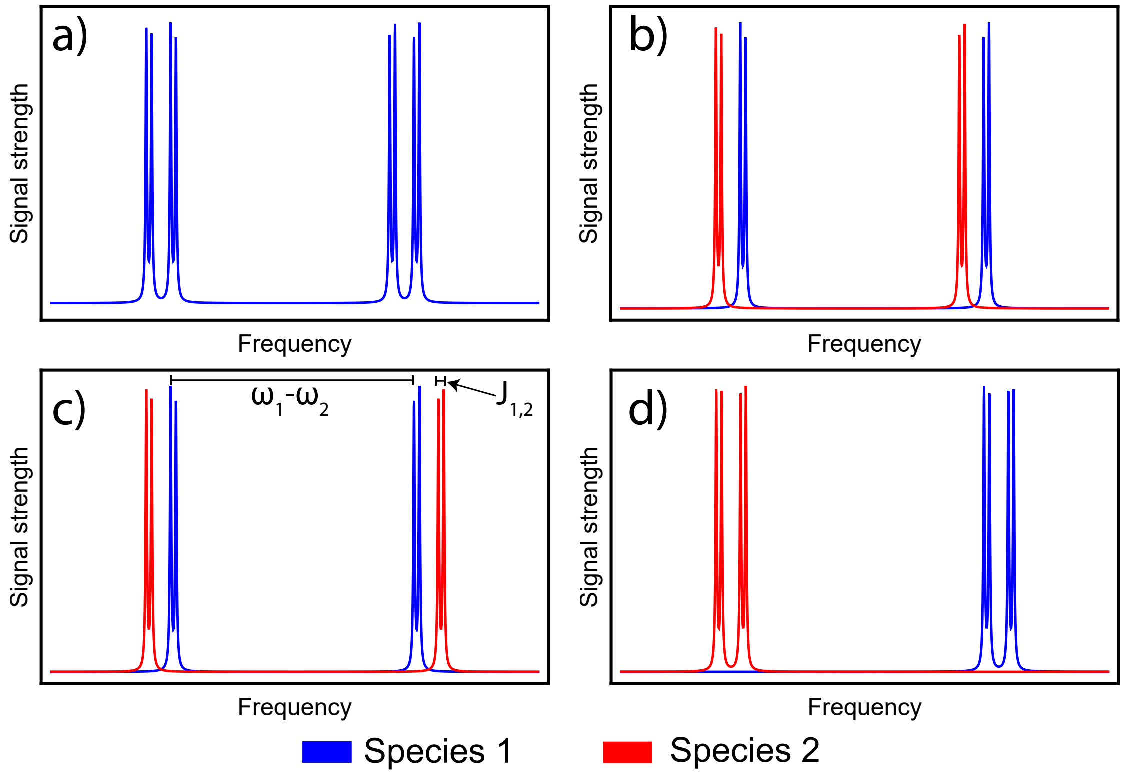

Figure 4.21: Simulated 1D NMR spectra demonstrating identification ambiguity. Subfigure (a) shows a theoretical NMR spectra observed in the experiment of an analyte that holds two pairs of coupled spins. Subfigures (b-d) show three different possible groupings of the peaks that, when added together, could result in the spectrum shown in subfigure (a).

Two dimensional NV NMR spectroscopy

We performed two hetero-nuclear variations of the COSY experiment on 1,4-difluorobenzene. Fig.4.22 shows two different pulse sequences, theoretical predictions of the expected spectra (obtained using a density matrix propagation approach in the Matlab package SPINACH [153]) and the corresponding experimental spectra. In the homonuclear case three diagonal peaks separated by 6.1 Hz are observed and no cross-peaks are present. This is expected as the proton couplings in a strong coupling regime where the J coupling is comparable to the different in Larmor frequencies of the two spins. In the second experiment, the second $\pi/2$ pulse is resonant with the ^{19}F spins (blue pule inf Fig. 4.22(D)). Traditionally in heteronuclear COSY spectrum $\pi/2$ pulses are applied to both species at both instances showing correlations between the hetero-nuclei as well (see Robinson et al. [151]). Due to the limited bandwidth of our experiment this might have resulted in spectral fold-over making the interpretation of the spectra difficult. The variation depicted here results in correlations between the same spin species (these are effectively proton couplings mediated by J-couplings with fluorine). The pulse sequence is tuned to be resonant with protons rendering them insensitive to magnetic fields generated by precessing fluorine spins. The presence of cross peaks split by $\sim$ 6 Hz indicates that the ^{19}F mediates the transfer of magnetization between among the J-split proton states. The spectra are similar to those done by Robinson et al. at Earths field using an inductive aparatus [151].

4.4.4 Limitations and promise of thermal NV NMR

The microfluidic NV NMR spectrometer with spatially decoupled polarization and detection steps demonstrated sub-hertz spectral resolution - enough to resolve single or even double bond J-couplings in a multitude of chemical species. The effective sensing volume is estimated by magnetostatic modelling (see SI of [129]) to be $\sim$ 40 pL outperforming solenoidal sensors. Finally, the sensitivity achieved by the microfluidic platform allowed us to perform a two-dimensional NMR experiment, the first of its kind performed by NV sensors on an external analyte. Additionally, microfluidic systems are already widely used and well integrated in NMR spectrometers (or compound devices consisting of HPLC/mass-spectrometers/optical spectrometers and NMR spectrometers collectively referred to as hyphenated techniques) facilitating the use of diamond quantum sensors in small-sensing-volume research areas such as single-cell metabolomics and mass-limited pharmacodynamics. The epifluorescence imaging format also lends itself well to measurement multiplexing which could enable high-throughput chemical analysis or NMR imaging of cell-cultures while still still retaining single-cell resolution.

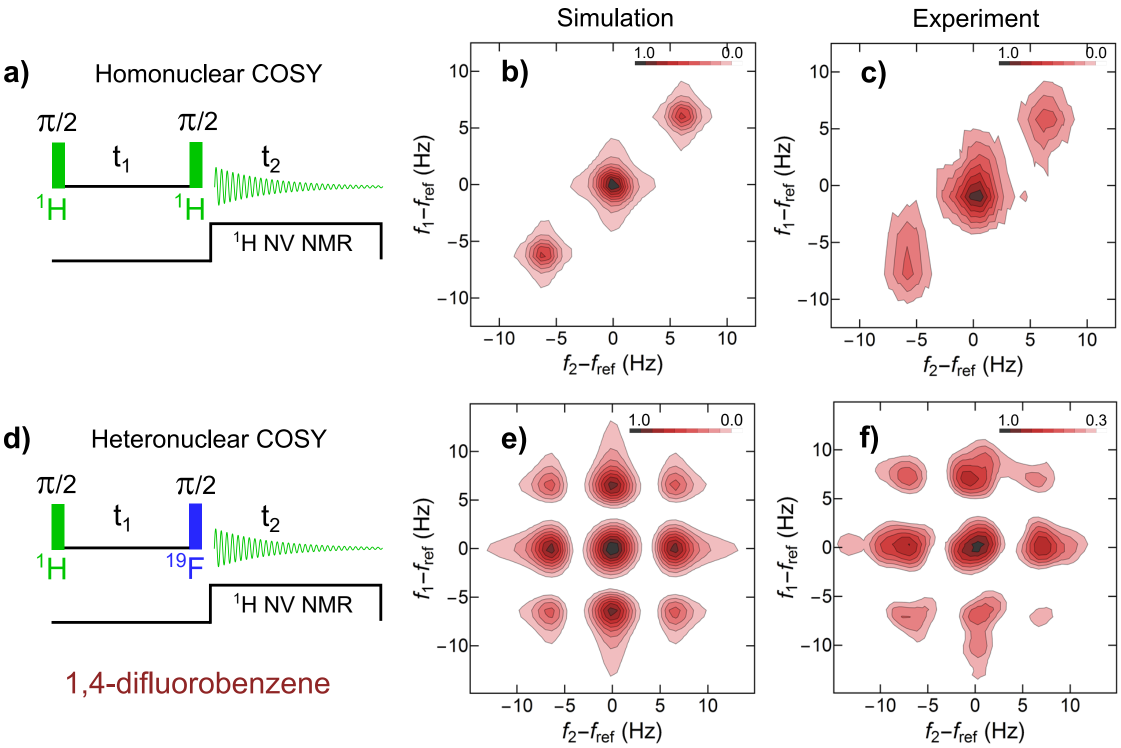

Figure 4.22: (A) Homonuclear COSY pulse sequence. (B) simulated spectrum. (C) Experimental NV NMR spectrum. (D) Modified heteronuclear COSY sequence which shows off-diagonal peaks in both the simulation (E) and experiment (F).

Despite the important progress represented by these results several key problems of the technique should still should still be addressed. First, an obvious flaw in the setup is the requirement for large amounts of analyte. Even-though the sensing volume is only $\sim 40pL$ a much larger volume is necessary to fill the overall flow aparatus (rest of the chip volume, tubing etc). A solution to this could be the use smaller microfluidic channels and/or microdroplet propulsion by helium through large systems which would significantly limit the amount of analyte necessary.

A more difficult challenge is the sensitivity which, despite the improvements netted by the microfluidic design, is still orders of magnitude away from what would be necessary to detect physiological quantities of analyte (typically in the micro- to millimolar range). Up to an order-of-magnitude increase in sensitivity could be achieved by increasing the field at which NMR is detected. As an added benefit this would enable the use of higher order $XY8-N$, as the nuclear spin Larmor precession frequency would be higher, leading to better decoupling, higher T_2 times and better acquisition duty cycles. Another order-of-magnitude could be achieved by significantly increasing the prepolarization field by using high-strength superconducting magnets. The largest increase in SNR could prospectively come from NV hyperpolarization where the near-unity NV polarization could be transferred to the analyte spins. This has already been successfully demonstrated for

^{13}C spins within the diamond [80], [112], [154] and polarization transfer using Hartmann-Hahn double resonance has been demonstrated for single NV centers [155], but ensemble transfer to an external analyte is yet to be demonstrated.

Chapter 5

Summary and outlook

The NV center in diamond has exceptional sensing capabilities and research in the field has been actively pursued by a large number of research groups worldwide. New detection modalities and performance improvements in terms of scale, sensitivity, and resolution sometimes spanning orders-of-magnitude are being published with a high frequency indicative of the potential of the platform. Additionally the fields in which the NV sensor is already being used as a sensor has also expanded considerably in the last few years ranging from biology, to geology, to electronics and material science. There are a large amount of tunable parameters and a wide array of experiment design approaches that affect the sensor performance and must be tailored to the particular problem under investigation. This work explored both parameter and design spaces of NV sensors.

In the parameter space the implantation dose/NV$^-$ concentration impact on the coherence properties of the ensemble sensor was studied. A series of spots on the same diamond chip were irradiated with an electron beam varying the electron dose. By using the same diamond chip we control for any variations in experimental results due to parameters intrinsic to the diamond. Magnetic field-dependent T_1 relaxation measurements were performed and revealed several features. First, at zero field a resonance in the relaxation rate was observed which we attributed to an opening of an additional relaxation channel through neighbouring NV centers not aligned along the NV center as at zero field all spatial NV subgroups are energy matched. Second, with increased concentration the effective T_1 relaxation time increased. The rate of increase was a linear function of concentration as is the average dipole-dipole interaction strength. We thus concluded that the dominant relaxation mechanism at high NV center concentrations in such a sample are couplings to other NV centers. Third, with increasing NV concentration the stretchedness parameter β of the fit function $e^{-(t/T_1)^\beta}$ moved further away from unity. We explain this by noting that not-only does the average dipole-dipole interaction strength increase but the distribution of interactions strengths also becomes broader. A perplexing aspect of the experimental results is how small the central resonance peak is for all the datasets. If pure dipole-dipole interactions where the governing relaxation mechanism the addition of 3 times as many relaxation partners should result in a a larger effect. A possible explanation for this could be hidden in an additional effect that is introduced with larger dosses of vacancy-generating particles which is lattice damage. Previous work by [88] observed significant line-broadening and ODMR frequency shift at high electron-implantation doses which they also attributed to lattice damage. In a future experiment should be complimented with a birefringence imaging experiment. The strength of the of birefringence is correlated to the amount of lattice damage present in the crystal [156]. If high strain is also strongly correlated with high relaxation rates additional steps could be taken to decouple the two quantities such as annealing at higher temperatures or performing experiments with low nitrogen-content diamond.

A study of experimental design parameter was a significant part of the magnetic imaging experiment described in chapter 3. The initial concept of the experiment envisioned probing the magnetic field distribution during the locomotion dynamics of magnetic microswimmers using an NV based magnetic epifluorescence microscope. During the following months the scope of the research was significantly narrowed with the final published results examining the properties of chains of magnetic particles (that form the microswimmer body) in a dry setting. This was the first such setup built in the University of Latvia Laser center and during the process several important lessons were learned that have since been implemented in the following iterations of imaging experiments. One such experiment, where the author made a minor contribution, observed para and superparamagnetism in hemozoin crystals - a digestion byproduct of the malaria-causing Plasmodium parasite and a substance targeted by anti-malarial drugs. This was performed on an aparatus with a per-pixel sensitivity of 8.4μT Hz$^{-1/2}$, an order of magnitude increase compared to the first attempt. This sensitivity could enable us to revisit the experiment where the swimming dynamics of microfluidic swimmers are observed. A key challenge would be to constrain the z-component of the microswimmers translation as the magnetic dipole signal falls rapidly with stand-off distance. This could be done by embedding the sensor in a narrow microfluidic channel, etching the channels in the diamond itself.

The last chapter discussed nuclear magnetic resonance spectroscopy with NV centers where both the diamond engineering and experimental design had to be finely tuned to observe the faint magnetic fields produced by nuclear spins. The first experiment relied on the fact that very shallow NV centers are much more strongly coupled to nuclear spins near the diamond surfaces than those further away. For this reason the effective sensing volume of an NV center is defined by the depth below the surface and very shallow defects have exceedingly small sensing volumes. In this regime the polarization due to stochastic flips in the nuclear spin population is significant and high signal-to-noise ratio can be achieved. A significant drawback of the method was the limited spectral resolution (~ 1 kHz) due to spin diffusion away from the sensing volume. This prompted a pivot to sensing of thermal polarization (thermal equilibrium polarization due to small difference in energy from the Zeeman effect) where diffusion is not an issue. To combat the intrinsically lower signal strengths than when detecting statistical fields the detection and polarization phases were spatially separated by using a microfluidic system. The sensor was able to achieve sub-hertz spectral resolution in a ~ 40 pL sensing volume and a concentration sensitivity of 27 $\mathrm{M}/\sqrt{\mathrm{Hz}}$ - an order of magnitude increase when compared to previously reported results in such a system. This, however, is still insufficient to detect typical concentrations of biologically interesting molecules such as metabolites which are typically present in the micro- to millimolar quantities.

While there are design and engineering steps that could result in an SNR increase of an additional order of magnitude the most potent and most interesting approach is the transfer of polarization from the NV center to the target spins. This could lead to signal strength increases of several orders of magnitude and has already been demonstrated for certain nuclei inside the diamond itself. Despite the conceptual simplicity of the idea direct detection of polarization transfer to external analytes has proved elusive. Many strategies have been proposed and studied relying on energy-crossing, double resonance techniques and ancilla mediated transfer. What complicates the study of this process is a lack of baseline signal that could be monitored for minor improvements in signal strength that could then be further iterated upon. The thermal nuclear NV NMR signal could be used as such a baseline to facilitate the study of hyperpolarization techniques.

5.1 Theses

- In the high nitrogen/NV concentration regime ([N]> 50 ppm) the longitudinal relaxation rate exhibits linear scaling with radiation dose supporting the idea that NV-NV dipolar couplings are the dominant longitudinal relaxation mechanism in diamond.
    - Some ambiguity of the role of lattice damage, introduced by the implantation process, in the worsening of the relaxation time still remains as the magnetic-field dependent relaxation rates do not perfectly agree with a relaxation process mediated purely by NV-NV dipolar interactions.
- A systematic optimization of the diamond/setup/control parameter space of a diamond magnetic microscope can net a sensitivity as low as 8.4 μT $\mathrm{Hz}^{-1/2}$ potentially enabling the monitoring of time-dependent processes such as locomotion of magnetic microswimmers.
- An NV NMR spectrometer embedded in a microfluidic platform with spatially decoupled polarisation and detection phases exhibited a molar sensitivity of 27 M $\mathrm{Hz}^{-1/2}$ in a 40 pL effective sensing volume with a spectral resolution of 0.65 Hz—performance metrics good enough to enable multi-dimensional NMR measurements on an external analyte.
    - The microfluidic NV platform could be a launchpad for polarization transfer studies in NVs providing a high enough baseline signal for rapid iteration over the experimental parameter space (external field, transfer mechanism, analyte).

References

[1] A. Acín, I. Bloch, H. Buhrman, T. Calarco, C. Eichler, J. Eisert, D. Esteve, N. Gisin, S. J. Glaser, F. Jelezko, S. Kuhr, M. Lewenstein, M. F. Riedel, P. O. Schmidt, R. Thew, A. Wallraff, I. Walmsley, and F. K. Wilhelm, "The quantum technologies roadmap: A European community view", *New Journal of Physics*, vol. 20, no. 8, p. 080 201, Aug. 2018, ISSN: 1367-2630. DOI: `10.1088/1367-2630/aad1ea`.

[2] "Quantum leaps - Subatomic opportunities", *The Economist*, Mar. 2017, ISSN: 0013-0613.

[3] C. L. Degen, F. Reinhard, and P. Cappellaro, "Quantum sensing", *Reviews of Modern Physics*, vol. 89, no. 3, p. 035 002, Jul. 2017. DOI: `10.1103/RevModPhys.89.035002`.

[4] R. LaRose, "Overview and Comparison of Gate Level Quantum Software Platforms", *arXiv:1807.02500 [quant-ph]*, Jul. 2018.

[5] G. Balasubramanian, P. Neumann, D. Twitchen, M. Markham, R. Kolesov, N. Mizuochi, J. Isoya, J. Achard, J. Beck, J. Tissler, V. Jacques, P. R. Hemmer, F. Jelezko, and J. Wrachtrup, "Ultralong spin coherence time in isotopically engineered diamond", en, *Nature Materials*, vol. 8, no. 5, pp. 383–387, May 2009, ISSN: 1476-4660. DOI: `10.1038/nmat2420`.

[6] N. Bar-Gill, L. M. Pham, A. Jarmola, D. Budker, and R. L. Walsworth, "Solid-state electronic spin coherence time approaching one second", en, *Nature Communications*, vol. 4, p. 1743, Apr. 2013, ISSN: 2041-1723. DOI: `10.1038/ncomms2771`.

[7] P. Kehayias, A. Jarmola, N. Mosavian, I. Fescenko, F. M. Benito, A. Laraoui, J. Smits, L. Bougas, D. Budker, A. Neumann, S. R. J. Brueck, and V. M. Acosta, "Solution nuclear magnetic resonance spectroscopy on a nanostructured diamond chip", En, *Nature Communications*, vol. 8, no. 1, p. 188, Aug. 2017, ISSN: 2041-1723. DOI: `10.1038/s41467-017-00266-4`.

[8] D. J. McCloskey, N. Dontschuk, D. A. Broadway, A. Nadarajah, A. Stacey, J.-P. Tetienne, L. C. L. Hollenberg, S. Prawer, and D. A. Simpson, "Enhanced widefield quantum sensing with nitrogen-vacancy ensembles using diamond nanopillar arrays", *arXiv:1902.02464 [cond-mat, physics:physics]*, Feb. 2019.

[9] D. Le Sage, K. Arai, D. R. Glenn, S. J. DeVience, L. M. Pham, L. Rahn-Lee, M. D. Lukin, A. Yacoby, A. Komeili, and R. L. Walsworth, "Optical magnetic imaging of living cells", en, *Nature*, vol. 496, no. 7446, pp. 486–489, Apr. 2013, ISSN: 1476-4687. DOI: `10.1038/nature12072`.

[10] D. R. Glenn, K. Lee, H. Park, R. Weissleder, A. Yacoby, M. D. Lukin, H. Lee, R. L. Walsworth, and C. B. Connolly, "Single cell magnetic imaging using a quantum diamond microscope", *Nature methods*, vol. 12, no. 8, pp. 736–738, Aug. 2015, ISSN: 1548-7091. DOI: `10.1038/nmeth.3449`.

[11] T. R. Anthony and W. F. Banholzer, "Properties of diamond with varying isotopic composition", *Diamond and Related Materials*, Proceedings of the Second European Conference on Diamond, Diamond-like and Related Coatings, vol. 1, no. 5, pp. 717–726, Apr. 1992, ISSN: 0925-9635. DOI: `10.1016/0925-9635(92)90197-V`.

[12] A. Jarmola, Z. Bodrog, P. Kehayias, M. Markham, J. Hall, D. J. Twitchen, V. M. Acosta, A. Gali, and D. Budker, "Optically detected magnetic resonances of nitrogen-vacancy ensembles in 13c-enriched diamond", *Physical Review B*, vol. 94, no. 9, p. 094 108, Sep. 2016. DOI: `10.1103/PhysRevB.94.094108`.

[13] E. Bauch, S. Singh, J. Lee, C. A. Hart, J. M. Schloss, M. J. Turner, J. F. Barry, L. Pham, N. Bar-Gill, S. F. Yelin, and R. L. Walsworth, "Decoherence of dipolar spin ensembles in diamond", *arXiv:1904.08763 [physics, physics:quant-ph]*, Apr. 2019.

[14] D. Farfurnik, N. Alfasi, S. Masis, Y. Kauffmann, E. Farchi, Y. Romach, Y. Hovav, E. Buks, and N. Bar-Gill, "Enhanced concentrations of nitrogen-vacancy centers in diamond through TEM irradiation", *Applied Physics Letters*, vol. 111, no. 12, p. 123 101, Sep. 2017, ISSN: 0003-6951. DOI: `10.1063/1.4993257`.

[15] Y.-C. Chen, P. S. Salter, S. Knauer, L. Weng, A. C. Frangeskou, C. J. Stephen, S. N. Ishmael, P. R. Dolan, S. Johnson, B. L. Green, G. W. Morley, M. E. Newton, J. G. Rarity, M. J. Booth, and J. M. Smith, "Laser writing of coherent colour centres in diamond", *Nature Photonics*, vol. 11, p. 77, Dec. 2016.

[16] C. Santori, P. E. Barclay, K.-M. C. Fu, and R. G. Beausoleil, "Vertical distribution of nitrogen-vacancy centers in diamond formed by ion implantation and annealing", *Physical Review B*, vol. 79, no. 12, p. 125 313, Mar. 2009. DOI: `10.1103/PhysRevB.79.125313`.

[17] J. F. Barry, M. J. Turner, J. M. Schloss, D. R. Glenn, Y. Song, M. D. Lukin, H. Park, and R. L. Walsworth, "Optical magnetic detection of single-neuron action potentials using quantum defects in diamond", en, *Proceedings of the National Academy of Sciences*, vol. 113, no. 49, pp. 14 133–14 138, Dec. 2016, ISSN: 0027-8424, 1091-6490. DOI: `10.1073/pnas.1601513113`.

[18] P. Balasubramanian, C. Osterkamp, Y. Chen, X. Chen, T. Teraji, E. Wu, B. Naydenov, and F. Jelezko, "Dc Magnetometry with Engineered Nitrogen-Vacancy Spin Ensembles in Diamond", *Nano Letters*, Aug. 2019, ISSN: 1530-6984. DOI: `10.1021/acs.nanolett.9b02993`.

[19] M. V. Hauf, P. Simon, N. Aslam, M. Pfender, P. Neumann, S. Pezzagna, J. Meijer, J. Wrachtrup, M. Stutzmann, F. Reinhard, and J. A. Garrido, "Addressing Single Nitrogen-Vacancy Centers in Diamond with Transparent in-Plane Gate Structures", *Nano Letters*, vol. 14, no. 5, pp. 2359–2364, May 2014, ISSN: 1530-6984. DOI: `10.1021/nl4047619`.

[20] B. Grotz, M. V. Hauf, M. Dankerl, B. Naydenov, S. Pezzagna, J. Meijer, F. Jelezko, J. Wrachtrup, M. Stutzmann, F. Reinhard, and J. A. Garrido, "Charge state manipulation of qubits in diamond", en, *Nature Communications*, vol. 3, p. 729, Mar. 2012, ISSN: 2041-1723. DOI: `10.1038/ncomms1729`.

[21] Y. Mita, "Change of absorption spectra in type-Ib diamond with heavy neutron irradiation", *Physical Review B*, vol. 53, no. 17, pp. 11 360–11 364, May 1996. DOI: `10.1103/PhysRevB.53.11360`.

[22] M. W. Doherty, N. B. Manson, P. Delaney, F. Jelezko, J. Wrachtrup, and L. C. L. Hollenberg, "The nitrogen-vacancy colour centre in diamond", *Physics Reports*, The nitrogen-vacancy colour centre in diamond, vol. 528, no. 1, pp. 1–45, Jul. 2013, ISSN: 0370-1573. DOI: `10.1016/j.physrep.2013.02.001`.

[23] J. H. N. Loubser and J. A. v. Wyk, "Electron spin resonance in the study of diamond", *Reports on Progress in Physics*, vol. 41, no. 8, pp. 1201–1248, Aug. 1978, ISSN: 0034-4885. DOI: `10.1088/0034-4885/41/8/002`.

[24] J. Loubser and J. Van Wyk, "Optical spin-polarisation in a triplet state in irradiated and annealed type 1b diamonds", *Diamond Research*, pp. 11–14, 1977.

[25] L. M. Pham, “Magnetic Field Sensing with Nitrogen-Vacancy Color Centers in Diamond”, en, PhD thesis, Harvard University, May 2013.

[26] R. Hanson, O. Gywat, and D. D. Awschalom, “Room-temperature manipulation and decoherence of a single spin in diamond”, *Physical Review B*, vol. 74, no. 16, p. 161 203, Oct. 2006. DOI: `10.1103/PhysRevB.74.161203`.

[27] A. M. Edmonds, U. F. S. D’Haenens-Johansson, R. J. Cruddace, M. E. Newton, K.-M. C. Fu, C. Santori, R. G. Beausoleil, D. J. Twitchen, and M. L. Markham, “Production of oriented nitrogen-vacancy color centers in synthetic diamond”, *Physical Review B*, vol. 86, no. 3, p. 035 201, Jul. 2012. DOI: `10.1103/PhysRevB.86.035201`.

[28] L. M. Pham, N. Bar-Gill, D. Le Sage, C. Belthangady, A. Stacey, M. Markham, D. J. Twitchen, M. D. Lukin, and R. L. Walsworth, “Enhanced metrology using preferential orientation of nitrogen-vacancy centers in diamond”, *Physical Review B*, vol. 86, no. 12, p. 121 202, Sep. 2012. DOI: `10.1103/PhysRevB.86.121202`.

[29] Y.-C. Chen, B. Griffiths, L. Weng, S. S. Nicley, S. N. Ishmael, Y. Lekhai, S. Johnson, C. J. Stephen, B. L. Green, G. W. Morley, M. E. Newton, M. J. Booth, P. S. Salter, and J. M. Smith, “Laser writing of individual nitrogen-vacancy defects in diamond with near-unity yield”, *Optica*, vol. 6, no. 5, pp. 662–667, May 2019. DOI: `10.1364/OPTICA.6.000662`.

[30] M. V. Hauf, B. Grotz, B. Naydenov, M. Dankerl, S. Pezzagna, J. Meijer, F. Jelezko, J. Wrachtrup, M. Stutzmann, F. Reinhard, and J. A. Garrido, “Chemical control of the charge state of nitrogen-vacancy centers in diamond”, *Physical Review B*, vol. 83, no. 8, p. 081 304, Feb. 2011. DOI: `10.1103/PhysRevB.83.081304`.

[31] K.-M. C. Fu, C. Santori, P. E. Barclay, and R. G. Beausoleil, “Conversion of neutral nitrogen-vacancy centers to negatively charged nitrogen-vacancy centers through selective oxidation”, *Applied Physics Letters*, vol. 96, no. 12, p. 121 907, Mar. 2010, ISSN: 0003-6951. DOI: `10.1063/1.3364135`.

[32] F. P. Bundy, H. T. Hall, H. M. Strong, and R. H. Wentorf, “Man-Made Diamonds”, En, *Nature*, vol. 176, no. 4471, p. 51, Jul. 1955, ISSN: 1476-4687. DOI: `10.1038/176051a0`.

[33] R. S. Balmer, J. R. Brandon, S. L. Clewes, H. K. Dhillon, J. M. Dodson, I. Friel, P. N. Inglis, T. D. Madgwick, M. L. Markham, T. P. Mollart, N. Perkins, G. A. Scarsbrook, D. J. Twitchen, A. J. Whitehead, J. J. Wilman, and S. M. Woollard, “Chemical vapour deposition synthetic diamond: Materials, technology and applications”, en, *Journal of Physics:*

Condensed Matter, vol. 21, no. 36, p. 364 221, Aug. 2009, ISSN: 0953-8984. DOI: `10.1088/0953-8984/21/36/364221`.

[34] D. Choudhary and J. Bellare, “Manufacture of gem quality diamonds: A review”, *Ceramics International*, vol. 26, no. 1, pp. 73–85, Jan. 2000, ISSN: 0272-8842. DOI: `10.1016/S0272-8842(99)00022-X`.

[35] R. C. Burns, V. Cvetkovic, C. N. Dodge, D. J. F. Evans, M.-L. T. Rooney, P. M. Spear, and C. M. Welbourn, “Growth-sector dependence of optical features in large synthetic diamonds”, *Journal of Crystal Growth*, vol. 104, no. 2, pp. 257–279, Jul. 1990, ISSN: 0022-0248. DOI: `10.1016/0022-0248(90)90126-6`.

[36] J. F. Ziegler, M. D. Ziegler, and J. P. Biersack, “SRIM – The stopping and range of ions in matter (2010)”, *Nuclear Instruments and Methods in Physics Research Section B: Beam Interactions with Materials and Atoms*, 19th International Conference on Ion Beam Analysis, vol. 268, no. 11, pp. 1818–1823, Jun. 2010, ISSN: 0168-583X. DOI: `10.1016/j.nimb.2010.02.091`.

[37] E. E. Kleinsasser, M. M. Stanfield, J. K. Q. Banks, Z. Zhu, W.-D. Li, V. M. Acosta, H. Watanabe, K. M. Itoh, and K.-M. C. Fu, “High density nitrogen-vacancy sensing surface created via He+ ion implantation of 12c diamond”, *Applied Physics Letters*, vol. 108, no. 20, p. 202 401, May 2016, ISSN: 0003-6951. DOI: `10.1063/1.4949357`.

[38] K. Ohno, F. Joseph Heremans, L. C. Bassett, B. A. Myers, D. M. Toyli, A. C. Bleszynski Jayich, C. J. Palmstrøm, and D. D. Awschalom, “Engineering shallow spins in diamond with nitrogen delta-doping”, *Applied Physics Letters*, vol. 101, no. 8, p. 082 413, Aug. 2012, ISSN: 0003-6951. DOI: `10.1063/1.4748280`.

[39] C. Osterkamp, J. Lang, J. Scharpf, C. Müller, L. P. McGuinness, T. Diemant, R. J. Behm, B. Naydenov, and F. Jelezko, “Stabilizing shallow color centers in diamond created by nitrogen delta-doping using SF6 plasma treatment”, *Applied Physics Letters*, vol. 106, no. 11, p. 113 109, Mar. 2015, ISSN: 0003-6951. DOI: `10.1063/1.4915305`.

[40] D. R. Glenn, D. B. Bucher, J. Lee, M. D. Lukin, H. Park, and R. L. Walsworth, “High-resolution magnetic resonance spectroscopy using a solid-state spin sensor”, en, *Nature*, vol. 555, no. 7696, pp. 351–354, Mar. 2018, ISSN: 1476-4687. DOI: `10.1038/nature25781`.

[41] M. Gould, R. J. Barbour, N. Thomas, H. Arami, K. M. Krishnan, and K.-M. C. Fu, “Room-temperature detection of a single 19 nm super-paramagnetic nanoparticle with an imaging magnetometer”, *Applied Physics Letters*, vol. 105, no. 7, p. 072 406, Aug. 2014, ISSN: 0003-6951. DOI: `10.1063/1.4893602`.

[42] K. Ohashi, T. Rosskopf, H. Watanabe, M. Loretz, Y. Tao, R. Hauert, S. Tomizawa, T. Ishikawa, J. Ishi-Hayase, S. Shikata, C. L. Degen, and K. M. Itoh, “Negatively Charged Nitrogen-Vacancy Centers in a 5 nm Thin 12c Diamond Film”, *Nano Letters*, vol. 13, no. 10, pp. 4733–4738, Oct. 2013, ISSN: 1530-6984. DOI: `10.1021/nl402286v`.

[43] J. R. Maze, A. Gali, E. Togan, Y. Chu, A. Trifonov, E. Kaxiras, and M. D. Lukin, “Properties of nitrogen-vacancy centers in diamond: The group theoretic approach”, en, *New Journal of Physics*, vol. 13, no. 2, p. 025 025, Feb. 2011, ISSN: 1367-2630. DOI: `10.1088/1367-2630/13/2/025025`.

[44] L. J. Rogers, S. Armstrong, M. J. Sellars, and N. B. Manson, “Infrared emission of the NV centre in diamond: Zeeman and uniaxial stress studies”, en, *New Journal of Physics*, vol. 10, no. 10, p. 103 024, Oct. 2008, ISSN: 1367-2630. DOI: `10.1088/1367-2630/10/10/103024`.

[45] Davies G., Hamer M. F., and Price William Charles, “Optical studies of the 1.945 eV vibronic band in diamond”, *Proceedings of the Royal Society of London. A. Mathematical and Physical Sciences*, vol. 348, no. 1653, pp. 285–298, Feb. 1976. DOI: `10.1098/rspa.1976.0039`.

[46] A. M. Stoneham, *Theory of Defects in Solids: Electronic Structure of Defects in Insulators and Semiconductors*, en. Clarendon Press, 2001, ISBN: 978-0-19-850780-2.

[47] V. M. Acosta, E. Bauch, M. P. Ledbetter, A. Waxman, L.-S. Bouchard, and D. Budker, “Temperature Dependence of the Nitrogen-Vacancy Magnetic Resonance in Diamond”, *Physical Review Letters*, vol. 104, no. 7, p. 070 801, Feb. 2010. DOI: `10.1103/PhysRevLett.104.070801`.

[48] S. Felton, A. M. Edmonds, M. E. Newton, P. M. Martineau, D. Fisher, D. J. Twitchen, and J. M. Baker, “Hyperfine interaction in the ground state of the negatively charged nitrogen vacancy center in diamond”, *Physical Review B*, vol. 79, no. 7, p. 075 203, Feb. 2009. DOI: `10.1103/PhysRevB.79.075203`.

[49] N. B. Manson, J. P. Harrison, and M. J. Sellars, “Nitrogen-vacancy center in diamond: Model of the electronic structure and associated dynamics”, *Physical Review B*, vol. 74, no. 10, p. 104 303, Sep. 2006. DOI: `10.1103/PhysRevB.74.104303`.

[50] L. Robledo, H. Bernien, I. van Weperen, and R. Hanson, "Control and Coherence of the Optical Transition of Single Nitrogen Vacancy Centers in Diamond", *Physical Review Letters*, vol. 105, no. 17, p. 177 403, Oct. 2010. DOI: `10.1103/PhysRevLett.105.177403`.

[51] L. Robledo, H. Bernien, T. v. d. Sar, and R. Hanson, "Spin dynamics in the optical cycle of single nitrogen-vacancy centres in diamond", en, *New Journal of Physics*, vol. 13, no. 2, p. 025 013, Feb. 2011, ISSN: 1367-2630. DOI: `10.1088/1367-2630/13/2/025013`.

[52] J. M. Schloss, J. F. Barry, M. J. Turner, and R. L. Walsworth, "Simultaneous Broadband Vector Magnetometry Using Solid-State Spins", *Physical Review Applied*, vol. 10, no. 3, p. 034 044, Sep. 2018. DOI: `10.1103/PhysRevApplied.10.034044`.

[53] R. R. Ernst, G. Bodenhausen, and A. Wokaun, *Principles of Nuclear Magnetic Resonance in One and Two Dimensions (International Series of Monographs on Chemistry)*. Clarendon Press, 1990, ISBN: 0-19-855647-0.

[54] A. Jarmola, V. M. Acosta, K. Jensen, S. Chemerisov, and D. Budker, "Temperature- and Magnetic-Field-Dependent Longitudinal Spin Relaxation in Nitrogen-Vacancy Ensembles in Diamond", *Physical Review Letters*, vol. 108, no. 19, p. 197 601, May 2012. DOI: `10.1103/PhysRevLett.108.197601`.

[55] M. Mrózek, D. Rudnicki, P. Kehayias, A. Jarmola, D. Budker, and W. Gawlik, "Longitudinal spin relaxation in nitrogen-vacancy ensembles in diamond", En, *EPJ Quantum Technology*, vol. 2, no. 1, p. 22, Dec. 2015, ISSN: 2196-0763. DOI: `10.1140/epjqt/s40507-015-0035-z`.

[56] D. A. Redman, S. Brown, R. H. Sands, and S. C. Rand, "Spin dynamics and electronic states of N-V centers in diamond by EPR and four-wave-mixing spectroscopy", *Physical Review Letters*, vol. 67, no. 24, pp. 3420–3423, Dec. 1991. DOI: `10.1103/PhysRevLett.67.3420`.

[57] S. Takahashi, R. Hanson, J. van Tol, M. S. Sherwin, and D. D. Awschalom, "Quenching Spin Decoherence in Diamond through Spin Bath Polarization", *Physical Review Letters*, vol. 101, no. 4, p. 047 601, Jul. 2008. DOI: `10.1103/PhysRevLett.101.047601`.

[58] A. Norambuena Zamorano, "Effect of phonons on the optical properties of color centers in diamond", PhD thesis, 2017.

[59] D. A. Simpson, R. G. Ryan, L. T. Hall, E. Panchenko, S. C. Drew, S. Petrou, P. S. Donnelly, P. Mulvaney, and L. C. L. Hollenberg, "Electron paramagnetic resonance microscopy using spins in diamond under ambient conditions", en, *Nature Communications*, vol. 8, no. 1, p. 458, Dec. 2017, ISSN: 2041-1723. DOI: `10.1038/s41467-017-00466-y`.

[60] S. Steinert, F. Ziem, L. T. Hall, A. Zappe, M. Schweikert, N. Götz, A. Aird, G. Balasubramanian, L. Hollenberg, and J. Wrachtrup, "Magnetic spin imaging under ambient conditions with sub-cellular resolution", en, *Nature Communications*, vol. 4, no. 1, p. 1607, Jun. 2013, ISSN: 2041-1723. DOI: `10.1038/ncomms2588`.

[61] J. D. A. Wood, D. A. Broadway, L. T. Hall, A. Stacey, D. A. Simpson, J.-P. Tetienne, and L. C. L. Hollenberg, "Wide-band nanoscale magnetic resonance spectroscopy using quantum relaxation of a single spin in diamond", en, *Physical Review B*, vol. 94, no. 15, p. 155 402, Oct. 2016, ISSN: 2469-9950, 2469-9969. DOI: `10.1103/PhysRevB.94.155402`.

[62] L. T. Hall, P. Kehayias, D. A. Simpson, A. Jarmola, A. Stacey, D. Budker, and L. C. L. Hollenberg, "Detection of nanoscale electron spin resonance spectra demonstrated using nitrogen-vacancy centre probes in diamond", en, *Nature Communications*, vol. 7, no. 1, p. 10 211, Apr. 2016, ISSN: 2041-1723. DOI: `10.1038/ncomms10211`.

[63] J. F. Barry, J. M. Schloss, E. Bauch, M. J. Turner, C. A. Hart, L. M. Pham, and R. L. Walsworth, "Sensitivity Optimization for NV-Diamond Magnetometry", *arXiv:1903.08176 [cond-mat, physics:physics, physics:quant-ph]*, Mar. 2019.

[64] A. Dréau, M. Lesik, L. Rondin, P. Spinicelli, O. Arcizet, J.-F. Roch, and V. Jacques, "Avoiding power broadening in optically detected magnetic resonance of single NV defects for enhanced dc magnetic field sensitivity", en, *Physical Review B*, vol. 84, no. 19, p. 195 204, Nov. 2011, ISSN: 1098-0121, 1550-235X. DOI: `10.1103/PhysRevB.84.195204`.

[65] Z.-H. Wang, G. de Lange, D. Ristè, R. Hanson, and V. V. Dobrovitski, "Comparison of dynamical decoupling protocols for a nitrogen-vacancy center in diamond", *Physical Review B*, vol. 85, no. 15, p. 155 204, Apr. 2012. DOI: `10.1103/PhysRevB.85.155204`.

[66] S. Schäublin, A. Höhener, and R. Ernst, "Fourier spectroscopy of nonequilibrium states, application to CIDNP, overhauser experiments and relaxation time measurements", *Journal of Magnetic Resonance (1969)*, vol. 13, no. 2,

pp. 196–216, Feb. 1974, ISSN: 0022-2364. DOI: `10.1016/0022-2364(74)90007-9`.

[67] A. Jarmola, A. Berzins, J. Smits, K. Smits, J. Prikulis, F. Gahbauer, R. Ferber, D. Erts, M. Auzinsh, and D. Budker, “Longitudinal spin-relaxation in nitrogen-vacancy centers in electron irradiated diamond”, *Applied Physics Letters*, vol. 107, no. 24, p. 242 403, Dec. 2015, ISSN: 0003-6951. DOI: `10.1063/1.4937489`.

[68] J.-P. Tetienne, R. W. de Gille, D. A. Broadway, T. Teraji, S. E. Lillie, J. M. McCoey, N. Dontschuk, L. T. Hall, A. Stacey, D. A. Simpson, and L. C. L. Hollenberg, “Spin properties of dense near-surface ensembles of nitrogen-vacancy centers in diamond”, *Physical Review B*, vol. 97, no. 8, p. 085 402, Feb. 2018. DOI: `10.1103/PhysRevB.97.085402`.

[69] E. Abe and K. Sasaki, “Tutorial: Magnetic resonance with nitrogen-vacancy centers in diamond—microwave engineering, materials science, and magnetometry”, *Journal of Applied Physics*, vol. 123, no. 16, p. 161 101, Mar. 2018, ISSN: 0021-8979. DOI: `10.1063/1.5011231`.

[70] E. Bauch, C. A. Hart, J. M. Schloss, M. J. Turner, J. F. Barry, P. Kehayias, S. Singh, and R. L. Walsworth, “Ultralong Dephasing Times in Solid-State Spin Ensembles via Quantum Control”, *Physical Review X*, vol. 8, no. 3, p. 031 025, Jul. 2018. DOI: `10.1103/PhysRevX.8.031025`.

[71] C. S. Shin, C. E. Avalos, M. C. Butler, H.-J. Wang, S. J. Seltzer, R.-B. Liu, A. Pines, and V. S. Bajaj, “Suppression of electron spin decoherence of the diamond NV center by a transverse magnetic field”, *Physical Review B*, vol. 88, no. 16, p. 161 412, Oct. 2013. DOI: `10.1103/PhysRevB.88.161412`.

[72] C. Lei, S. Peng, C. Ju, M.-H. Yung, and J. Du, “Decoherence Control of Nitrogen-Vacancy Centers”, en, *Scientific Reports*, vol. 7, no. 1, pp. 1–9, Sep. 2017, ISSN: 2045-2322. DOI: `10.1038/s41598-017-12280-z`.

[73] J. A. v. Wyk, E. C. Reynhardt, G. L. High, and I. Kiflawi, “The dependences of ESR line widths and spin - spin relaxation times of single nitrogen defects on the concentration of nitrogen defects in diamond”, en, *Journal of Physics D: Applied Physics*, vol. 30, no. 12, pp. 1790–1793, Jun. 1997, ISSN: 0022-3727. DOI: `10.1088/0022-3727/30/12/016`.

[74] S. Pezzagna, B. Naydenov, F. Jelezko, J. Wrachtrup, and J. Meijer, “Creation efficiency of nitrogen-vacancy centres in diamond”, en, *New Journal of Physics*, vol. 12, no. 6, p. 065 017, Jun. 2010, ISSN: 1367-2630. DOI: `10.1088/1367-2630/12/6/065017`.

[75] B. Campbell, W. Choudhury, A. Mainwood, M. Newton, and G. Davies, “Lattice damage caused by the irradiation of diamond”, *Nuclear Instruments and Methods in Physics Research Section A: Accelerators, Spectrometers, Detectors and Associated Equipment*, Proc. of the 3rd Int. Conf. on Radiation Effects on Semiconductor Materials, Detectors and Devices, vol. 476, no. 3, pp. 680–685, Jan. 2002, ISSN: 0168-9002. DOI: `10.1016/S0168-9002(01)01664-3`.

[76] M. Capelli, A. H. Heffernan, T. Ohshima, H. Abe, J. Jeske, A. Hope, A. D. Greentree, P. Reineck, and B. C. Gibson, “Increased nitrogen-vacancy centre creation yield in diamond through electron beam irradiation at high temperature”, *Carbon*, vol. 143, pp. 714–719, Mar. 2019, ISSN: 0008-6223. DOI: `10.1016/j.carbon.2018.11.051`.

[77] J. Schwartz, S. Aloni, D. F. Ogletree, and T. Schenkel, “Effects of low-energy electron irradiation on formation of nitrogen–vacancy centers in single-crystal diamond”, en, *New Journal of Physics*, vol. 14, no. 4, p. 043 024, Apr. 2012, ISSN: 1367-2630. DOI: `10.1088/1367-2630/14/4/043024`.

[78] C. Kittel and E. Abrahams, “Dipolar Broadening of Magnetic Resonance Lines in Magnetically Diluted Crystals”, *Physical Review*, vol. 90, no. 2, pp. 238–239, Apr. 1953. DOI: `10.1103/PhysRev.90.238`.

[79] P. L. Stanwix, L. M. Pham, J. R. Maze, D. Le Sage, T. K. Yeung, P. Cappellaro, P. R. Hemmer, A. Yacoby, M. D. Lukin, and R. L. Walsworth, “Coherence of nitrogen-vacancy electronic spin ensembles in diamond”, *Physical Review B*, vol. 82, no. 20, p. 201 201, Nov. 2010. DOI: `10.1103/PhysRevB.82.201201`.

[80] D. Pagliero, K. R. K. Rao, P. R. Zangara, S. Dhomkar, H. H. Wong, A. Abril, N. Aslam, A. Parker, J. King, C. E. Avalos, A. Ajoy, J. Wrachtrup, A. Pines, and C. A. Meriles, “Multispin-assisted optical pumping of bulk 13c nuclear spin polarization in diamond”, *Physical Review B*, vol. 97, no. 2, p. 024 422, Jan. 2018. DOI: `10.1103/PhysRevB.97.024422`.

[81] R. Wunderlich, J. Kohlrautz, B. Abel, J. Haase, and J. Meijer, “Optically induced cross relaxation via nitrogen-related defects for bulk diamond 13c hyperpolarization”, *Physical Review B*, vol. 96, no. 22, p. 220 407, Dec. 2017. DOI: `10.1103/PhysRevB.96.220407`.

[82] J. D. A. Wood, “Quantum Relaxometric Spectroscopy Using The Nitrogen-Vacancy Centre in Diamond”, en, PhD thesis, University of Melbourne, 2018.

[83] T. Rendler, J. Neburkova, O. Zemek, J. Kotek, A. Zappe, Z. Chu, P. Cigler, and J. Wrachtrup, "Optical imaging of localized chemical events using programmable diamond quantum nanosensors", eng, *Nature communications*, vol. 8, pp. 14 701–14 701, Mar. 2017, ISSN: 2041-1723. DOI: `10.1038/ncomms14701`.

[84] H. Demers, N. Poirier-Demers, A. R. Couture, D. Joly, M. Guilmain, N. de Jonge, and D. Drouin, "Three-dimensional electron microscopy simulation with the CASINO Monte Carlo software", *Scanning*, vol. 33, no. 3, pp. 135–146, May 2011, ISSN: 0161-0457. DOI: `10.1002/sca.20262`.

[85] *ESTAR Database.*

[86] J. Koike, D. M. Parkin, and T. E. Mitchell, "Displacement threshold energy for type IIa diamond", *Applied Physics Letters*, vol. 60, no. 12, pp. 1450–1452, Mar. 1992, ISSN: 0003-6951. DOI: `10.1063/1.107267`.

[87] P. Deák, B. Aradi, M. Kaviani, T. Frauenheim, and A. Gali, "Formation of NV centers in diamond: A theoretical study based on calculated transitions and migration of nitrogen and vacancy related defects", *Phys. Rev. B*, vol. 89, no. 7, p. 075 203, Feb. 2014. DOI: `10.1103/PhysRevB.89.075203`.

[88] E. Kim, V. M. Acosta, E. Bauch, D. Budker, and P. R. Hemmer, "Electron spin resonance shift and linewidth broadening of nitrogen-vacancy centers in diamond as a function of electron irradiation dose", *Applied Physics Letters*, vol. 101, no. 8, Aug. 2012, ISSN: 0003-6951. DOI: `10.1063/1.4747211`.

[89] D. C. Johnston, "Stretched exponential relaxation arising from a continuous sum of exponential decays", *Physical Review B*, vol. 74, no. 18, p. 184 430, Nov. 2006. DOI: `10.1103/PhysRevB.74.184430`.

[90] J.-C. Jaskula, E. Bauch, S. Arroyo-Camejo, M. D. Lukin, S. W. Hell, A. S. Trifonov, and R. L. Walsworth, "Superresolution optical magnetic imaging and spectroscopy using individual electronic spins in diamond", EN, *Optics Express*, vol. 25, no. 10, pp. 11 048–11 064, May 2017, ISSN: 1094-4087. DOI: `10.1364/OE.25.011048`.

[91] D. R. Glenn, R. R. Fu, P. Kehayias, D. L. Sage, E. A. Lima, B. P. Weiss, and R. L. Walsworth, "Micrometer-scale magnetic imaging of geological samples using a quantum diamond microscope", en, *Geochemistry, Geophysics, Geosystems*, vol. 18, no. 8, pp. 3254–3267, 2017, ISSN: 1525-2027. DOI: `10.1002/2017GC006946`.

[92] V. V. Dremov, S. Y. Grebenchuk, A. G. Shishkin, D. S. Baranov, R. A. Hovhannisyan, O. V. Skryabina, N. Lebedev, I. A. Golovchanskiy, V. I. Chichkov, C. Brun, T. Cren, V. M. Krasnov, A. A. Golubov, D. Roditchev, and V. S. Stolyarov, "Local Josephson vortex generation and manipulation with a Magnetic Force Microscope", en, *Nature Communications*, vol. 10, no. 1, pp. 1–9, Sep. 2019, ISSN: 2041-1723. DOI: `10.1038/s41467-019-11924-0`.

[93] T. Jungwirth, X. Marti, P. Wadley, and J. Wunderlich, "Antiferromagnetic spintronics", en, *Nature Nanotechnology*, vol. 11, no. 3, pp. 231–241, Mar. 2016, ISSN: 1748-3395. DOI: `10.1038/nnano.2016.18`.

[94] E. V. Levine, M. J. Turner, P. Kehayias, C. A. Hart, N. Langellier, R. Trubko, D. R. Glenn, R. R. Fu, and R. L. Walsworth, "Principles and techniques of the quantum diamond microscope", *Nanophotonics*, vol. 8, no. 11, pp. 1945–1973, 2019, ISSN: 2192-8614. DOI: `10.1515/nanoph-2019-0209`.

[95] D. B. Murphy, *Fundamentals of light microscopy and electronic imaging.* John Wiley & Sons, 2002, ISBN: 0-471-23429-X.

[96] A. Haque and S. Sumaiya, "An Overview on the Formation and Processing of Nitrogen-Vacancy Photonic Centers in Diamond by Ion Implantation", *Journal of Manufacturing and Materials Processing*, vol. 1, no. 1, 2017, ISSN: 2504-4494. DOI: `10.3390/jmmp1010006`.

[97] H. Pinto, R. Jones, D. W. Palmer, J. P. Goss, P. R. Briddon, and S. Öberg, "On the diffusion of NV defects in diamond", *physica status solidi (a)*, vol. 209, no. 9, pp. 1765–1768, Sep. 2012, ISSN: 1862-6300. DOI: `10.1002/pssa.201200050`.

[98] L. Dei Cas, S. Zeldin, N. Nunn, M. Torelli, A. I. Shames, A. M. Zaitsev, and O. Shenderova, "From Fancy Blue to Red: Controlled Production of a Vibrant Color Spectrum of Fluorescent Diamond Particles", *Advanced Functional Materials*, vol. 29, no. 19, p. 1 808 362, May 2019, ISSN: 1616-301X. DOI: `10.1002/adfm.201808362`.

[99] I. Fescenko, A. Jarmola, I. Savukov, P. Kehayias, J. Smits, J. Damron, N. Ristoff, N. Mosavian, and V. M. Acosta, "Diamond magnetometer enhanced by ferrite flux concentrators", en, *arXiv:1911.05070 [cond-mat, physics:physics]*, Nov. 2019.

[100] S. Steinert, F. Dolde, P. Neumann, A. Aird, B. Naydenov, G. Balasubramanian, F. Jelezko, and J. Wrachtrup, "High sensitivity magnetic imaging using an array of spins in diamond", eng, *The Review of Scientific*

Instruments, vol. 81, no. 4, p. 043 705, Apr. 2010, ISSN: 1089-7623. DOI: `10.1063/1.3385689`.

[101] L. M. Pham, D. Le Sage, P. L. Stanwix, T. K. Yeung, D. Glenn, A. Trifonov, P. Cappellaro, P. R. Hemmer, M. D. Lukin, H. Park, A. Yacoby, and R. L. Walsworth, "Magnetic field imaging with nitrogen-vacancy ensembles", *New Journal of Physics*, vol. 13, no. 4, p. 045 021, Apr. 2011, ISSN: 1367-2630. DOI: `10.1088/1367-2630/13/4/045021`.

[102] Y. Schlussel, T. Lenz, D. Rohner, Y. Bar-Haim, L. Bougas, D. Groswasser, M. Kieschnick, E. Rozenberg, L. Thiel, A. Waxman, J. Meijer, P. Maletinsky, D. Budker, and R. Folman, "Wide-Field Imaging of Superconductor Vortices with Electron Spins in Diamond", *Physical Review Applied*, vol. 10, no. 3, p. 034 032, Sep. 2018. DOI: `10.1103/PhysRevApplied.10.034032`.

[103] P. Kehayias, M. J. Turner, R. Trubko, J. M. Schloss, C. A. Hart, M. Wesson, D. R. Glenn, and R. L. Walsworth, "Imaging crystal stress in diamond using ensembles of nitrogen-vacancy centers", *Physical Review B*, vol. 100, no. 17, p. 174 103, Nov. 2019. DOI: `10.1103/PhysRevB.100.174103`.

[104] I. Fescenko, A. Laraoui, J. Smits, N. Mosavian, P. Kehayias, J. Seto, L. Bougas, A. Jarmola, and V. M. Acosta, "Diamond Magnetic Microscopy of Malarial Hemozoin Nanocrystals", *Physical Review Applied*, vol. 11, no. 3, p. 034 029, Mar. 2019. DOI: `10.1103/PhysRevApplied.11.034029`.

[105] L. M. Coronado, C. T. Nadovich, and C. Spadafora, "Malarial hemozoin: From target to tool", *Biochimica et Biophysica Acta (BBA) - General Subjects*, vol. 1840, no. 6, pp. 2032–2041, Jun. 2014, ISSN: 0304-4165. DOI: `10.1016/j.bbagen.2014.02.009`.

[106] A. Butykai, A. Orbán, V. Kocsis, D. Szaller, S. Bordács, E. Tátrai-Szekeres, L. F. Kiss, A. Bóta, B. G. Vértessy, T. Zelles, and I. Kézsmárki, "Malaria pigment crystals as magnetic micro-rotors: Key for high-sensitivity diagnosis", en, *Scientific Reports*, vol. 3, p. 1431, Mar. 2013, ISSN: 2045-2322. DOI: `10.1038/srep01431`.

[107] M. Inyushin, Y. Kucheryavih, L. Kucheryavih, L. Rojas, I. Khmelinskii, and V. Makarov, "Superparamagnetic Properties of Hemozoin", *Scientific Reports*, vol. 6, no. 1, p. 26 212, May 2016, ISSN: 2045-2322. DOI: `10.1038/srep26212`.

[108] I. Khmelinskii and V. Makarov, "Temperature dependence of the spin relaxation time of Fe3o4 and hemozoin superparamagnetic nanocrystals", *Chemical Physics*, vol. 493, pp. 120–132, Aug. 2017, ISSN: 0301-0104. DOI: `10.1016/j.chemphys.2017.06.015`.

[109] M. Lesik, J.-P. Tetienne, A. Tallaire, J. Achard, V. Mille, A. Gicquel, J.-F. Roch, and V. Jacques, “Perfect preferential orientation of nitrogen-vacancy defects in a synthetic diamond sample”, *Applied Physics Letters*, vol. 104, no. 11, p. 113 107, Mar. 2014, ISSN: 0003-6951. DOI: `10.1063/1.4869103`.

[110] C. Osterkamp, M. Mangold, J. Lang, P. Balasubramanian, T. Teraji, B. Naydenov, and F. Jelezko, “Engineering preferentially-aligned nitrogen-vacancy centre ensembles in CVD grown diamond”, *Scientific Reports*, vol. 9, no. 1, p. 5786, Apr. 2019, ISSN: 2045-2322. DOI: `10.1038/s41598-019-42314-7`.

[111] J. Yaita, T. Tsuji, M. Hatano, and T. Iwasaki, “Preferentially aligned nitrogen-vacancy centers in heteroepitaxial (111) diamonds on Si substrates via 3c-SiC intermediate layers”, *Applied Physics Express*, vol. 11, no. 4, p. 045 501, Mar. 2018, ISSN: 1882-0778. DOI: `10.7567/apex.11.045501`.

[112] A. Ajoy, K. Liu, R. Nazaryan, X. Lv, P. R. Zangara, B. Safvati, G. Wang, D. Arnold, G. Li, A. Lin, P. Raghavan, E. Druga, S. Dhomkar, D. Pagliero, J. A. Reimer, D. Suter, C. A. Meriles, and A. Pines, “Orientation-independent room temperature optical (13)C hyperpolarization in powdered diamond”, eng, *Science advances*, vol. 4, no. 5, eaar5492–eaar5492, May 2018, ISSN: 2375-2548. DOI: `10.1126/sciadv.aar5492`.

[113] P. R. Zangara, S. Dhomkar, A. Ajoy, K. Liu, R. Nazaryan, D. Pagliero, D. Suter, J. A. Reimer, A. Pines, and C. A. Meriles, “Dynamics of frequency-swept nuclear spin optical pumping in powdered diamond at low magnetic fields”, *Proceedings of the National Academy of Sciences*, vol. 116, no. 7, p. 2512, Feb. 2019. DOI: `10.1073/pnas.1811994116`.

[114] N. Aslam, M. Pfender, P. Neumann, R. Reuter, A. Zappe, F. F. d. Oliveira, A. Denisenko, H. Sumiya, S. Onoda, J. Isoya, and J. Wrachtrup, “Nanoscale nuclear magnetic resonance with chemical resolution”, en, *Science*, vol. 357, no. 6346, pp. 67–71, Jul. 2017, ISSN: 0036-8075, 1095-9203. DOI: `10.1126/science.aam8697`.

[115] J.-H. Ardenkjaer-Larsen, G. S. Boebinger, A. Comment, S. Duckett, A. S. Edison, F. Engelke, C. Griesinger, R. G. Griffin, C. Hilty, H. Maeda, G. Parigi, T. Prisner, E. Ravera, J. van Bentum, S. Vega, A. Webb, C. Luchinat, H. Schwalbe, and L. Frydman, “Facing and Overcoming Sensitivity Challenges in Biomolecular NMR Spectroscopy”, en, *Angewandte Chemie International Edition*, vol. 54, no. 32, pp. 9162–9185, 2015, ISSN: 1521-3773. DOI: `10.1002/anie.201410653`.

[116] E. M. Purcell, H. C. Torrey, and R. V. Pound, “Resonance absorption by nuclear magnetic moments in a solid”, *Physical review*, vol. 69, no. 1-2, p. 37, 1946.

[117] F. Bloch, W. W. Hansen, and M. E. Packard, “Physical review”, *Phys Rev*, vol. 70, pp. 460–473, 1946.

[118] M. H. Levitt, *Spin dynamics: basics of nuclear magnetic resonance.* John Wiley & Sons, 2001, ISBN: 0-471-48921-2.

[119] J. Seliger, “Nuclear Quadrupole Resonance, Theory”, en, in *Encyclopedia of Spectroscopy and Spectrometry*, J. C. Lindon, Ed., Oxford: Elsevier, Jan. 1999, pp. 1672–1680, ISBN: 978-0-12-226680-5. DOI: `10.1006/rwsp.2000.0211`.

[120] I. Fugariu, R. Soong, D. Lane, M. Fey, W. Maas, F. Vincent, A. Beck, D. Schmidig, B. Treanor, and A. J. Simpson, “Towards single egg toxicity screening using microcoil NMR”, en, *The Analyst*, vol. 142, no. 24, pp. 4812–4824, 2017, ISSN: 0003-2654, 1364-5528. DOI: `10.1039/C7AN01339F`.

[121] M. Grisi, F. Vincent, B. Volpe, R. Guidetti, N. Harris, A. Beck, and G. Boero, “NMR spectroscopy of single sub-nL ova with inductive ultra-compact single-chip probes”, en, *Scientific Reports*, vol. 7, p. 44 670, Mar. 2017, ISSN: 2045-2322. DOI: `10.1038/srep44670`.

[122] E. Montinaro, M. Grisi, M. C. Letizia, L. Pethö, M. a. M. Gijs, R. Guidetti, J. Michler, J. Brugger, and G. Boero, “3d printed microchannels for sub-nL NMR spectroscopy”, en, *PLOS ONE*, vol. 13, no. 5, e0192780, May 2018, ISSN: 1932-6203. DOI: `10.1371/journal.pone.0192780`.

[123] D. A. Seeber, R. L. Cooper, L. Ciobanu, and C. H. Pennington, “Design and testing of high sensitivity microreceiver coil apparatus for nuclear magnetic resonance and imaging”, *Review of Scientific Instruments*, vol. 72, no. 4, pp. 2171–2179, Mar. 2001, ISSN: 0034-6748. DOI: `10.1063/1.1359190`.

[124] J. E. Stocker, T. L. Peck, A. G. Webb, M. Feng, and R. L. Magin, “Nanoliter volume, high-resolution NMR microspectroscopy using a 60-/spl mu/m planar microcoil”, *IEEE Transactions on Biomedical Engineering*, vol. 44, no. 11, pp. 1122–1127, Nov. 1997, ISSN: 0018-9294. DOI: `10.1109/10.641340`.

[125] A. G. Webb and S. C. Grant, “Signal-to-noise and magnetic susceptibility trade-offs in solenoidal microcoils for NMR.”, eng, *Journal of magnetic resonance. Series B*, vol. 113, no. 1, pp. 83–87, Oct. 1996, ISSN: 1064-1866. DOI: `10.1006/jmrb.1996.0159`.

[126] M. Grisi, “Broadband single-chip transceivers for compact NMR probes”, en, PhD thesis, 2017. DOI: `10.5075/epfl-thesis-7755`.

[127] “Magnetic Field Inhomogeneity Effects and T2* Dephasing”, en, in *Magnetic Resonance Imaging*, John Wiley & Sons, Ltd, 2014, pp. 569–617, ISBN: 978-1-118-63395-3. DOI: `10.1002/9781118633953.ch20`.

[128] M. E. Stoll and T. J. Majors, “Reduction of magnetic susceptibility broadening in NMR by susceptibility matching”, *Journal of Magnetic Resonance (1969)*, vol. 46, no. 2, pp. 283–288, Feb. 1982, ISSN: 0022-2364. DOI: `10.1016/0022-2364(82)90143-3`.

[129] J. Smits, J. T. Damron, P. Kehayias, A. F. McDowell, N. Mosavian, I. Fescenko, N. Ristoff, A. Laraoui, A. Jarmola, and V. M. Acosta, “Two-dimensional nuclear magnetic resonance spectroscopy with a microfluidic diamond quantum sensor”, *Science Advances*, vol. 5, no. 7, eaaw7895, Jul. 2019. DOI: `10.1126/sciadv.aaw7895`.

[130] H. G. Krojanski, J. Lambert, Y. Gerikalan, D. Suter, and R. Hergenröder, “Microslot NMR Probe for Metabolomics Studies”, *Analytical Chemistry*, vol. 80, no. 22, pp. 8668–8672, Nov. 2008, ISSN: 0003-2700. DOI: `10.1021/ac801636a`.

[131] D. L. Olson, T. L. Peck, A. G. Webb, R. L. Magin, and J. V. Sweedler, “High-Resolution Microcoil 1h-NMR for Mass-Limited, Nanoliter-Volume Samples”, en, *Science*, vol. 270, no. 5244, pp. 1967–1970, Dec. 1995, ISSN: 0036-8075, 1095-9203. DOI: `10.1126/science.270.5244.1967`.

[132] D. B. Bucher, D. R. Glenn, H. Park, M. D. Lukin, and R. L. Walsworth, “Hyperpolarization-enhanced NMR spectroscopy with femtomole sensitivity using quantum defects in diamond”, *arXiv:1810.02408 [physics, physics:quant-ph]*, Oct. 2018.

[133] P. A. Guitard, R. Ayde, G. Jasmin-Lebras, L. Caruso, M. Pannetier-Lecoeur, and C. Fermon, “Local nuclear magnetic resonance spectroscopy with giant magnetic resistance-based sensors”, *Applied Physics Letters*, vol. 108, no. 21, p. 212 405, May 2016, ISSN: 0003-6951. DOI: `10.1063/1.4952947`.

[134] D. A. Jayawickrama and J. V. Sweedler, “Hyphenation of capillary separations with nuclear magnetic resonance spectroscopy”, *Journal of Chromatography A*, A Century of Chromatography 1903-2003, vol. 1000, no. 1, pp. 819–840, Jun. 2003, ISSN: 0021-9673. DOI: `10.1016/S0021-9673(03)00447-3`.

[135] N. C. Gonnella, *LC-NMR : Expanding the Limits of Structure Elucidation*, en. CRC Press, Mar. 2013, ISBN: 978-0-429-06595-8. DOI: `10.1201/b13857`.

[136] *Analytical Techniques Combining Mass Spectrometry and Chromatography*, en.

[137] B. Liu, K. T. Kongstad, S. Wiese, A. K. Jäger, and D. Staerk, "Edible seaweed as future functional food: Identification of alpha-glucosidase inhibitors by combined use of high-resolution alpha-glucosidase inhibition profiling and HPLC–HRMS–SPE–NMR", *Food Chemistry*, vol. 203, pp. 16–22, Jul. 2016, ISSN: 0308-8146. DOI: `10.1016/j.foodchem.2016.02.001`.

[138] S. G. Wubshet, Y. Tahtah, A. M. Heskes, K. T. Kongstad, I. Pateraki, B. Hamberger, B. L. Møller, and D. Staerk, "Identification of PTP1b and alpha-Glucosidase Inhibitory Serrulatanes from Eremophila spp. by Combined use of Dual High-Resolution PTP1b and alpha-Glucosidase Inhibition Profiling and HPLC-HRMS-SPE-NMR", *Journal of Natural Products*, vol. 79, no. 4, pp. 1063–1072, Apr. 2016, ISSN: 0163-3864. DOI: `10.1021/acs.jnatprod.5b01128`.

[139] O. Kenny, N. P. Brunton, D. Walsh, C. M. Hewage, P. McLoughlin, and T. J. Smyth, "Characterisation of Antimicrobial Extracts from Dandelion Root (Taraxacum officinale) Using LC-SPE-NMR", en, *Phytotherapy Research*, vol. 29, no. 4, pp. 526–532, 2015, ISSN: 1099-1573. DOI: `10.1002/ptr.5276`.

[140] S. G. Wubshet, I. M. C. Brighente, R. Moaddel, and D. Staerk, "Magnetic Ligand Fishing as a Targeting Tool for HPLC-HRMS-SPE-NMR: Alpha-Glucosidase Inhibitory Ligands and Alkylresorcinol Glycosides from Eugenia catharinae", *Journal of Natural Products*, vol. 78, no. 11, pp. 2657–2665, Nov. 2015, ISSN: 0163-3864. DOI: `10.1021/acs.jnatprod.5b00603`.

[141] L. M. Pham, S. J. DeVience, F. Casola, I. Lovchinsky, A. O. Sushkov, E. Bersin, J. Lee, E. Urbach, P. Cappellaro, H. Park, A. Yacoby, M. Lukin, and R. L. Walsworth, "NMR technique for determining the depth of shallow nitrogen-vacancy centers in diamond", *Physical Review B*, vol. 93, no. 4, p. 045 425, Jan. 2016. DOI: `10.1103/PhysRevB.93.045425`.

[142] S. J. DeVience, L. M. Pham, I. Lovchinsky, A. O. Sushkov, N. Bar-Gill, C. Belthangady, F. Casola, M. Corbett, H. Zhang, M. Lukin, H. Park, A. Yacoby, and R. L. Walsworth, "Nanoscale NMR spectroscopy and imaging of multiple nuclear species", en, *Nature Nanotechnology*, vol. 10, no. 2, pp. 129–134, Feb. 2015, ISSN: 1748-3395. DOI: `10.1038/nnano.2014.313`.

[143] Ł. Cywiński, R. M. Lutchyn, C. P. Nave, and S. Das Sarma, "How to enhance dephasing time in superconducting qubits", *Physical Review B*, vol. 77, no. 17, p. 174 509, May 2008. DOI: `10.1103/PhysRevB.77.174509`.

[144] D. Farfurnik, A. Jarmola, L. M. Pham, Z. H. Wang, V. V. Dobrovitski, R. L. Walsworth, D. Budker, and N. Bar-Gill, "Optimizing a dynamical decoupling protocol for solid-state electronic spin ensembles in diamond", *Physical Review B*, vol. 92, no. 6, p. 060 301, Aug. 2015. DOI: `10.1103/PhysRevB.92.060301`.

[145] A. Laraoui, F. Dolde, C. Burk, F. Reinhard, J. Wrachtrup, and C. A. Meriles, "High-resolution correlation spectroscopy of 13c spins near a nitrogen-vacancy centre in diamond", *Nature Communications*, vol. 4, no. 1, p. 1651, Apr. 2013, ISSN: 2041-1723. DOI: `10.1038/ncomms2685`.

[146] S. Zaiser, T. Rendler, I. Jakobi, T. Wolf, S.-Y. Lee, S. Wagner, V. Bergholm, T. Schulte-Herbrüggen, P. Neumann, and J. Wrachtrup, "Enhancing quantum sensing sensitivity by a quantum memory", en, *Nature Communications*, vol. 7, no. 1, pp. 1–11, Aug. 2016, ISSN: 2041-1723. DOI: `10.1038/ncomms12279`.

[147] I. Lovchinsky, A. O. Sushkov, E. Urbach, N. P. de Leon, S. Choi, K. De Greve, R. Evans, R. Gertner, E. Bersin, C. Müller, L. McGuinness, F. Jelezko, R. L. Walsworth, H. Park, and M. D. Lukin, "Nuclear magnetic resonance detection and spectroscopy of single proteins using quantum logic", *Science*, vol. 351, no. 6275, p. 836, Feb. 2016. DOI: `10.1126/science.aad8022`.

[148] J. M. Boss, K. S. Cujia, J. Zopes, and C. L. Degen, "Quantum sensing with arbitrary frequency resolution", en, *Science*, vol. 356, no. 6340, pp. 837–840, May 2017, ISSN: 0036-8075, 1095-9203. DOI: `10.1126/science.aam7009`.

[149] H. Harcken, R. Ketzler, M. Albrecht, M. Burghoff, S. Hartwig, and L. Trahms, "The natural line width of low field nuclear magnetic resonance spectra", en, *Journal of Magnetic Resonance*, vol. 206, no. 1, pp. 168–170, Sep. 2010, ISSN: 1090-7807. DOI: `10.1016/j.jmr.2010.06.008`.

[150] S.-H. Liao, M.-J. Chen, H.-C. Yang, S.-Y. Lee, H.-H. Chen, H.-E. Horng, and S.-Y. Yang, "A study of J-coupling spectroscopy using the Earth's field nuclear magnetic resonance inside a laboratory", eng, *The Review of Scientific Instruments*, vol. 81, no. 10, p. 104 104, Oct. 2010, ISSN: 1089-7623. DOI: `10.1063/1.3498895`.

[151] J. N. Robinson, A. Coy, R. Dykstra, C. D. Eccles, M. W. Hunter, and P. T. Callaghan, "Two-dimensional NMR spectroscopy in Earth's magnetic field", en, *Journal of Magnetic Resonance*, vol. 182, no. 2, pp. 343–347, Oct. 2006, ISSN: 1090-7807. DOI: `10.1016/j.jmr.2006.06.027`.

[152] W. G. Paterson and E. J. Wells, “NMR spectrum of para-difluorobenzene”, en, *Journal of Molecular Spectroscopy*, vol. 14, no. 1, pp. 101–111, Jan. 1964, ISSN: 0022-2852. DOI: `10.1016/0022-2852(64)90105-5`.

[153] H. J. Hogben, M. Krzystyniak, G. T. P. Charnock, P. J. Hore, and I. Kuprov, “Spinach–a software library for simulation of spin dynamics in large spin systems”, eng, *Journal of Magnetic Resonance (San Diego, Calif.: 1997)*, vol. 208, no. 2, pp. 179–194, Feb. 2011, ISSN: 1096-0856. DOI: `10.1016/j.jmr.2010.11.008`.

[154] J. P. King, K. Jeong, C. C. Vassiliou, C. S. Shin, R. H. Page, C. E. Avalos, H.-J. Wang, and A. Pines, “Room-temperature in situ nuclear spin hyperpolarization from optically pumped nitrogen vacancy centres in diamond”, eng, *Nature Communications*, vol. 6, p. 8965, Dec. 2015, ISSN: 2041-1723. DOI: `10.1038/ncomms9965`.

[155] P. London, J. Scheuer, J.-M. Cai, I. Schwarz, A. Retzker, M. B. Plenio, M. Katagiri, T. Teraji, S. Koizumi, J. Isoya, R. Fischer, L. P. McGuinness, B. Naydenov, and F. Jelezko, “Detecting and Polarizing Nuclear Spins with Double Resonance on a Single Electron Spin”, *Physical Review Letters*, vol. 111, no. 6, p. 067 601, Aug. 2013. DOI: `10.1103/PhysRevLett.111.067601`.

[156] A. R. Lang, “Causes of Birefringence in Diamond”, en, *Nature*, vol. 213, no. 5073, pp. 248–251, Jan. 1967, ISSN: 1476-4687. DOI: `10.1038/213248a0`.